2017

Engineering Plasmonic Nanocrystal Coupling Through Template-Assisted Self-Assembly

Nicholas J. Greybush
University of Pennsylvania, greybush@seas.upenn.edu

Engineering Plasmonic Nanocrystal Coupling Through Template-Assisted Self-Assembly

Abstract
The construction of materials from nanocrystal building blocks represents a powerful new paradigm for materials design. Just as nature's materials orchestrate intricate combinations of atoms from the library of the periodic table, nanocrystal "metamaterials" integrate individual nanocrystals into larger architectures with emergent collective properties. The individual nanocrystal "meta-atoms" that make up these materials are themselves each a nanoscale atomic system with tailorable size, shape, and elemental composition, enabling the creation of hierarchical materials with predesigned structure at multiple length scales. However, an improved fundamental understanding of the interactions among individual nanocrystals is needed in order to translate this structural control into enhanced functionality. The ability to form precise arrangements of nanocrystals and measure their collective properties is therefore essential for the continued development of nanocrystal metamaterials. In this dissertation, we utilize template-assisted self-assembly and spatially-resolved spectroscopy to form and characterize individual nanocrystal oligomers. At the intersection of "top-down" and "bottom-up" nanoscale patterning schemes, template-assisted self-assembly combines the design freedom of lithography with the chemical control of colloidal synthesis to achieve unique nanocrystal configurations. Here, we employ shape-selective templates to assemble new plasmonic structures, including heterodimers of Au nanorods and upconversion phosphors, a series of hexagonally-packed Au nanocrystal oligomers, and triangular formations of Au nanorods. Through experimental analysis and numerical simulation, we elucidate the means through which inter-nanocrystal coupling imparts collective optical properties to the plasmonic assemblies. Our self-assembly and measurement strategy offers a versatile platform for exploring optical interactions in a wide range of material systems and application areas.

Degree Type
Dissertation

Degree Name
Doctor of Philosophy (PhD)

Graduate Group
Materials Science & Engineering

First Advisor
Cherie R. Kagan

Second Advisor
Christopher B. Murray

Keywords
metamaterials, nanocrystals, optical materials, plasmonics, self-assembly, spectroscopy

ENGINEERING PLASMONIC NANOCRYSTAL COUPLING THROUGH TEMPLATE-ASSISTED SELF-ASSEMBLY

Nicholas J. Greybush

A DISSERTATION

in

Materials Science and Engineering

Presented to the Faculties of the University of Pennsylvania

in

Partial Fulfillment of the Requirements for the

Degree of Doctor of Philosophy

2017

Supervisor of Dissertation

_____

Cherie R. Kagan

Stephen J. Angello Professor

Materials Science and Engineering

Co-Supervisor of Dissertation

_____

Christopher B. Murray

Richard Perry University Professor

Materials Science and Engineering

Graduate Group Chairperson

_____

David J. Srolovitz, Joseph Bordogna Professor, Materials Science and Engineering

Dissertation Committee

Nader Engheta, H. Nedwill Ramsey Professor, Electrical and Systems Engineering

Lee C. Bassett, Assistant Professor, Electrical and Systems Engineering

ENGINEERING PLASMONIC NANOCRYSTAL COUPLING

THROUGH TEMPLATE-ASSISTED SELF-ASSEMBLY

To my family…

ACKNOWLEDGMENTS

Throughout my graduate career I have had the great fortune of having two incredible mentors, Prof. Cherie Kagan and Prof. Chris Murray, whose boundless creativity and tireless enthusiasm for science are an inspiration to all who know them. Their prodigious scientific vision continues to lead to many exciting research directions, and I am grateful for having shared in it. Thank you for welcoming me so generously into the group, for supporting my research, for providing me opportunities to present my work externally, and for offering the valuable guidance and direction that have shaped my scientific and personal development.

I would like to express my gratitude to the following:

To Prof. Nader Engheta, who as a teacher, collaborator, and committee member has helped open my eyes to the wonders and possibilities of light.

To Prof. Lee Bassett, for graciously agreeing to lend his expertise as a committee member on such short notice.

To all of the postdoctoral, Ph.D., masters, and undergraduate members of the Kagan and Murray groups past and present, who have been exceptional colleagues and friends. To the senior members, thank you for welcoming me into the group, leading by example, and patiently and generously imparting your hard-earned wisdom and experience. Thank you to all for making the lab a vibrant environment and for the many

fruitful discussions and collaborations. My best wishes for continued success to all of the current members.

To my internal and external collaborators, for making my research possible and inviting me to share in yours. A special thanks to Prof. Jay Kikkawa, for offering his time and measurement capabilities to make the darkfield scattering measurements a reality. Thank you to co-authors Victor Pacheco Peña, Iñigo Liberal, and Christian Della Giovampaola of the Engheta Group; Ludivine Malassis, Xingchen Ye, and Ben Diroll of the Murray Group; Marjan Saboktakin, SJ Oh, Wenxiang Chen, Ed Goodwin, and Nathaniel Berry of the Kagan Group; Rana Ashkar of Oak Ridge National Laboratory; and Mike Hore of Case Western Reserve University.

To the talented and hardworking university staff for their tireless efforts to make Penn run smoothly. To Irene, Pat, Vicky, Steve, and Kristin in the LRSM; to Jamie and Doug of the NCF; to all of the QNF staff; to Lillian and the MBO staff; to John in Singh; and to all in the ESE office, thank you for offering your help whenever I needed it.

To the NSF MRSEC DMR-1120901 for financially supporting my research activities, and to all the members of the MRSEC IRG for our illuminating conversations. I am also grateful for the support of the John Henry Towne Fellowship and Ashton Scholarship for my academic endeavors.

To all of the MSE students past and present, whose names are too innumerable to enumerate, but whose friendship and camaraderie have made my time at Penn fun, enjoyable, and ever-surprising. A special thanks to the senior members for serving as

friendly role-models, and for offering perspective, guidance, and reassurance at just the right moments.

To my MSE cohort: Frank, Dan, Rob, Daksh, and Jacob, and to Spencer. I will always treasure our Philadelphia memories: the joyous, the stressful, the profound, and the absurd. I could not have hoped for better friends to share them with.

To my former teachers and mentors, for the many ways they have inspired me and broadened my understanding.

Finally, to my friends and family, most especially to my parents James and Leona Greybush and my brother Steven, who know that their everlasting support extends far beyond what can be acknowledged on this page. Thank you.

ABSTRACT

ENGINEERING PLASMONIC NANOCRYSTAL COUPLING

THROUGH TEMPLATE-ASSISTED SELF-ASSEMBLY

Nicholas J. Greybush

Cherie R. Kagan

Christopher B. Murray

The construction of materials from nanocrystal building blocks represents a powerful new paradigm for materials design. Just as nature's materials orchestrate intricate combinations of atoms from the library of the periodic table, nanocrystal "metamaterials" integrate individual nanocrystals into larger architectures with emergent collective properties. The individual nanocrystal "meta-atoms" that make up these materials are themselves each a nanoscale atomic system with tailorable size, shape, and elemental composition, enabling the creation of hierarchical materials with predesigned structure at multiple length scales. However, an improved fundamental understanding of the interactions among individual nanocrystals is needed in order to translate this structural control into enhanced functionality. The ability to form precise arrangements of nanocrystals and measure their collective properties is therefore essential for the continued development of nanocrystal metamaterials. In this dissertation, we utilize template-assisted self-assembly and spatially-resolved spectroscopy to form and characterize individual nanocrystal oligomers. At the intersection of "top-down" and "bottom-up" nanoscale patterning schemes, template-assisted self-assembly combines the design freedom of lithography with the chemical control of colloidal synthesis to achieve unique nanocrystal configurations. Here, we employ shape-selective templates to assemble new plasmonic structures, including heterodimers of Au nanorods and upconversion phosphors, a series of hexagonally-packed Au nanocrystal

oligomers, and triangular formations of Au nanorods. Through experimental analysis and numerical simulation, we elucidate the means through which inter-nanocrystal coupling imparts collective optical properties to the plasmonic assemblies. Our self-assembly and measurement strategy offers a versatile platform for exploring optical interactions in a wide range of material systems and application areas.

TABLE OF CONTENTS

ACKNOWLEDGMENTS ..... **IV**

ABSTRACT ..... **VII**

TABLE OF CONTENTS ..... **IX**

LIST OF TABLES ..... **XIII**

LIST OF FIGURES ..... **XIV**

CHAPTER 1. INTRODUCTION **1**

1.1 Nanocrystal Assemblies: a New Paradigm for Materials Design **1**

1.2 Template-Assisted Self-Assembly **3**

1.3 Plasmonic Nanocrystals **5**

1.4 Outline of Dissertation Chapters **8**

CHAPTER 2. PLASMON-ENHANCED UPCONVERSION LUMINESCENCE IN SINGLE NANOPHOSPHOR–NANOROD HETERODIMERS FORMED THROUGH TEMPLATE-ASSISTED SELF-ASSEMBLY **10**

2.1 Introduction **10**

2.2 Results and Discussion 13

2.3 Conclusions 35

2.4 Methods 36

2.4.1 Nanocrystal Synthesis 36

2.4.2 Template Fabrication and Nanocrystal Assembly 36

2.4.3 Structural and Optical Measurements 37

2.4.4 Simulations 38

2.5 Supplemental Discussion 39

CHAPTER 3. PLASMON RESONANCES IN SELF-ASSEMBLED TWO-DIMENSIONAL AU NANOCRYSTAL METAMOLECULES 41

3.1 Introduction 41

3.2 Results and Discussion 44

3.3 Conclusions 72

3.4 Methods 73

3.4.1 Nanocrystal Synthesis 73

3.4.2 Template Fabrication and Nanocrystal Assembly 73

3.4.3 Structural and Optical Measurements 75

3.4.4 Simulations 76

CHAPTER 4. PLASMONIC OPTICAL AND CHIROPTICAL RESPONSE OF SELF-ASSEMBLED AU NANOROD EQUILATERAL TRIMERS 78

4.1 Introduction 78

4.2 Results and Discussion 79

4.3 Conclusions 93

4.4 Methods 94

4.4.1 Au Nanorod Synthesis 94

4.4.2 Template Fabrication and Nanocrystal Assembly 94

4.4.3 Structural and Optical Measurements 95

4.4.4 Simulations 97

CHAPTER 5. EXTENSIONS AND FUTURE DIRECTIONS 98

5.1 Introduction 98

5.2 Engineering Plasmon Resonances by Tailoring Nanocrystal Separation 98

5.3 Nanocrystal Assembly at Polygon Vertices and Edges 101

5.4 Assembly of Plasmonic Nanocrystals around Post Templates 104

5.5 Three-Dimensional Plasmonic Nanocrystal Clusters 105

5.6 Dielectric-Doped Plasmonic Oligomers 106

5.7 Heterostructures of Plasmonic and Phase-Change Materials 108

5.8 Fractal-Like Assembly of Two-Component Systems 113

5.9 Assembly Yield Optimization 118

5.10 Conclusions **129**

CHAPTER 6. CONCLUDING REMARKS **130**

REFERENCES **131**

LIST OF TABLES

Table 2-1. Nanorod dimensions used for the simulations shown in Figure 2-20. 35

LIST OF FIGURES

Figure 1-1. (a) Transmission electron microscopy (TEM) images of binary nanocrystal superlattices exhibiting structures analogous to the indicated atomic crystal structures. The lattice projection of each image is labeled above the scale bar. Scale bars: 10 nm. Adapted by permission from Macmillan Publishers Ltd from Shevchenko *et al*,[1] © 2006. (b) TEM images and small-angle electron diffraction pattern of a dodecagonal nanocrystal quasicrystal. Adapted by permission from Macmillan Publishers Ltd from Ye *et al*,[2] © 2016.....2

Figure 1-2. Scheme of template-assisted self-assembly, where nanocrystals self-assemble in lithographically defined templates.....4

Figure 1-3. Noble metal nanocrystal building blocks with different geometries: (A) sphere, (B) rod, (C) dog bone, (D) peanut, (E) penta-branch, (F) wire, (G) triangular plate, (H) hexagonal plate, (I) cube, (J) octahedron, (K) cubooctahedron, (L) rhombic dodecahedron, (M) pentagonal bipyramid, (N) star-like octapod, (O) tripod (up) and tetrapod (down), (P) star, (Q) edge truncated octahedron, (R) octapod, (S) core–shell wire/cylinder, (T) tube, (U) cage, (V) double-walled box, (W) core–shell triangular plate, and (X) core–shell cube. Scale bar: 200 nm for A–E, G–I, K, L, P, R and T–V; 1 μm for F and Q; 50 nm for J, M, N, W and X. Figure reprinted from Gong *et al*,[33] © 2012, with permission from Elsevier.....6

Figure 1-4. Schematic illustration of a localized surface plasmon resonance (LSPR) excited by the electric field (E_0) of incident light with wavevector (k). Figure reprinted with permission from Rycenga *et al*.[37] © 2011 American Chemical Society. 7

Figure 1-5. Mass-and-spring model for plasmonic resonances. (a) Sketch of a plasmonic particle whose electron cloud has been displaced by Δx. The resulting positive and negative charges at the ends are treated as point-like charges that possess potential energy due to Coulomb interaction. (b) The resulting oscillation can be modeled by an effective spring constant D and the effective mass m of the moving electron cloud. Figure reproduced from Biagioni *et al*.[38] DOI: 10.1088/0034-4885/75/2/024402. © IOP Publishing. Reproduced with permission. All rights reserved. 7

Figure 1-6. Schematic of plasmon hybridization. In analogy with molecular orbital theory, "bonding" and "antibonding" hybrid plasmon modes result from the coupling of the plasmonic modes of individual nanoparticles. Hybridization results in a "splitting" into new modes having different resonance energies. Figure reprinted with permission from Rycenga *et al*.[37] © 2011 American Chemical Society. 8

Figure 2-1. (a) SEM image of $NaYF_4$:Yb^{3+},Er^{3+} UCNPs. Inset: Schematic depiction of hexagonal prismatic UCNP morphology. (b) Emission spectrum of UCNPs under 977 nm excitation. Peak labels indicate the I: $^2H_{11/2} \rightarrow {}^4I_{15/2}$, II: $^4S_{3/2} \rightarrow {}^4I_{15/2}$, and III: $^4F_{9/2} \rightarrow {}^4I_{15/2}$ transitions of Er^{3+}. (c) TEM image of Au NRs. Inset: Schematic depiction. (d) Extinction spectra of Au NRs (black) and UCNPs (blue). Vertical lines denote the 977 nm excitation (dark red), 660 nm UCNP emission (red), and 545 nm UCNP emission (green). 14

Figure 2-2. Schematic energy level diagram of the upconversion process. Lines indicate photon emission/absorption (solid), non-radiative energy transfer (dashed), and multi-phonon relaxation (dotted).[73] 14

Figure 2-3. (a) Representative SEM image of an empty template defined in SiO_2 (with resist layer visible). (b) Schematic depiction of UCNP assembly via a "squeegee method" in which a polymer wiper sweeps the UCNP solution across the substrate. Not to scale; the UCNPs and template features are enlarged for clarity. (c) SEM image of a single UCNP in a template (after ALD deposition of the SiO_2 overcoat). (d) Schematic of Au NR assembly with an assembly apparatus in which the substrate moves relative to a fixed slide that restrains the Au NR solution. Not to scale. (e) SEM image of a UCNP and Au NR heterodimer structure formed inside the template. Scale bars for SEM: 100 nm. 16

Figure 2-4. SEM images of (a–g) rod–phosphor heterodimers and (h–l) single phosphors. (a–g) and (h–l) correspond respectively to sample labels "A–G" and "H–L" in Figure 2-7c,d. The average rod–phosphor separation measured from (a–g) was 14 ± 5 nm. With a pixel size at this magnification of 1.1 nm, the estimated uncertainty in each individual measurement was ~3 nm. 18

Figure 2-5. (a) Schematic of the PL mapping setup. (b) Spatial map of PL from a single UCNP–NR heterodimer structure. Pixel brightness indicates spectrally integrated PL intensity. (c) 2D Gaussian fit (black contours) superimposed over a contour map of the data in (b). Scale bars in (b) and (c) are 500 nm. 19

Figure 2-6. Representative PL maps of the structures shown in Figure 2-4. (a–l) correspond respectively to sample labels "A–L" in Figure 2-7c,d. Color scale represents integrated intensity in arbitrary units. Maps are cropped to the region over which the 2D Gaussian was fit. 21

Figure 2-7. Inverse-variance weighted average PL intensity for single-phosphor and rod–phosphor structures under longitudinal and transverse laser polarization for power densities of (a) 1.6×10^6 W/cm^2 and (b) 1.6×10^5 W/cm^2. Error bars represent one standard deviation. (c,d) Ratio between PL from longitudinal excitation and transverse excitation for various (c) rod–phosphor (A–G) and (d) single-phosphor (H–

L) structures (representative SEM images inset). High and low power refer to the same power densities as (a) and (b). Error bars represent one standard deviation over at least three measurements for low power and two for high power excitation. 21

Figure 2-8. PL polarization ratio for samples A–G integrated separately over the green and red emission bands. Error bars indicate one standard deviation for multiple measurements. The inverse-variance weighted average and standard deviation among all the samples are presented at the right. 23

Figure 2-9. (a,b) Representative PL spectra from the center of the phosphor under longitudinal (blue) and transverse (red) incident polarization for (a) a single phosphor and (b) a rod–phosphor heterodimer. Each set of curves was normalized so that the transverse curves are of equal height for comparison. Excitation power density was 1.6×10^5 W/cm^2. (c) PL polarization ratio versus excitation power density (log scales) with fit to Eq. 2-1 (blue). Error bars are one standard deviation. 24

Figure 2-10. (a) Photoluminescence spectra collected from a drop-cast film of UCNPs at the indicated excitation power densities (increasing from bottom to top). Spectra were normalized to the maximum of the 660 nm peak. The peaks emerging at high power at 469 and 504 nm have been attributed to higher-excited-state transitions and that at 556 nm to excited-state-to-excited-state transitions.[57] (b) Spectra collected from the same sample at higher spectral resolution to demonstrate the relative growth of the features around 556 nm at increasing power. Spectra were normalized to the height of the left-most peak. 25

Figure 2-11. Power dependence of photoluminescence polarization ratio for (a) a single-phosphor and (b,c) two different additional rod–phosphor structures. Error bars represent one standard deviation for multiple measurements. Green line indicates a ratio of unity. Blue curves are guides to the eye. 27

Figure 2-12. (a) Dependence on excitation power density (P) of the intensity of photoluminescence (PL) collected from a drop-cast film of UCNPs. Data is fit to the form $PL = kP^{C\cdot\log(P)+B}$, with $k = 0.018$, $B = 2.26$, and $C = -0.15$. (b) Left axis: plot of $\log(PL)$ versus $\log(P)$ superimposed with the fit from (a). Right axis: slope of this log–log curve as a function of $\log(P)$. The slope decreases from 1.3 to 0.4 as power is increased. The form of the modified power law is intended to mathematically approximate the observed power dependent behavior over the wide range of power densities used in our study. The underlying physical phenomena are complex and require a detailed understanding of the rates of Yb^{3+} absorption, energy transfer to Er^{3+}, multi-phonon relaxation, and radiative relaxation of Er^{3+}. A recent report by Gargas *et al.*[57] calculated the populations of the Yb^{3+} and Er^{3+} energy states as a function of excitation power density to ascertain the rate-limiting steps for upconversion at different power levels. Pump photon absorption in Yb^{3+} is the

bottleneck at low power densities (where the slope theoretically equals 2) that are typical of ensemble measurements. However, with increasing power into the regime suitable for single particle measurements, insufficient radiative relaxation of Er^{3+} leads to filling of higher-energy states and saturation in the visible upconversion luminescence, as observable as a reduction in the slope and as modeled by our power law. 27

Figure 2-13. Simulated field intensity enhancement maps for (a) transverse and (b) longitudinal excitation polarization. (c,d) Simulated PL enhancement factor as a function of rod–phosphor separation *d* for (c) transverse and (d) longitudinal polarization. (e) Simulated PL polarization ratio as a function of rod–phosphor separation *d*. 29

Figure 2-14. Location of point sources within the phosphor volume used for the simulations. Note that point 4 is located closest to the rod tip. 30

Figure 2-15. Simulated field intensity enhancement as a function of rod–phosphor separation *d* evaluated at the six points indicated in Figure 2-14 for (a) transverse and (b) longitudinal polarization. 30

Figure 2-16. Simulated emission efficiency as a function of rod–phosphor separation *d* evaluated at the six points indicated in Figure 2-14. 32

Figure 2-17. (a) Simulated field intensity enhancement maps for transverse polarization at the indicated polarization misorientation angles. (b) Simulated field intensity enhancement averaged over the six representative points of Figure 2-14 as a function of misorientation angle. 32

Figure 2-18. SEM image of a rod–phosphor structure with a large gap of ~80 nm. 33

Figure 2-19. Simulated PL polarization ratio as a function of rod length. Rod diameter is fixed at 20 nm, and rod–phosphor separation is 15 nm. 34

Figure 2-20. Simulated PL polarization ratio as a function of the overall rod size as pictured in the illustrations and described in Table 2-1. For the chosen rod diameters, the rod length was selected according to Bryant *et al.*[122] to maintain the longitudinal SPR wavelength at 977 nm in order to match the phosphor absorption. Rod–phosphor separation was 15 nm. 35

Figure 3-1. (a) Schematic of plasmonic oligomer metamolecules assembled in polygonal templates. The assemblies contain 1, 7, 13, 19, and 31 NCs. Like colors indicate NCs equidistant from the central NC, forming (light blue) first-, (red) second-, (green) third-, and (dark blue) fourth-nearest neighbor 2D shells. (b) Scanning electron

micrographs of Au NC oligomers formed *via* template-assisted self-assembly, shown after resist liftoff. 45

Figure 3-2. Representative scanning electron microscopy (SEM) image of empty templates defined in poly(methyl methacrylate) (PMMA) resist. The templates shown here have dimensions designed to assemble 31-membered oligomers. Inset: higher-magnification image of the top-right template. 45

Figure 3-3. Transmission electron microscopy (TEM) image of the Au nanocrystals used for assembly. Average nanocrystal diameter is 55 ± 3 nm. 47

Figure 3-4. (a) Cross-sectional schematic of the template-assisted self-assembly process. As the substrate is translated relative to a fixed glass slide, capillary forces at the liquid meniscus direct the NCs to assemble within the templates defined in the resist. (b) Liftoff in acetone removes the resist layer and any stray NCs, leaving behind well-defined Au NC oligomers. 47

Figure 3-5. SEM images of an array of oligomers before and after liftoff. The position and integrity of the oligomers are preserved after liftoff, while the number of stray nanocrystals is reduced. 48

Figure 3-6. Scanning electron micrographs and single-oligomer darkfield scattering spectra of representative 7-, 13-, 19-, and 31-member Au-NC oligomers. Spectra for each different metamolecule configuration collected under p- and s-polarized excitation are presented separately in the left and right panels, respectively, with the color indicating the corresponding SEM image. 49

Figure 3-7. Estimated percent assembly yield for each metamolecule configuration. The average over all the configurations is 14%. A total of 704 template sites is surveyed. A success is scored only if the oligomer possesses exactly the target number of nanocrystals. The yield of templates having a nonzero number of nanocrystals is greater than 90%. 50

Figure 3-8. Schematic depiction of experimental setup, illustrating p- and s-polarization defined by rotating a linear polarizer in the excitation beam. The electric field for p-polarization is primarily out of the plane of the oligomers (with a small in-plane component) while the electric field for s-polarization is completely in plane. The upper row shows a perspective view of the setup, and the lower row illustrates a top view of the sample. 51

Figure 3-9. (a) Average darkfield scattering spectra for each metamolecule configuration under p-polarized excitation, normalized by the number of NCs in the oligomer. (b) Resonance center positions determined from Lorentzian fits over the 500–750 nm range of each of the spectra averaged in (a) as a function of the number of NC shells

(N_S) surrounding the center NC. (c) Average darkfield scattering spectra for each metamolecule configuration under s-polarized excitation, normalized by the number of NCs in the oligomer. (d) Spectral centroid positions determined from each of the spectra averaged in (c) as a function of the number of NC shells. Shaded regions in (a,c) represent the standard error of the mean. Fitting curves in (b,d) are according to Eq. 3-1, and error bars represent one standard deviation. 53

Figure 3-10. A representative scattering spectrum and corresponding Lorentzian fit curve for each metamolecule configuration under p-polarization. The number of nanocrystals in the oligomer is indicated in the legend. Intensity is normalized by the maximum value of each fit curve.....54

Figure 3-11. Calculated average nanocrystal coordination number (black) and experimental average scattering wavelength for p-polarization (blue) as a function of the number of nanocrystal shells in the oligomer. 58

Figure 3-12. Illustration of quantitative image analysis procedure using ImageJ. (a) An SEM image of each oligomer is obtained. (b) A thresholding algorithm is performed to determine the boundaries of each nanocrystal. (c) The center of each nanocrystal is determined using the "ultimate points" command. (d) (x,y) coordinates are determined for each of the numbered nanocrystals using the particle analysis plugin. The coordinates are then entered into a custom MATLAB script to extract information about interparticle distances. 60

Figure 3-13. Correlation coefficient between average scattering spectrum centroid wavelength and four different interparticle distance metrics: first-nearest-neighbor, second-nearest-neighbor, third-nearest-neighbor, and the sum of all interparticle distances.....61

Figure 3-14. (a) Scattering centroid wavelength under s-polarization for seven different 7-member oligomers plotted *versus* the corresponding average nearest-neighbor (NN) interparticle distance within each oligomer. Each 7-member oligomer has 12 unique first-NN NC pairs. (b) Sum of the average first-, second-, and third-NN distances *versus* the number of NC shells (N_S) in each metamolecule configuration. More distant neighbors are excluded since the 7-member oligomers do not have fourth-NN particle pairs. Blue lines in (a) and (b) are linear regressions. 61

Figure 3-15. Individual s-polarized scattering spectra from each metamolecule configuration stacked in order of decreasing first-nearest-neighbor interparticle distance. In general, a red-shift is observed upon decreasing distance. 62

Figure 3-16. Normalized simulated scattering spectrum under p-polarized illumination for each metamolecule configuration. The incident electric field vector is oriented

predominantly orthogonal to the substrate plane. The small shoulder visible in the spectra of the larger oligomers results from phase retardation of the incident plane wave across the lateral extent of the oligomers. 64

Figure 3-17. (a) Simulated normalized scattering cross-section for each metamolecule configuration. (b) Simulated contributions to the scattering cross section of the 13-NC oligomer from electric dipole, magnetic dipole, and electric quadrupole resonances. (c,d) Simulated electric displacement vector maps for the 13-NC oligomer at (c) 700 nm and (d) 1000 nm. Arrows represent an instantaneous spatial distribution of the vector orientations, and the color maps represent the time-averaged values of the vector magnitudes. Schematics below illustrate the combined electric (E)/magnetic (M) dipole nature of the plasmonic response at 700 nm and the predominantly electric dipole response at 1000 nm. All simulation results are shown for s-polarized illumination. 65

Figure 3-18. Experimental (black) and simulated (green) scattering centroid wavelength under s-polarized illumination *versus* oligomer size. Fit curves are performed using Eq. 3-1. The data points for $N_s = 0$ represent the center of Lorentzian fits to the single nanocrystal scattering spectra. Error bars represent one standard deviation. 66

Figure 3-19. Simulated scattering spectra for a 7-membered oligomer under s-polarized illumination as a function of interparticle spacing d. Nanocrystals are modeled as faceted spheres in a surrounding medium of relative permittivity $\varepsilon_r = 2.1$. 66

Figure 3-20. Simulated scattering spectra of a 7-membered oligomer under s-polarized illumination as a function of the relative permittivity ε_r of the surrounding medium. Nanocrystals are modeled as faceted spheres with an interparticle spacing of $d = 2.5$ nm. 67

Figure 3-21. (a) Simulated electric dipole, magnetic dipole, and electric quadrupole contributions to the overall scattering cross section for each metamolecule configuration under s-polarized illumination. (b) Simulated electric displacement vector distributions at the indicated wavelengths. Color scale represents the time-averaged magnitude of the electric displacement. Nanocrystals are the same size in each simulation; figures are scaled for clarity. 69

Figure 3-22. Simulated electric displacement vector maps, scattering spectra, and multipole analysis for (a) an ordered and (b) a disordered 19-NC oligomer under s-polarized illumination. The geometrical arrangement of the particles is extracted from the SEM images of the two experimentally formed oligomers shown. Note that the interparticle spacing for the ordered oligomer is scaled by 5% to avoid overlapping NC volumes in the simulation. 71

Figure 3-23. Experimental (a,b) and simulated (c,d) scattering spectra for the pictured ordered and disordered 19-membered oligomers (also described in Figure 3-22). In both experiment and simulation, the ordered oligomer displays a more red-shifted scattering spectrum centroid than the less ordered oligomer. 72

Figure 4-1. Assembly of one, two, and three Au nanorods along the edges of triangular templates. (a) Schematic representation. (b) Scanning electron microscopy (SEM) images, shown after resist liftoff. 80

Figure 4-2. (a) TEM image of Au nanorods having average length of 110 ± 8 nm and diameter of 22 ± 3 nm. (b) Ensemble extinction spectrum of the nanorods dispersed in water, exhibiting longitudinal and transverse surface plasmon resonances centered at 915 nm and 510 nm, respectively. 80

Figure 4-3. Schematics of the darkfield scattering geometry for p-polarization and s-polarization. (a) Perspective view. (b) Top view. The excitation is incident from left to right. With a 10° incident elevation angle, for p-polarization the electric field is oriented primarily out of the substrate plane with a small in-plane component. For s-polarization, the incident electric field is oriented completely within the plane of the substrate. Note that the in-plane electric field components for p- and s-polarization are orthogonal to each other. 82

Figure 4-4. Darkfield scattering spectra of the structures shown in the inset SEM images: (a) one, (b) two, and (c) three Au nanorods assembled along the edges of a triangular template. Excitation light is incident from the right with either p-polarization (black) or s-polarization (red). Within each panel, intensity is normalized by the peak intensity of the s-polarization spectrum. 84

Figure 4-5. Experimental (red) and simulated (blue) scattering spectra for the Au nanorod trimer shown in the inset SEM image under s-polarized illumination. The intensity of each spectrum is normalized by its maximum value. 87

Figure 4-6. Simulated electric field distributions under s-polarized illumination. The incident electric field is oriented along the *y* direction. Simulations are at the wavelengths of the two scattering features shown in Figure 4-5: (a) 790 nm and (b) 857 nm. The small white arrows indicate the direction of the electric displacement field. The overlay of black arrows in (a) emphasizes the head-to-head configuration of electric dipoles, while the field map in (b) is more ambiguous to assign. 87

Figure 4-7. Darkfield scattering spectra of the Au nanorod trimer structures shown in the inset SEM images. Excitation light is incident from the right with either p-polarization (black) or s-polarization (red). Labels of L, R, and A refer to designations as left-enantiomer, right-enantiomer, and achiral structures. 89

Figure 4-8. Schematic depiction of an achiral nanorod trimer and left-handed and right-handed 2D chiral enantiomers. The choice of L *versus* R as the designation is arbitrary. 90

Figure 4-9. Polar plots of illumination intensity as a function of the rotation of an analyzer polarizer placed after the quarter wave plate. Residual ellipticity in the LCP and RCP illumination is low, as desired. 91

Figure 4-10. (a) Scattering spectra under left-circular and right-circular polarized illumination and (b) percent CDS spectrum for the structure pictured in the inset SEM image. The excitation is incident from the right. 92

Figure 4-11. Percent CDS spectrum averaged over azimuthal rotations of the sample in 30° increments through a full 360° rotation. 93

Figure 5-1. Scanning electron microscopy (SEM) images of Au nanocrystals with the same size (55 nm diameter) but different surface coatings: CTAB (left) and SiO_2 (right). 100

Figure 5-2. SEM images of Au@SiO_2 nanocrystals assembled at the vertices (top row) and edges (bottom row) of templates with 2-, 3-, 4-, 5-, and 6-fold rotational symmetries. 101

Figure 5-3. Template designs for six-fold symmetric polygons ranging from a “regular polygon” (left) to a “star polygon” (right). 102

Figure 5-4. SEM images of nanocrystals assembled at the vertices of square templates having two different sizes. 102

Figure 5-5. SEM images of Au nanocrystals assembled in 5-fold symmetric templates. 103

Figure 5-6. (a) SEM image of nanocrystals assembled into a close-packed structure with approximately 5-fold rotational symmetry, enabled by the small size of the central nanocrystal. (b) Overlay of an ideal 5-fold symmetric pattern. 103

Figure 5-7. SEM images of Au@SiO_2 nanocrystals assembled around PMMA post templates. 105

Figure 5-8. SEM image of Au@SiO_2 nanocrystals assembled within an annular template. 105

Figure 5-9. (a) Schematic and (b) SEM images of 3D tetrahedral Au nanocrystal assemblies formed through templated assembly. 106

Figure 5-10. (a) Schematic of a large nanocrystal oligomer, whose optical response approximates that of an infinite array of nanocrystals. (b) Schematic of introducing a dielectric nanoparticle "dopant" into a metal nanocrystal oligomer. 107

Figure 5-11. SEM image of a random co-assembly of Au nanocrystals (bright) and SiO_2 nanoparticles (gray) on an unstructured substrate. Insets show magnified regions...108

Figure 5-12. SEM image of pillars formed through templated assembly of VO_x nanocrystals before rapid thermal annealing. Sample is tilted by 20°. 110

Figure 5-13. SEM image of pillars formed through templated assembly of VO_x nanocrystals (a) before and (b) after rapid thermal annealing. Sample in (a) is tilted by 30°. 110

Figure 5-14. (a) Representative AFM image of VO_2 pillars after rapid thermal annealing. (b) Height profile across the line indicated in (a) showing a height of approximately 20 nm. (c) 3D rendering of the pillar structures. 111

Figure 5-15. SEM images of pillars formed through assembly of VO_x nanocrystals into templates etched into SiO_2 using a PMMA mask (a) before and (b) after rapid thermal annealing. 112

Figure 5-16. (a) Solution-phase absorption spectrum of ICO nanocrystals. (b) SEM image of a PMMA pillar decorated with ICO nanocrystals. 113

Figure 5-17. Fractal geometries. (a) Sierpinski triangle. (b) Apollonian gasket. 114

Figure 5-18. SEM images of (a) an empty triangular template, (b) a single 510 nm hexagonal $NaYF_4:Er^{3+},Yb^{3+}$ nanocrystal assembled in a triangular PMMA template, and (c) $Au@SiO_2$ nanocrystals co-assembled with a $NaYF_4:Er^{3+},Yb^{3+}$ nanocrystal. 115

Figure 5-19. (a) SEM image of an empty triangular template etched in SiO_2. (b-d) SEM images of the self-similar filling of a triangular template with a 265 nm hexagonal $NaYF_4:Er^{3+},Yb^{3+}$ nanocrystal and (b) one, (c) two, and (d) three $Au@SiO_2$ nanocrystals. 115

Figure 5-20. SEM images of (a) the filling of a triangular template etched in SiO_2 with a $NaYF_4:Er^{3+},Yb^{3+}$ nanocrystal and two $Au@SiO_2$ nanocrystals at each vertex and (b) filling of a triangular template with a triangular arrangement of $Au@SiO_2$ nanocrystals. 116

Figure 5-21. Schematic of the self-similar filling of templates with spheres having a size ratio 2.75:1. 117

Figure 5-22. SEM images of (a) 55 nm and 20 nm Au nanocrystals, (b) an empty circular template, (c) a single 55 nm Au nanocrystal assembled in a template, (d) a 55 nm and a 20 nm Au nanocrystal co-assembled in a template, and (e) a trimer of 55 nm Au nanocrystals. The structure in (e) is shown after resist liftoff. 118

Figure 5-23. Schematic illustrating several of the factors influencing the performance of template-assisted self-assembly. 119

Figure 5-24. Side-view photographs of three different nanocrystal assembly methods..120

Figure 5-25. (a) Estimated percent assembly yield as a function of substrate withdrawal velocity in the capillary assembly of Au nanocrystals. (b,c) SEM images of assemblies with substrate velocities of 2 μm/s and 8 μm/s, respectively. 121

Figure 5-26. (a) Estimated percent assembly yield of Au nanocrystals with 55 nm diameter in PMMA templates of varying depths. (b,c) Schematic depictions of nanocrystals in (b) deep and (c) shallow templates. 122

Figure 5-27. (a,b) SEM images of circular templates (a) before and (b) after reactive ion etching. (c,d) AFM images of the templates in (a) and (b), respectively. Note the increased roughness after etching. 123

Figure 5-28. SEM images and yield statistics for assemblies performed using nanocrystal solutions with the two indicated dilution ratios. 124

Figure 5-29. Aqueous-phase absorption spectrum of the Au nanocrystal solution referenced as “1:5 dilution from stock” in Figure 5-28. 124

Figure 5-30. SEM images and yield statistics for assemblies using nanocrystal solutions having the same concentration, but either freshly diluted before assembly or stored in dilute form. 125

Figure 5-31. SEM images and yield statistics for assemblies prepared at the indicated temperature offsets above the dew point (DP) temperature. 126

Figure 5-32. (a) Brightfield optical microscope, (b) darkfield optical microscope, and (c) scanning electron microscope images of platelets observed to form at low Au nanorod solution temperatures. 127

Figure 5-33. SEM secondary electron (SE) image and energy dispersive x-ray spectroscopy (EDS) elemental analysis maps of the platelets shown in Figure 5-32. Note that the Al signal for the platelets is likely to be actually from Br Lα signal (1.480 keV), which overlaps with the energy of Al Kα signal (1.486 keV). 127

Figure 5-34. (a) Assembly yield statistics for four different samples after a 1st and 2nd deposition of nanocrystals. (b) SEM images of the same field of view after a 1st and 2nd deposition of nanocrystals. 128

CHAPTER 1. INTRODUCTION

1.1 Nanocrystal Assemblies: a New Paradigm for Materials Design

The construction of materials from nanocrystal building blocks represents an exciting new paradigm for materials design. Just as nature's materials orchestrate intricate combinations of atoms from the library of the periodic table, nanocrystal "metamaterials" integrate individual nanocrystals into larger architectures with emergent collective properties. As illustrated in Figure 1-1, nanocrystals can assemble into superlattices having periodic structures that are direct analogues of the crystal structures familiar from atomic crystals (Figure 1-1a) as well as quasiperiodic structures with quasicrystalline ordering (Figure 1-1b).[1,2]

Nanocrystal metamaterials offer the opportunity for hierarchical materials engineering, where structure and properties are designed on multiple length scales. The individual nanocrystal "meta-atoms" that make up these materials are themselves each a nanoscale atomic system with tailorable size, shape, and elemental composition. The identity, organization, and interaction of these individual meta-atoms determine the global properties of the metamaterial assembly.

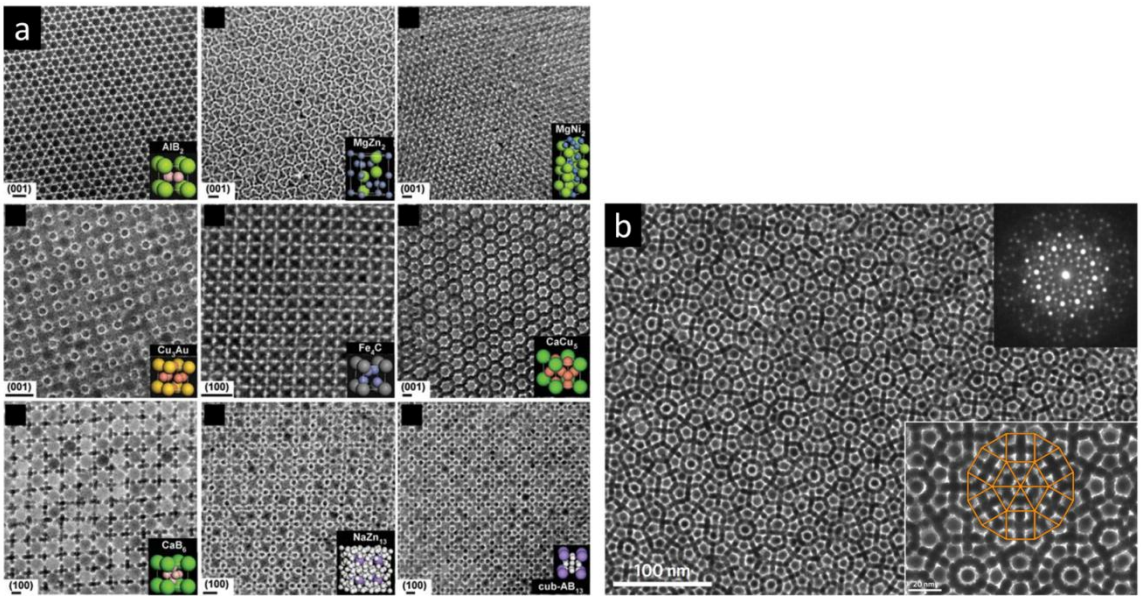

Figure 1-1. (a) Transmission electron microscopy (TEM) images of binary nanocrystal superlattices exhibiting structures analogous to the indicated atomic crystal structures. The lattice projection of each image is labeled above the scale bar. Scale bars: 10 nm. Adapted by permission from Macmillan Publishers Ltd from Shevchenko *et al*,[1] © 2006. (b) TEM images and small-angle electron diffraction pattern of a dodecagonal nanocrystal quasicrystal. Adapted by permission from Macmillan Publishers Ltd from Ye *et al*,[2] © 2016.

A full and fundamental understanding of inter-nanocrystal coupling is therefore necessary in order to move beyond initial structural demonstrations and toward generating metamaterials with tangible functionality. By studying the behavior of small groupings of nanocrystals, we can uncover essential insights into the physics of how the cooperative interactions within small "unit cells" or "nanocrystal metamolecules" give rise to their collective properties. These metamolecules can be utilized for their individual properties as well as integrated into larger multifunctional devices. Characterizing and optimizing metamolecule properties will allow them to be harnessed for applications

spanning energy conversion, light manipulation, biomedicine, catalysis, and information processing.[3]

1.2 Template-Assisted Self-Assembly

Motivated by the desire to measure, understand, and engineer the coupling in nanocrystal metamolecules, the need for methods to form precise arrangements of nanocrystals continues to grow. Nanocrystal self-assembly[4] offers a powerful "bottom-up" approach in which the energetic, entropic, and kinetic conditions are carefully set up to then "let nature do its work" to assemble the structures.[5] While the structural diversity achievable by self-assembly is impressive, the ability to assemble an arbitrarily designed architecture to suit the requirements of a specific application remains limited. Approaching the goal of nanoscale patterning from a different direction, "top-down" methods such as lithography provide far greater flexibility in design. However, these methods are restricted by the size resolution of the nanofabrication tools and often involve time-consuming and expensive serial patterning mechanisms.

At the intersection of the "top-down" and "bottom-up" paradigms, template-assisted self-assembly combines the advantages of each approach while overcoming many of their individual limitations (Figure 1-2). Here, nanocrystals are directed to assemble into templates defined using lithography. Incorporating lithography enables precise control over the location of the nanostructure and the freedom to make patterns with arbitrary designs. Then, by accessing the extensive library of chemically-synthesized nanocrystals, which are prepared in large quantities in a highly-parallel manner, we can

utilize their tailorable properties by assembling them into functional arrangements within the templates.

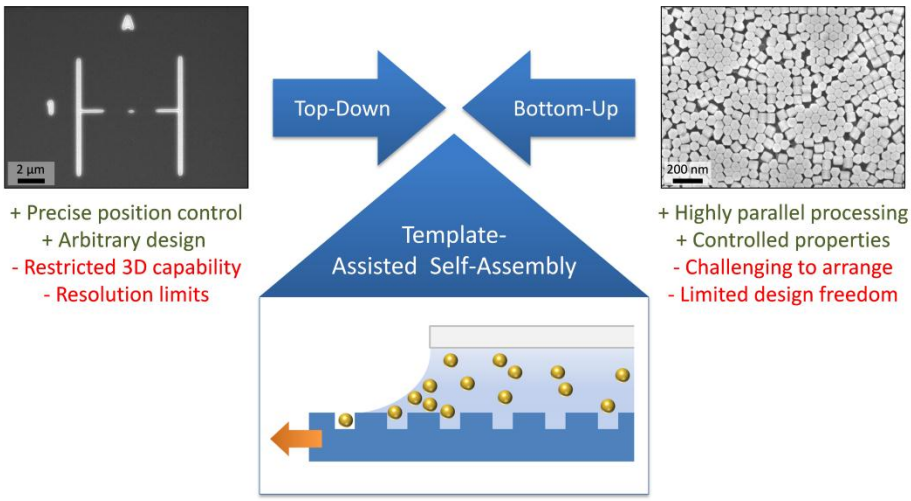

Figure 1-2. Scheme of template-assisted self-assembly, where nanocrystals self-assemble in lithographically defined templates.

Progress in assembling nanoscale materials using templated assembly builds upon the early foundation of the approach in assembling micrometer-scale colloidal particles.[6] These microscale experiments highlighted design strategies for templating small planar clusters of silica and polystyrene spheres, including heterodimers of two sphere types as well as 3D clusters.[7–11] By pushing the template sizes to ever-smaller dimensions, nanosized components were soon integrated into templates.[12,13] Because the magnitude of the capillary force directing the particle assembly diminishes with reduced particle size,[12] an understanding of the role of experimental parameters such as temperature, substrate velocity, and wetting properties in achieving high placement yield has been a significant contribution.[14,15] While the assembly of anisotropic and faceted nanocrystals into shape-matched templates had been discussed,[16] nearly all studies focused on spherical particles

until Kuemin *et al.*'s demonstration of the high-yield placement of gold nanorods into large-area arrays of circular holes,[17] followed up by the oriented assembly of nanorods using rectangular templates.[18] Employing shape-selective templates to impart geometrical control over nanocrystal arrangement remains a powerful strategy for future implementations of template-assisted self-assembly,[19–21] and successful experiments continue to motivate theoretical studies exploring the physical mechanisms underlying the approach.[22–24]

Templated assembly has been especially powerful for studying the interactions among plasmonic nanocrystals, as highlighted in this dissertation and reported by others in the literature.[19,25–30] To provide context for this discussion, a brief introduction to plasmonic nanocrystals is given in the following section.

1.3 Plasmonic Nanocrystals

Through the efforts of the synthesis community, an ever-expanding library of noble metal nanocrystal components is available, as highlighted in Figure 1-3. When these nanoscale, sub-wavelength structures interact with light, collective oscillations of the free electrons can arise in resonance with the oscillating electromagnetic fields of the excitation light. These oscillations, referred to as localized surface plasmon resonances,[31,32] are manifested in the far-field as spectral features of enhanced extinction and in the near-field as spatially-localized regions of enhanced electric field intensity surrounding the plasmonic structure.

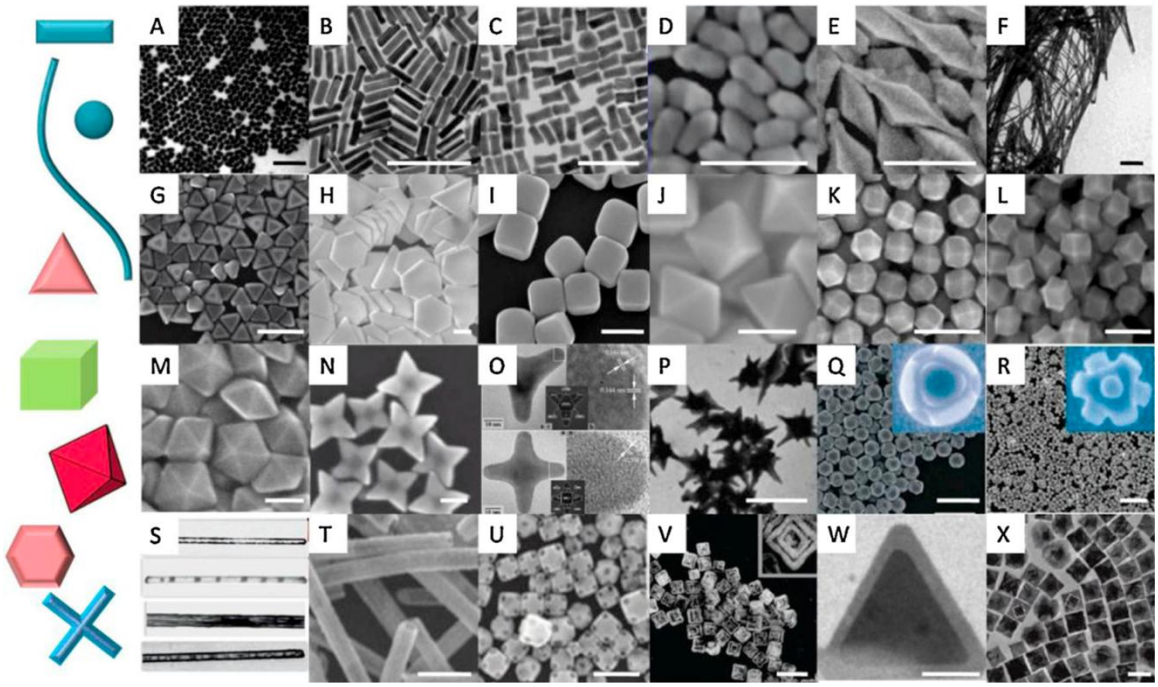

Figure 1-3. Noble metal nanocrystal building blocks with different geometries: (A) sphere, (B) rod, (C) dog bone, (D) peanut, (E) penta-branch, (F) wire, (G) triangular plate, (H) hexagonal plate, (I) cube, (J) octahedron, (K) cubooctahedron, (L) rhombic dodecahedron, (M) pentagonal bipyramid, (N) star-like octapod, (O) tripod (up) and tetrapod (down), (P) star, (Q) edge truncated octahedron, (R) octapod, (S) core–shell wire/cylinder, (T) tube, (U) cage, (V) double-walled box, (W) core–shell triangular plate, and (X) core–shell cube. Scale bar: 200 nm for A–E, G–I, K, L, P, R and T–V; 1 μm for F and Q; 50 nm for J, M, N, W and X. Figure reprinted from Gong *et al*,[33] © 2012, with permission from Elsevier.

A simple depiction of the excitation of a surface plasmon resonance is shown in Figure 1-4, illustrating the positive and negative surface charge distributions caused by the incident light. The restoring force counteracting this charge distribution sets up a resonant harmonic oscillation, analogous to the classical mass-on-a-spring system (Figure 1-5). The nature of this resonance (*e.g.* its center frequency and broadness) is determined by the plasmonic nanostructure's material composition,[34] size,[35] and shape,[36] enabling

plasmon resonances to be tuned across the ultraviolet–visible–near-infrared electromagnetic spectrum.

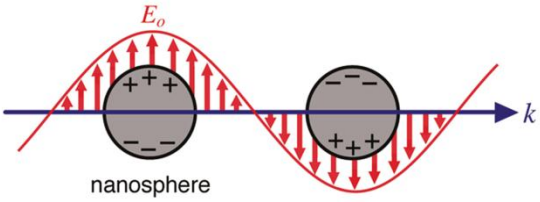

Figure 1-4. Schematic illustration of a localized surface plasmon resonance (LSPR) excited by the electric field (E_0) of incident light with wavevector (k). Figure reprinted with permission from Rycenga *et al*.[37] © 2011 American Chemical Society.

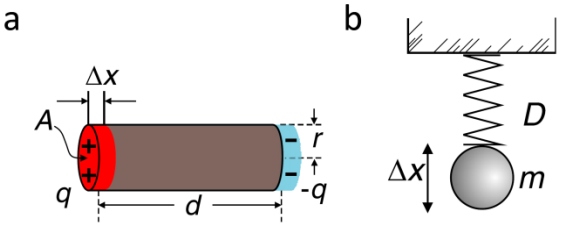

Figure 1-5. Mass-and-spring model for plasmonic resonances. (a) Sketch of a plasmonic particle whose electron cloud has been displaced by Δx. The resulting positive and negative charges at the ends are treated as point-like charges that possess potential energy due to Coulomb interaction. (b) The resulting oscillation can be modeled by an effective spring constant D and the effective mass m of the moving electron cloud. Figure reproduced from Biagioni *et al*.[38] DOI: 10.1088/0034-4885/75/2/024402. © IOP Publishing. Reproduced with permission. All rights reserved.

Another means to engineer the plasmonic response is to combine multiple plasmonic components together to form a coupled plasmonic system. As pictured in Figure 1-6, individual plasmon modes can interact to form new hybridized modes at different energies, analogous to hybridization in molecular orbital theory.[39] Understanding the collective plasmonic response of coupled multi-component structures,

including phenomena such as Fano interference[40] and the generation of magnetic plasmon resonances,[41] remains an active area of plasmonics research.[42] For additional information on plasmonics and its applications in photovoltaics,[43] optical circuitry,[44] biosensing,[45] catalysis,[46] superlens imaging,[47] and optical invisibility cloaking,[48] the reader is referred to several comprehensive books and review articles.[31,32,42,49]

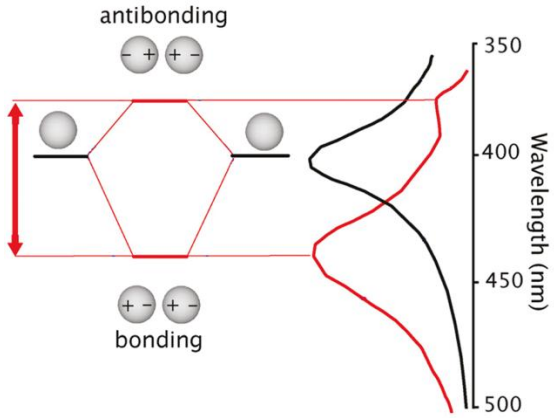

Figure 1-6. Schematic of plasmon hybridization. In analogy with molecular orbital theory, "bonding" and "antibonding" hybrid plasmon modes result from the coupling of the plasmonic modes of individual nanoparticles. Hybridization results in a "splitting" into new modes having different resonance energies. Figure reprinted with permission from Rycenga *et al.*[37] © 2011 American Chemical Society.

1.4 Outline of Dissertation Chapters

In this dissertation, we present several strategies to engineer and exploit plasmonic coupling in nanocrystal metamolecules assembled using template-assisted self-assembly and characterized by spatially-resolved structural and spectroscopic techniques.

In Chapter 2, we utilize template-assisted self-assembly to form discrete nanocrystal heterodimers consisting of a single upconversion nanophosphor and a single gold nanorod. By matching the surface plasmon resonance of the nanorods with the

excitation wavelength of the phosphors and by spatially localizing the phosphors in the intense near-fields surrounding the rod tips, several-fold luminescence enhancements are achieved.

Chapter 3 explores the evolution of plasmonic modes in two-dimensional Au nanocrystal oligomer metamolecules as the number of nanocrystals is systematically varied. Darkfield scattering spectroscopy of individual self-assembled oligomers in combination with theoretical simulations is used to map the wavelength and character of plasmonic modes as a function of metamolecule size and degree of disorder in nanocrystal packing.

In Chapter 4, Au nanorods are self-assembled into equilateral triangle configurations, and their collective plasmonic optical and chiroptical response is measured and simulated. We explore the interplay of magnetic and electric plasmon modes in the structure, as well as the role of geometric chirality in determining the enantioselective response to circularly polarized light.

Chapter 5 offers several extensions and future directions of our self-assembly and materials design strategy. These include further engineering nanocrystal assembly geometry and interparticle separation and forming assemblies in three dimensions. Extensions incorporating multiple types of nanocrystals into a single structure include dielectric-doped plasmonic oligomers, phase-change heterostructures, and self-similar, fractal-like configurations. Strategies to optimize assembly yield are discussed, before concluding the dissertation in Chapter 6.

CHAPTER 2. PLASMON-ENHANCED UPCONVERSION LUMINESCENCE IN SINGLE NANOPHOSPHOR–NANOROD HETERODIMERS FORMED THROUGH TEMPLATE-ASSISTED SELF-ASSEMBLY[1]

2.1 Introduction

Upconversion phosphors are an attractive class of materials with the ability to absorb low-energy light and re-emit light having higher energy.[50–57] This property has made spectral upconverters attractive for a number of applications including photovoltaics,[58–61] bioimaging and therapy,[62–66] solid state lighting,[67] and display technologies.[68,69] For example, solar cell efficiency could be improved by extending the usable portion of the solar spectrum by upconverting sub-band-gap infrared light that is otherwise lost. As contrast agents in biological systems, upconverters enable the use of low-power, infrared excitation, which offers reduced autofluorescence background while penetrating more deeply and with less damage to tissue. While developments in these application areas are promising, widespread implementation of upconversion materials remains limited by the low efficiency of the upconversion process. Even for the most

[1] Much of this chapter appears in print: Adapted with permission from Greybush, N. J.; Saboktakin, M.; Ye, X.; Della Giovampaola, C.; Oh, S. J.; Berry, N. E.; Engheta, N.; Murray, C. B.; Kagan, C. R. *ACS Nano* **2014**, *8*, 9482–9491. DOI: 10.1021/nn503675a © 2014 American Chemical Society.

effective materials, such as hexagonal (β) phase $NaYF_4$ nanocrystals co-doped with Yb^{3+} and Er^{3+}, the quantum yield is often below 1%,[70–72] motivating the development of routes to enhance upconversion luminescence.

One approach to enhance upconversion is to explore chemical design strategies such as tailoring the doping level, host material and phase, and nanocrystal morphology.[73–78] An alternative, parallel strategy involves enhancing the luminescence of phosphors through coupling to plasmonic nanostructures. The collective oscillations of conduction electrons within nanoscale metal structures, known as surface plasmon resonances (SPRs), can greatly amplify the luminescence from nearby emitters,[31] as extensively demonstrated for semiconductor quantum dot[79–81] and single molecule[82–84] fluorescence. A number of recent studies have explored plasmonic enhancement of upconversion nanophosphors (UCNPs) with strategies including assembling UCNPs with Au and Ag nanoparticles,[85–90] placing UCNPs near structured metal surfaces,[91–97] and employing core-shell architectures with either plasmonic cores[98,99] or shells.[100–105] However, single-particle optical studies of UCNPs[57,106–109] and their plasmon-enhanced luminescence[86,100,105] remain limited. Single-particle measurements are valuable in complementing studies on ensembles of UCNPs, as ensemble heterogeneities in the upconverting and plasmonic components and in their spatial arrangement can obscure the underlying physics of their coupling. The sensitivity of luminescence enhancement to design parameters is more easily uncovered using single-particle experiments, enabling

the optimization of a model unit structure that can be extended to a useful large-scale system.

Single-particle studies of plasmon-coupled UCNPs require a robust means to precisely assemble a desired structure for optical characterization. While previous experiments have used, for example, manual manipulation of individual nanocrystals with an atomic force microscope (AFM) tip,[86] a method to self-assemble pre-designed structures with controlled orientation is highly advantageous. Template-assisted self-assembly[8,11] fulfills this need by combining the design freedom of lithography with the highly parallel nature of self-assembly. In this approach, chemically synthesized components are made to assemble within topographical features defined on a substrate by lithography. This technique has been used to successfully assemble micron-[7–9,11] and nano-sized[11,12,14,15,17,18,28,29,91,110–114] particles for applications including plasmonics,[28,29,113,114] surface-enhanced Raman scattering,[111] and nanoelectronics,[12] and was recently employed for the placement of UCNPs into gold nanohole arrays for luminescence enhancement.[91] In the present work, we utilize template-assisted self-assembly to form discrete nanocrystal heterodimers consisting of a single UCNP and a single gold nanorod (Au NR). These individual unit structures are assembled in well-defined locations and orientations on the substrate, enabling us to investigate the magnitude of plasmonic enhancement by studying the polarization- and power-dependent luminescence properties of individual UCNPs in the presence and absence of Au NRs.

2.2 Results and Discussion

The nanocrystal building blocks used in our study are shown in Figure 2-1. We synthesized UCNPs composed of hexagonal (β) phase $NaYF_4$ co-doped with Yb^{3+} and Er^{3+} that are hexagonal prismatic in shape with an average height of 61 nm ±5% and face diagonal of 66 nm ±4% (Figure 2-1a). In this UCNP system, incident light at 977 nm resonantly excites the $^2F_{7/2} \rightarrow {}^2F_{5/2}$ transition in Yb^{3+}, and this energy is subsequently transferred non-radiatively to nearby Er^{3+} ions through a series of energy transfer and phonon relaxation steps to populate the emitting states of Er^{3+}, as shown in Figure 2-2. The visible emission spectrum (Figure 2-1b) displays three major upconversion emission bands centered around (I) 525, (II) 545, and (III) 660 nm, corresponding to transitions from the $^2H_{11/2}$, $^4S_{3/2}$, and $^4F_{9/2}$ states to the $^4I_{15/2}$ ground state of Er^{3+}, respectively. Au NRs were synthesized with an average length of 109 nm ±8% and width of 20 nm ±9% (Figure 2-1c). This Au NR aspect ratio was targeted specifically so that the broad SPR spectrally overlaps the UCNP excitation. Figure 2-1d illustrates that the main spectral feature in the Au NR extinction around 975 nm, the longitudinal SPR resulting from excitation along the long axis of the rod, coincides with the $^2F_{7/2} \rightarrow {}^2F_{5/2}$ absorption in Yb^{3+} as desired.

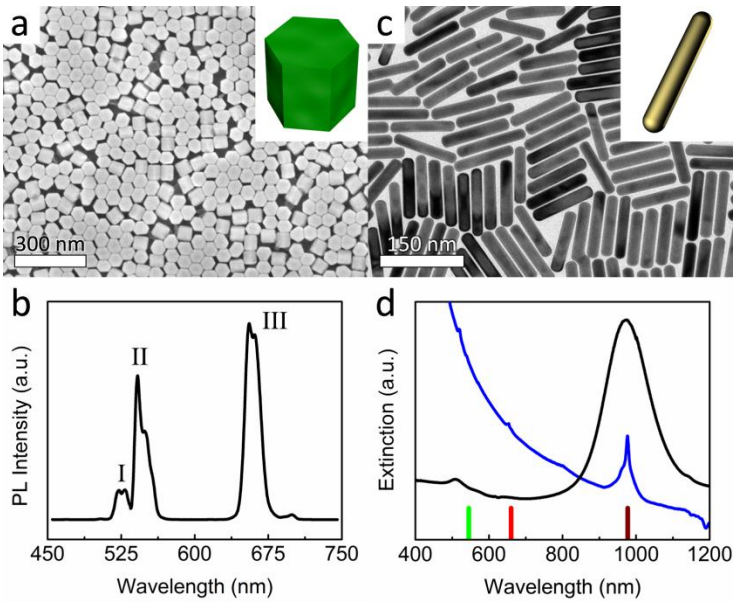

Figure 2-1. (a) SEM image of $NaYF_4:Yb^{3+},Er^{3+}$ UCNPs. Inset: Schematic depiction of hexagonal prismatic UCNP morphology. (b) Emission spectrum of UCNPs under 977 nm excitation. Peak labels indicate the I: $^2H_{11/2} \rightarrow {}^4I_{15/2}$, II: $^4S_{3/2} \rightarrow {}^4I_{15/2}$, and III: $^4F_{9/2} \rightarrow {}^4I_{15/2}$ transitions of Er^{3+}. (c) TEM image of Au NRs. Inset: Schematic depiction. (d) Extinction spectra of Au NRs (black) and UCNPs (blue). Vertical lines denote the 977 nm excitation (dark red), 660 nm UCNP emission (red), and 545 nm UCNP emission (green).

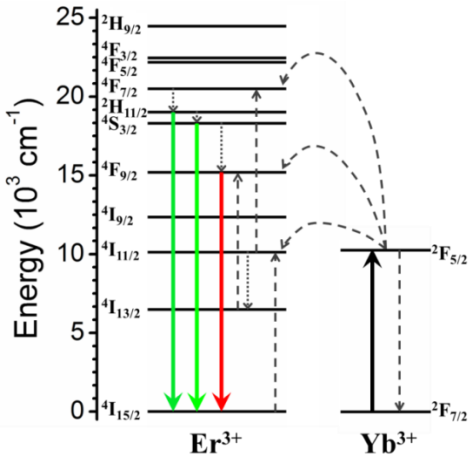

Figure 2-2. Schematic energy level diagram of the upconversion process. Lines indicate photon emission/absorption (solid), non-radiative energy transfer (dashed), and multi-phonon relaxation (dotted).[73]

This spectral overlap is critical in determining the nature, if any, of plasmonic luminescence enhancement. In general, the presence of a plasmonic structure can affect the luminescence of a nearby emitter in two ways.[115] First, the highly concentrated electric fields surrounding the plasmonic structure can increase the excitation rate of the emitter. Second, the quantum yield of the emitter can also be modified to enhance (or quench) the emission. Excitation and quantum yield enhancement are sensitive, respectively, to the spectral overlap of the plasmon resonance with the excitation and the emission wavelengths of the luminophore.[116,117] In our system we therefore are targeting excitation enhancement and expect limited contribution from quantum yield enhancement.

In addition to spectral overlap, effective plasmon-enhanced excitation requires spatial localization of the UCNP within the enhanced near-fields surrounding the plasmonic structure. We therefore employed a template-assisted self-assembly technique to generate spatially well-defined pairs of UCNPs and Au NRs as illustrated in Figure 2-3. First, a series of short trenches was patterned in SiO_2 on a silicon substrate by electron-beam lithography and reactive ion etching. The shape of these topographical templates was finely tuned so that the central portion could only accept one UCNP per template and the extended arms of the template were suitable for accepting individual Au NRs. The SEM image in Figure 2-3a shows a representative template structure following resist development and etching. To assemble the UCNPs into the templates, we employed a “squeegee method” previously demonstrated by our group for the assembly of

UCNPs.[91,118] As pictured schematically in Figure 2-3b, a drop of UCNPs in hexanes was placed on the templated area and then swept across the surface using a flexible piece of polydimethylsiloxane (PDMS), driving the UCNPs at the liquid meniscus downward into the depressions. The resist layer was then removed, clearing away any UCNPs deposited nonspecifically outside the templates. Next, a thin (6 nm) layer of SiO_2 was deposited on the surface using atomic layer deposition (ALD). This layer served a dual purpose: (1) it prevented the Au NRs from approaching too closely to the phosphor and quenching the emission[85] and (2) it secured the UCNPs in place while the Au NRs were being assembled. A representative SEM image of a single-phosphor structure after ALD is shown in Figure 2-3c.

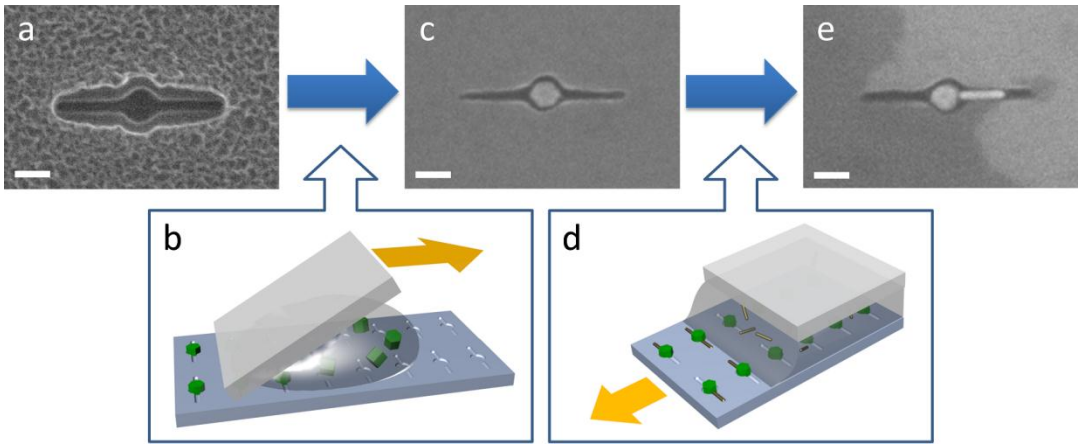

Figure 2-3. (a) Representative SEM image of an empty template defined in SiO_2 (with resist layer visible). (b) Schematic depiction of UCNP assembly via a "squeegee method" in which a polymer wiper sweeps the UCNP solution across the substrate. Not to scale; the UCNPs and template features are enlarged for clarity. (c) SEM image of a single UCNP in a template (after ALD deposition of the SiO_2 overcoat). (d) Schematic of Au NR assembly with an assembly apparatus in which the substrate moves relative to a fixed slide that restrains the Au NR solution. Not to

scale. (e) SEM image of a UCNP and Au NR heterodimer structure formed inside the template. Scale bars for SEM: 100 nm.

While the squeegee method was effective for the assembly of UCNPs dispersed in alkanes, the Au nanorods were dispersed in water, and matching the rate of manual translation of the PDMS wiper with the slow water evaporation rate was more challenging. However, recent successful demonstrations of Au NR templated assembly using capillary action[17,18,112] motivated us to construct our own home-built apparatus (Figure 2-3d) to use this approach for Au NR assembly. Briefly, a dispersion of Au NRs was sandwiched between a fixed glass slide and the substrate, which was mounted on a linear translation stage. As the substrate was slowly moved relative to the fixed slide, the meniscus of the Au NR solution was drawn across the templates, and capillary force directed the rods into their intended positions adjacent to the UCNPs. Figure 2-3e shows a representative SEM image of a rod–phosphor dimer formed using this assembly method. Additional SEM images are provided in Figure 2-4. For the heterodimers selected for photoluminescence measurements, the average distance from the rod tip to the UCNP was 14 ±5 nm. While we are still optimizing the capillary assembly of nanocrystals in our lab, our co-assembly scheme successfully demonstrates shape-selective assembly wherein nanocrystal components are directed with high specificity into template features corresponding to their size and aspect ratio.

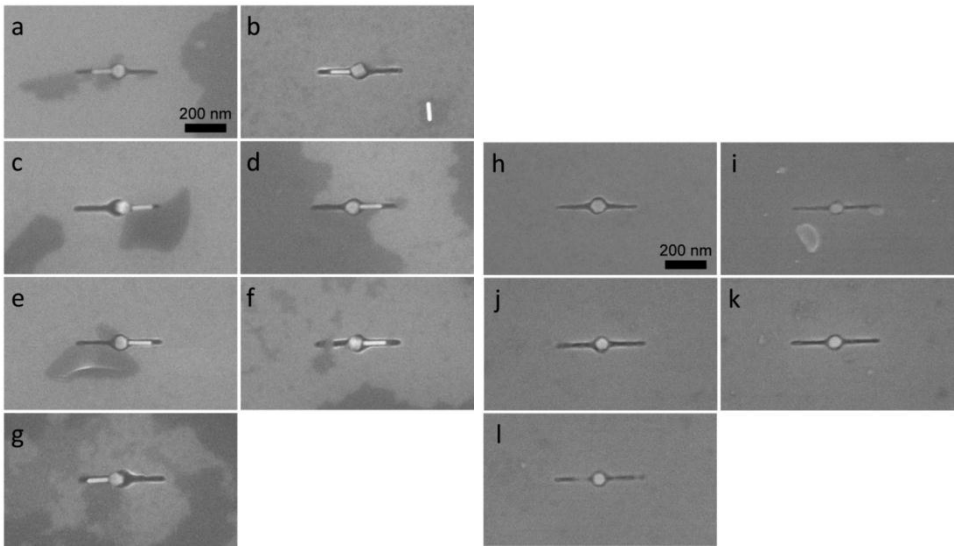

Figure 2-4. SEM images of (a–g) rod–phosphor heterodimers and (h–l) single phosphors. (a–g) and (h–l) correspond respectively to sample labels “A–G” and “H–L” in Figure 2-7c,d. The average rod–phosphor separation measured from (a–g) was 14 ± 5 nm. With a pixel size at this magnification of 1.1 nm, the estimated uncertainty in each individual measurement was ~3 nm.

The photoluminescence (PL) of the UCNPs and the UCNP–NR heterodimers was studied by scanning, confocal, PL microscopy using the setup depicted in Figure 2-5a. The sample was mounted on the piezoelectric translation stage of an optical microscope and rastered in two dimensions under a diffraction-limited 977 nm laser excitation spot focused by the microscope objective. The upconverted emission was collected by the objective, transmitted through a dichroic beamsplitter that filtered out reflected excitation light, and focused onto an optical fiber that carried the light to a spectrometer coupled with a CCD camera for detection. Importantly, a half-wave plate in the laser beam path allowed us to orient the laser’s linear polarization direction along either the Au NR’s long or short axis. The laser power was maintained at a desired constant value for the duration

of a measurement by a feedback loop that sampled the beam power and automatically adjusted the laser output *via* rotation of a gradient neutral density filter.

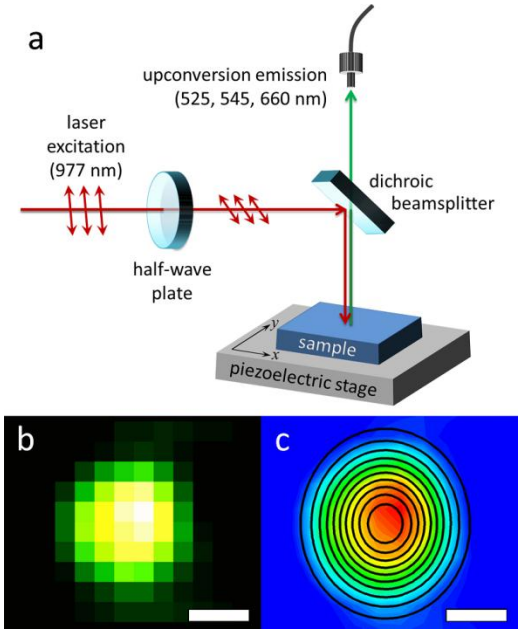

Figure 2-5. (a) Schematic of the PL mapping setup. (b) Spatial map of PL from a single UCNP–NR heterodimer structure. Pixel brightness indicates spectrally integrated PL intensity. (c) 2D Gaussian fit (black contours) superimposed over a contour map of the data in (b). Scale bars in (b) and (c) are 500 nm.

By measuring the PL at each point in the raster, spatial maps of PL intensity could be generated, as shown in Figure 2-5b. In this representation, the color intensity of each pixel indicates the total detected PL, spectrally integrated over all three major emission bands at 525, 545, and 660 nm. Because of the small size of the diffraction-limited laser spot (~1.5 μm diameter) relative to the separation between individual structures on the substrate (~13.5 μm), PL maps of individual single-phosphor and rod–phosphor structures could be acquired. While the structures themselves were too small to be

resolved in the optical microscope, alignment marks patterned in the periphery allowed specific structures to be located and mapped after their characterization by SEM. The PL maps were fit to a 2D Gaussian function (Figure 2-5c) whose height was used to quantify the PL intensity for a given measurement.

PL measurements were taken for several examples each of single-phosphor and rod–phosphor structures to generate statistics of the luminescence enhancement. A representative PL map for each structure measured is provided in Figure 2-6. Figure 2-7a presents the inverse-variance weighted average value of PL intensity for these two structure types under longitudinally and transversely oriented laser excitation with a power density of 1.6×10^6 W/cm^2. The presence of the Au NR was found to enhance the luminescence intensity by factors of 1.9 and 1.5 for the longitudinal and transverse polarizations, respectively. Figure 2-7b shows measurements of the same structures when the laser power was reduced by a factor of ten to 1.6×10^5 W/cm^2. In the low-power case, enhancement factors of 2.5 for longitudinal and 1.4 for transverse polarization were observed. It is important to note that these measurements encompass variations among samples in phosphor and rod size and in their separation, as discussed in more detail below.

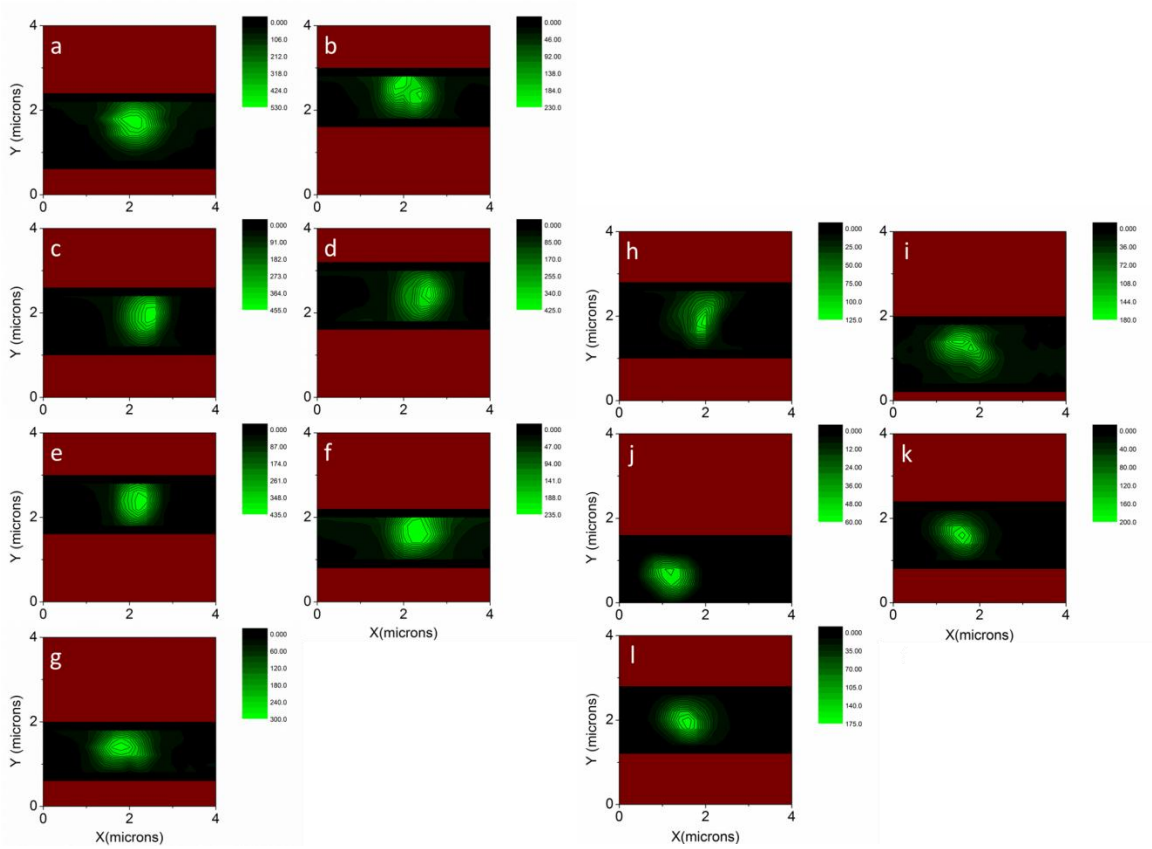

Figure 2-6. Representative PL maps of the structures shown in Figure 2-4. (a–l) correspond respectively to sample labels “A–L” in Figure 2-7c,d. Color scale represents integrated intensity in arbitrary units. Maps are cropped to the region over which the 2D Gaussian was fit.

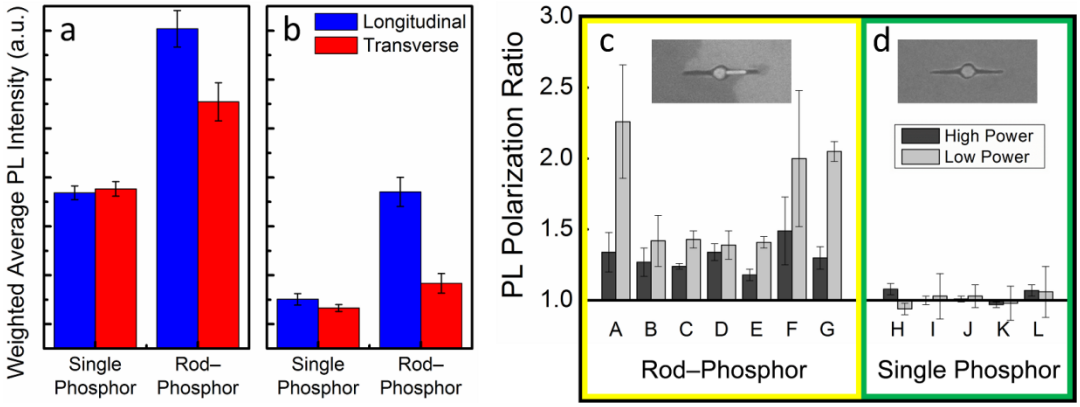

Figure 2-7. Inverse-variance weighted average PL intensity for single-phosphor and rod–phosphor structures under longitudinal and transverse laser polarization for power densities of (a)

1.6×10^6 W/cm^2 and (b) 1.6×10^5 W/cm^2. Error bars represent one standard deviation. (c,d) Ratio between PL from longitudinal excitation and transverse excitation for various (c) rod–phosphor (A–G) and (d) single-phosphor (H–L) structures (representative SEM images inset). High and low power refer to the same power densities as (a) and (b). Error bars represent one standard deviation over at least three measurements for low power and two for high power excitation.

As expected, the single phosphors without Au NRs demonstrated little sensitivity to the laser polarization. However, for rod–phosphor heterodimers the longitudinal polarization resulted in greater PL intensity than the transverse polarization. This comparison is presented more explicitly in Figure 2-7c,d, which show the ratio between PL for excitation with longitudinal laser polarization and PL for excitation with transverse polarization for each of the rod–phosphor and single-phosphor structures studied. The polarization ratio can be used as a metric for luminescence enhancement by anisotropic structures like nanorods where the enhancement along one direction is expected to be small.[119] As shown in our simulations below, there is no excitation enhancement predicted in the transverse case. From an experimental perspective, constructing this ratio is a very direct comparison, as the PL intensity was measured for each polarization in immediate succession at each point in the raster before the stage was translated to the next pixel in the map. As seen in Figure 2-7c, the PL polarization ratio was always greater than unity for the rod–phosphor cases, with magnitudes of up to ~2.3 for one of the structures. Again, the single phosphors demonstrated no polarization sensitivity, having PL polarization ratios near unity (Figure 2-7d). Consistent with the expectation that the polarization-dependent enhancement arises from excitation (rather

than emission) enhancement, when integrated separately the red and green PL bands displayed similar polarization ratios (Figure 2-8).

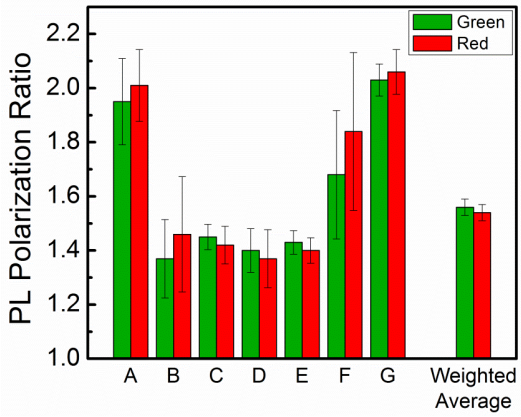

Figure 2-8. PL polarization ratio for samples A–G integrated separately over the green and red emission bands. Error bars indicate one standard deviation for multiple measurements. The inverse-variance weighted average and standard deviation among all the samples are presented at the right.

The luminescence enhancement is also observed by comparing the PL spectra under each polarization for the single phosphors and for the rod–phosphor heterodimers. As expected, there was no difference between the two polarizations in the single-phosphor case, as shown in the representative spectra of Figure 2-9a. However, Figure 2-9b illustrates that for the rod–phosphor heterodimers, in addition to an increase in intensity, the PL spectrum for the longitudinal polarization exhibits several spectral changes. Most prominently, the finer spectral structure in peak II evolves, with the ratio of the peak height at 556 nm to that at 541 nm increasing substantially. As shown in the power-dependent PL spectra for UCNP ensembles (Figure 2-10), and in agreement with the literature,[57] the relative emergence of the 556 nm peak (as well as of smaller peaks at

469 and 504 nm) is a signature of increased excitation power. To rule out the possibility that this peak arises at high power in the ensemble measurements due to local sample heating, PL spectra were collected as a function of temperature at a constant laser power. Changes in the shape of the spectra in this region were negligible up to the highest temperature measured (440 K). Therefore, it is likely that the 556 nm signature appears for the rod–phosphor structure under longitudinal polarization because of the increased local field intensity due to the plasmon resonance.

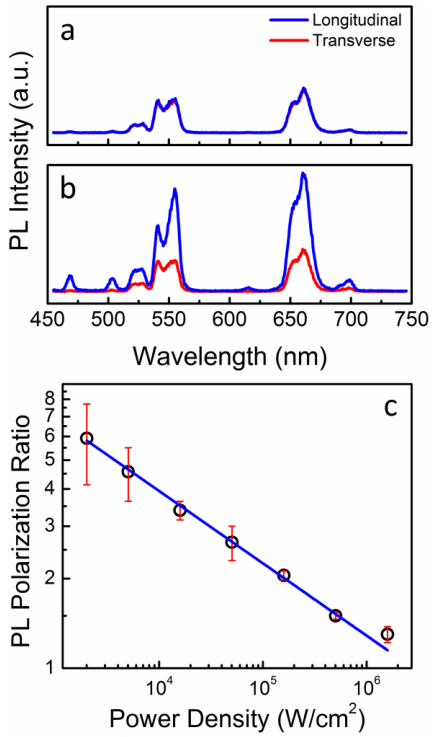

Figure 2-9. (a,b) Representative PL spectra from the center of the phosphor under longitudinal (blue) and transverse (red) incident polarization for (a) a single phosphor and (b) a rod–phosphor heterodimer. Each set of curves was normalized so that the transverse curves are of equal height for comparison. Excitation power density was 1.6×10^5 W/cm^2. (c) PL polarization ratio versus excitation power density (log scales) with fit to Eq. 2-1 (blue). Error bars are one standard deviation.

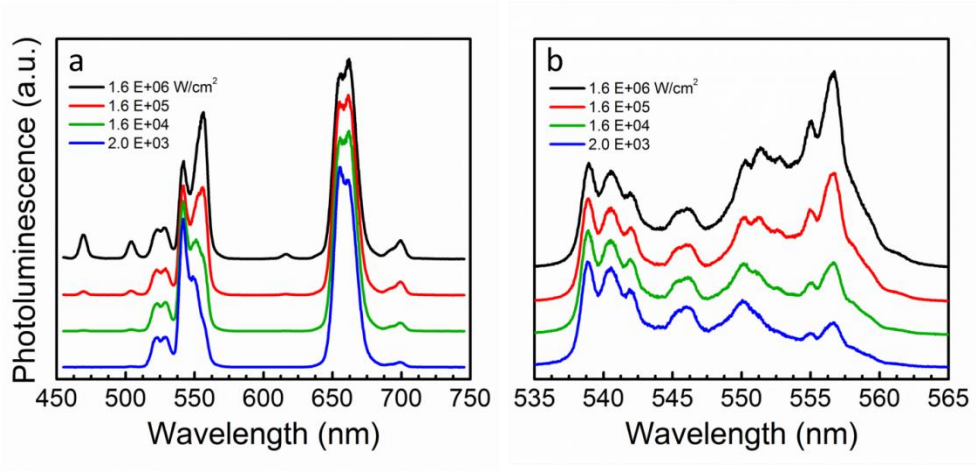

Figure 2-10. (a) Photoluminescence spectra collected from a drop-cast film of UCNPs at the indicated excitation power densities (increasing from bottom to top). Spectra were normalized to the maximum of the 660 nm peak. The peaks emerging at high power at 469 and 504 nm have been attributed to higher-excited-state transitions and that at 556 nm to excited-state-to-excited-state transitions.[57] (b) Spectra collected from the same sample at higher spectral resolution to demonstrate the relative growth of the features around 556 nm at increasing power. Spectra were normalized to the height of the left-most peak.

For all of the rod–phosphor heterodimers studied in Figure 2-7c, the polarization sensitivity was more pronounced for the low power excitation. To investigate this trend further, the PL polarization ratio for sample "G" was measured at additional excitation power levels ranging over nearly three orders of magnitude from the previous "high power" value of 1.6×10^6 W/cm^2 down to 2.0×10^3 W/cm^2. As seen in Figure 2-9c, the PL polarization ratio increased up to a value of ~6 as the incident power was decreased. The trend of increased PL polarization ratio at lower power was also consistently observed in other rod–phosphor structures, as shown in Figure 2-11. The power dependence of PL enhancement is explained by first considering the underlying power dependence of the upconversion process. Upconversion luminescence has been observed

to scale with power P as P^n.[120] While in the low-power limit n is constant and equal to two (the number of photons in the upconversion process), as power is increased the value of n can itself be power dependent.[121] This behavior can be observed in a plot of log(PL) *versus* log(P), where the slope indicates the value of n. As shown in Figure 2-12, over the range of powers used in our study this slope decreased from 1.3 to 0.4 as power was increased. To account for this behavior, we use a modified power law of the form $PL = kP^{C\cdot\log(P)+B}$, where k, C, and B are fitting parameters. With $y = \log(PL)$ and $x = \log(P)$, the shape of the log–log plot is then represented by the parabola $y = \log(k) + Bx + Cx^2$, which expresses the upconversion saturation seen at the high power levels applicable in single-particle experiments. In addition to our data, experimental and simulation results in the literature[57] could also be fit to the modified power law of this form. The PL polarization ratio can then be calculated as a function of incident laser power. Because the PL enhancement is due to an increase in the local field intensity surrounding the Au NR, we can introduce a field enhancement factor F such that $F\cdot P$ represents the increased local power experienced by the phosphor under longitudinal polarization. The longitudinal-to-transverse PL polarization ratio can then be written using the explicit form of the phosphor power dependence as

$$\frac{[F\cdot P]^{C\cdot\log(F\cdot P)+B}}{[P]^{C\cdot\log(P)+B}} \qquad \text{(Eq. 2-1)}$$

Figure 2-9c shows the very good agreement of the experimental data with this prediction. The linear relationship between log(PL polarization ratio) and log(power density) is

shown explicitly in Section 2.5. While the limited PL signal associated with single-particle measurements prevented investigating even lower power densities, it may be expected that the enhancement will continue to rise as the power law exponent approaches the low-power limit $n = 2$.

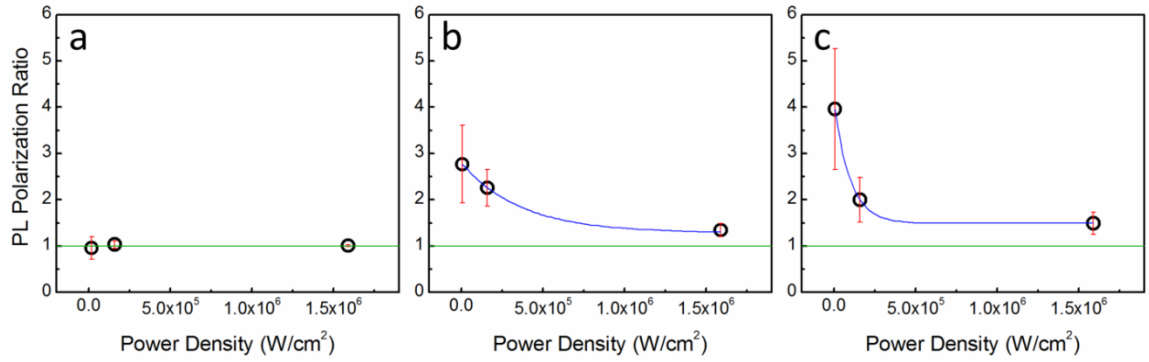

Figure 2-11. Power dependence of photoluminescence polarization ratio for (a) a single-phosphor and (b,c) two different additional rod–phosphor structures. Error bars represent one standard deviation for multiple measurements. Green line indicates a ratio of unity. Blue curves are guides to the eye.

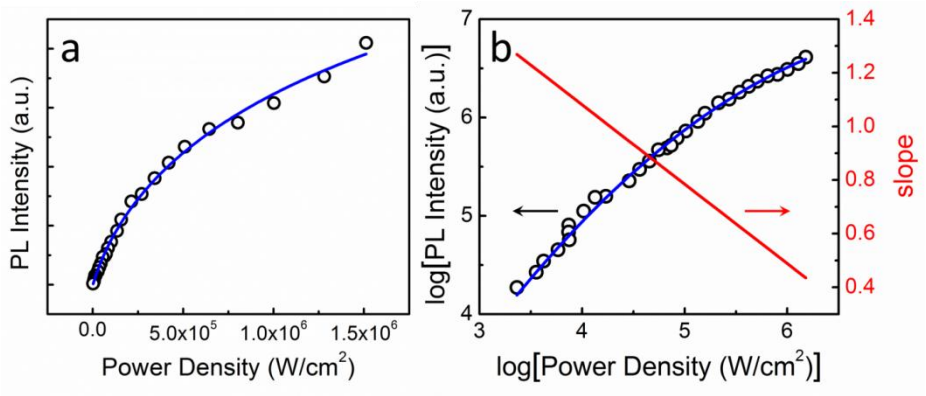

Figure 2-12. (a) Dependence on excitation power density (P) of the intensity of photoluminescence (PL) collected from a drop-cast film of UCNPs. Data is fit to the form $PL = kP^{C\cdot\log(P)+B}$, with $k = 0.018$, $B = 2.26$, and $C = -0.15$. (b) Left axis: plot of $\log(PL)$ versus $\log(P)$ superimposed with the fit from (a). Right axis: slope of this log–log curve as a function of $\log(P)$. The slope decreases from 1.3 to 0.4 as power is increased. The form of the modified power law is

intended to mathematically approximate the observed power dependent behavior over the wide range of power densities used in our study. The underlying physical phenomena are complex and require a detailed understanding of the rates of Yb^{3+} absorption, energy transfer to Er^{3+}, multi-phonon relaxation, and radiative relaxation of Er^{3+}. A recent report by Gargas *et al*.[57] calculated the populations of the Yb^{3+} and Er^{3+} energy states as a function of excitation power density to ascertain the rate-limiting steps for upconversion at different power levels. Pump photon absorption in Yb^{3+} is the bottleneck at low power densities (where the slope theoretically equals 2) that are typical of ensemble measurements. However, with increasing power into the regime suitable for single particle measurements, insufficient radiative relaxation of Er^{3+} leads to filling of higher-energy states and saturation in the visible upconversion luminescence, as observable as a reduction in the slope and as modeled by our power law.

To better understand the magnitude and sample-to-sample variation of PL enhancement in the UCNP–NR heterodimers, we performed simulations using COMSOL Multiphysics software of the polarization-dependent PL of the phosphors with and without the Au NRs and as a function of the experimentally observed variation in rod size and rod–phosphor separation. Spatial maps of the field intensity enhancement under 977 nm excitation, defined as the ratio of the electric field intensity with and without the nanorod, were generated for each incident polarization, as shown in Figure 2-13a,b. It is clear that the longitudinal polarization results in amplified field intensity near the rod tip where the phosphor is located, in contrast to the absence of enhancement for transverse polarization. Due to the spatial distribution of the field intensity, different regions of the phosphor volume experience different amounts of enhancement under longitudinal excitation. To explore this variation, the field intensity enhancement was evaluated at six representative points (locations shown in Figure 2-14). For each of the six points, the field intensity enhancement decreases with increasing rod–phosphor separation distance *d*

(Figure 2-15), and as expected from the shape of the field distribution, points nearest the rod tip are most strongly impacted while those further away feel more limited effects.

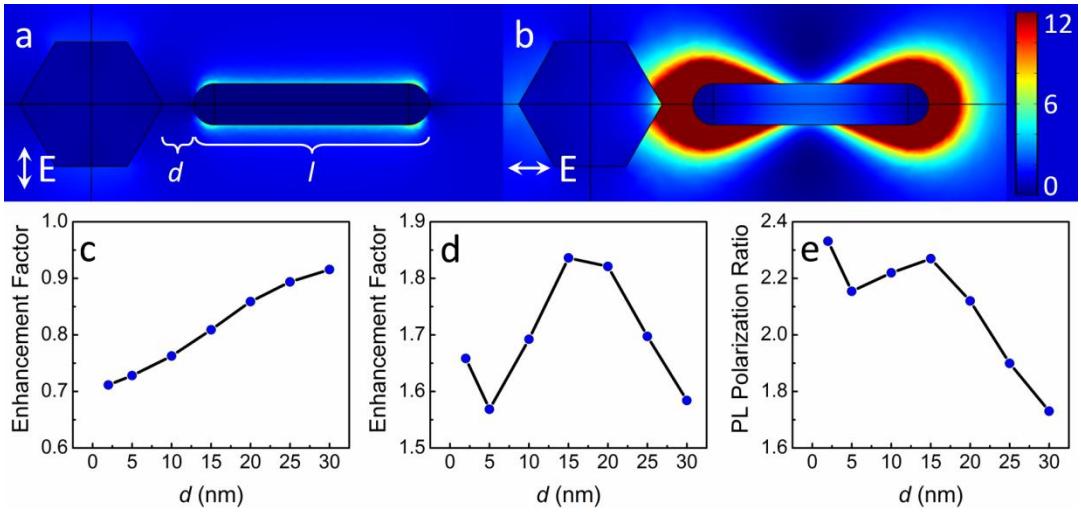

Figure 2-13. Simulated field intensity enhancement maps for (a) transverse and (b) longitudinal excitation polarization. (c,d) Simulated PL enhancement factor as a function of rod–phosphor separation *d* for (c) transverse and (d) longitudinal polarization. (e) Simulated PL polarization ratio as a function of rod–phosphor separation *d*.

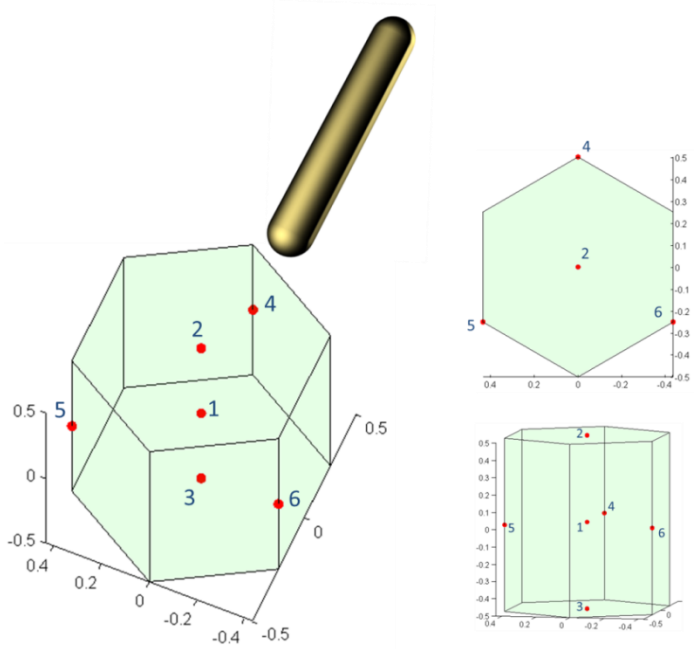

Figure 2-14. Location of point sources within the phosphor volume used for the simulations. Note that point 4 is located closest to the rod tip.

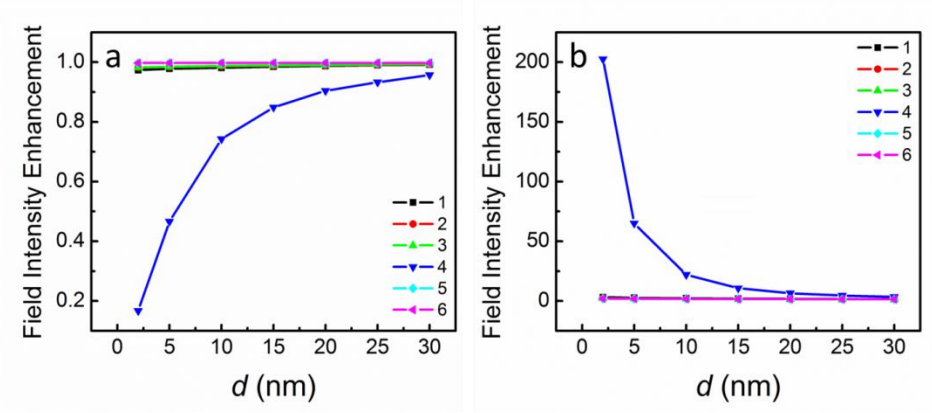

Figure 2-15. Simulated field intensity enhancement as a function of rod–phosphor separation *d* evaluated at the six points indicated in Figure 2-14 for (a) transverse and (b) longitudinal polarization.

In addition to the field enhancement, quenching due to losses in the nanorod must also be taken into consideration. This is done by calculating the emission efficiency for a

point dipole in the presence of the rod, defined as the radiated power divided by the total emitted power (radiated power plus power lost into the rod). Emission efficiency averaged over three orthogonal dipole orientations at each of the six points as a function of rod–phosphor separation is shown in Figure 2-16, where increased quenching is observed as the separation distance is reduced. The overall PL enhancement factor is the product of the field intensity enhancement and the emission efficiency, and it is shown for each polarization in Figure 2-13c,d averaged over the six emitter source positions. While the PL is enhanced by up to a factor of 1.8 in the longitudinal case, only quenching is predicted for transverse polarization. To explain why a small amount of enhancement was observed experimentally for transverse polarization, we consider misorientation of the excitation laser polarization with respect to the rod axes. As shown in Figure 2-17a, rotating the transverse polarization slightly off axis changes the spatial distribution of field enhancement such that some portions of the phosphor experience amplified field intensity. As a result, the average field enhancement factor for transverse polarization can change from being less than one to greater than one with increasing misorientation angle (Figure 2-17b).

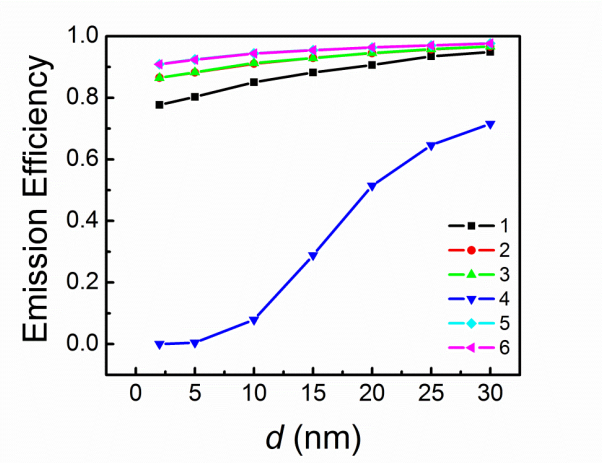

Figure 2-16. Simulated emission efficiency as a function of rod–phosphor separation *d* evaluated at the six points indicated in Figure 2-14.

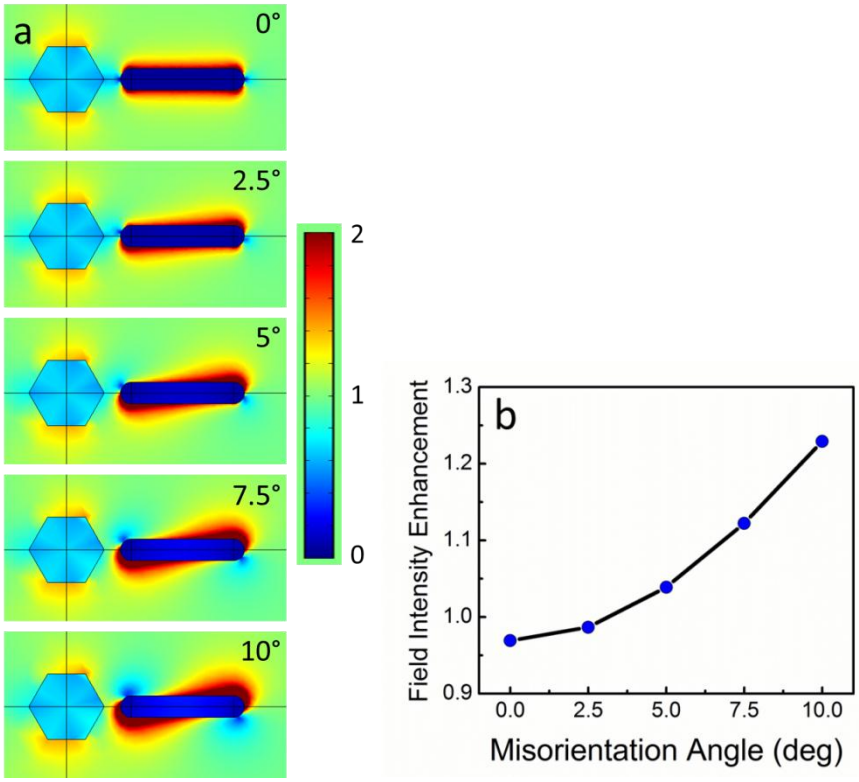

Figure 2-17. (a) Simulated field intensity enhancement maps for transverse polarization at the indicated polarization misorientation angles. (b) Simulated field intensity enhancement averaged over the six representative points of Figure 2-14 as a function of misorientation angle.

For longitudinal polarization (Figure 2-13d), the PL enhancement increases with decreasing rod–phosphor separation until reaching a maximum at d = 15 nm. Enhancement diminishes at smaller separation because of the reduction in emission efficiency due to loss in the rod. For comparison with the experimental results the PL polarization ratio was also calculated (Figure 2-13e), and it displays a local maximum value of 2.3 at d = 15 nm. The simulated magnitudes of PL polarization ratio agree favorably with the experimental results and show that variations in the gap size from the average experimentally measured gap of 14 nm are consistent with the observed sample-to-sample differences in enhancement. The diminishing enhancement with increasing gap size is experimentally supported by PL measurement of a heterodimer with a very large gap size of 80 nm (pictured in Figure 2-18). The PL polarization ratio in this case was measured to be 1.05 ±0.4, which is significantly closer to unity than for any of the small-gap heterodimers we reported and is comparable to the ratios measured for single phosphors having no rod nearby.

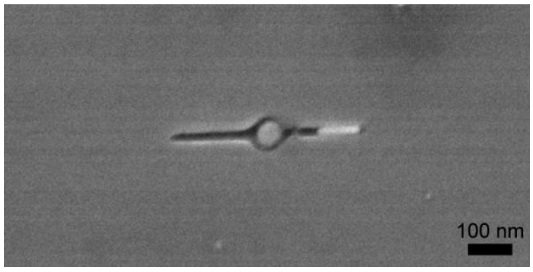

Figure 2-18. SEM image of a rod–phosphor structure with a large gap of ~80 nm.

Another cause of differences in enhancement among samples is polydispersity in nanorod size, which leads to variation in the spectral position of the surface plasmon

resonance. To investigate this effect, the PL enhancement was simulated as a function of rod length, with the rod–phosphor gap fixed at the maximum enhancement distance of 15 nm and the rod diameter constant at 20 nm. As seen in Figure 2-19, the PL enhancement reaches a maximum when the rod length is tuned so that the SPR matches the frequency of the 977 nm excitation. While the simulation predicts this condition to occur for a rod length of 160 nm, placing the rod in a dielectric environment (representing the SiO_2 template) rather than in free space would shift the resonance condition to a shorter rod length more closely matching the experimental length of 109 nm. Finally, we note that the condition of matching the rod resonance with the phosphor absorption can be achieved in rods of different overall sizes by simultaneously tuning the rod length and diameter. Figure 2-20 shows that for a fixed longitudinal SPR wavelength, greater enhancement can be achieved with larger-volume rods due to the greater extent of their electric field enhancement.

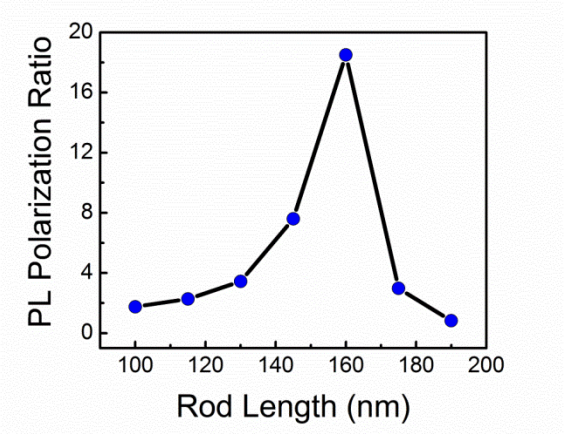

Figure 2-19. Simulated PL polarization ratio as a function of rod length. Rod diameter is fixed at 20 nm, and rod–phosphor separation is 15 nm.

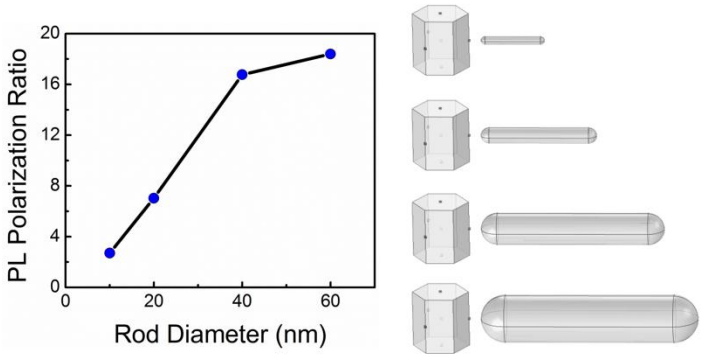

Figure 2-20. Simulated PL polarization ratio as a function of the overall rod size as pictured in the illustrations and described in Table 2-1. For the chosen rod diameters, the rod length was selected according to Bryant *et al.*[122] to maintain the longitudinal SPR wavelength at 977 nm in order to match the phosphor absorption. Rod–phosphor separation was 15 nm.

Table 2-1. Nanorod dimensions used for the simulations shown in Figure 2-20.

Rod Diameter (nm)	Rod Length (nm)	Aspect Ratio
10	79	7.9
20	144	7.2
40	228	5.7
60	270	4.5

2.3 Conclusions

In summary, we have utilized template-assisted self-assembly to form nanocrystal heterodimers consisting of a single UCNP and a single Au NR and have characterized their plasmon-enhanced upconversion luminescence. Shape-selective topographical templates defined by electron-beam lithography were used to direct the co-assembly of $NaYF_4$:Yb^{3+},Er^{3+} nanophosphors along with Au NRs having longitudinal SPRs tuned to

match the phosphor excitation wavelength. Polarization- and power-dependent PL of individual UCNPs in the presence and absence of Au NRs was measured and simulated, and several-fold PL enhancement due to the localized electric field intensity surrounding the Au NRs was observed. The successful co-assembly scheme demonstrated herein motivates extension to other material systems for achieving placement of a wide range of nanocrystal components into a variety of predesigned functional arrangements.

2.4 Methods

2.4.1 Nanocrystal Synthesis

The $NaYF_4$:Yb^{3+},Er^{3+} (20%, 2%) upconversion nanophosphors[54] and the gold nanorods[123] were synthesized according to previously reported methods.

2.4.2 Template Fabrication and Nanocrystal Assembly

The substrate consisted of a silicon wafer with 100 nm thermal oxide (Silicon Quest International). Poly(methyl methacrylate) (PMMA) positive e-beam resist (MicroChem) was spun onto the substrate in two layers: (1) 495K molecular weight (MW) PMMA in anisole was spun at 3000 rpm for 45 sec followed by a 4 min bake at 180°C and then (2) 950K MW PMMA in anisole was spun at 5000 rpm for 5 sec followed by a 4 min bake at 180°C. The thickness of the PMMA layer was ~150–200 nm as measured by atomic force microscopy (Asylum Research MFP-3D). The template pattern was written by e-beam lithography (Elionix ELS-7500EX) using a 50 kV accelerating voltage and a 50 pA beam current. The resist was developed by a 90 second

immersion in a solution of methyl isobutyl ketone (MIBK) and isopropyl alcohol (IPA) at a 1:3 ratio and was rinsed with IPA. The e-beam pattern was transferred by etching into the silica layer using reactive ion etching (RIE, Oxford Instruments Plasmalab 80 Plus) to a depth of ~40 nm (as measured by AFM) to construct the templates. UCNPs were assembled into the template features using a "squeegee method" in which a drop of a solution of UCNPs in hexanes was dragged across the surface by a piece of PDMS cut with a razor blade from a cast sheet. The PDMS wiper was held at an angle to the substrate of ~35° and was withdrawn at ~0.8 mm/s. The PMMA layer was then removed by sonication in acetone for 30 seconds. A 6-nm layer of SiO_2 was deposited in a Cambridge Nanotech Savannah 200 ALD system using 3-aminopropyltriethoxysilane (APTES), O_3, and H_2O precursors. Au NRs were assembled using the apparatus described above, using a substrate withdrawal rate of 7 μm/s.

2.4.3 Structural and Optical Measurements

Scanning electron microscopy was performed using a JEOL 7500F HRSEM and an FEI Quanta 600 ESEM operating at 5 kV. Transmission electron microscopy was performed with a JEOL JEM-1400 TEM operating at 120 kV. Solution-phase extinction spectra of UCNPs and Au NRs were collected using a Cary 5000 UV/Vis/NIR spectrometer. Spatially resolved PL measurements were taken under 977 nm illumination from a Ti:Sapphire laser (Coherent, Inc. Mira HP pumped with a 532 nm 18 W Verdi diode laser). Laser power was monitored by a beam sampler and power meter (Newport 1936-C) and stabilized throughout each measurement by passing the beam through a

gradient neutral density filter mounted in a motorized rotation stage (Thorlabs PRM1Z8) controlled in LabVIEW. The laser beam was coupled into a modified Olympus BX2 microscope with a shortpass dichroic mirror (Thorlabs DMSP805R) and focused by a 0.8 numerical aperture objective to a diffraction-limited (~1.5 μm diameter) spot. Samples were translated under the excitation spot with a closed-loop piezo-controlled stage (Thorlabs Nanomax) using a 200 nm step size. Upconversion luminescence was collected by a fiber and routed to a Horiba iHR 550 spectrometer with a nitrogen-cooled Symphony Si CCD camera. A shortpass filter (Newport 10SWF-950-B) at the spectrometer entrance removed any residual excitation laser signal. PL spectra were filtered using a MATLAB script to remove false signals due to cosmic ray strikes on the detector. Temperature-dependent PL spectra were collected by mounting the sample on the heating stage of an MMR Technologies D2300 Optical Transmission System.

2.4.4 Simulations

The theoretical simulations were performed using the commercial software COMSOL Multiphysics with a frequency domain solver based on the finite difference method. Only linear effects were taken into account in the simulations; therefore, the pump and the emission processes have been considered as separate phenomena and then combined together. The pump effect was simulated using plane waves with two different polarizations (parallel and orthogonal to the nanorod long axis). The emission process was studied using 6 point sources uniformly located within the phosphor, with each source modeled as three short electric dipoles oriented along x, y, and z with equal

emission probabilities. The dispersion of the gold at the pump wavelength, as well as at the two emission wavelengths, has been taken from Palik,[124] whereas the permittivity for the phosphor was set based on Banski *et al*.[125] The simulations shown in the Figures are for an emission wavelength of 540 nm; simulations performed at 650 nm displayed similar results.

2.5 Supplemental Discussion

The following presents a derivation from Eq. 2-1of the linear relationship of log(PL polarization ratio) *versus* log(power density) as depicted in Figure 2-9. Let R = PL polarization ratio. Then Eq. 2-2 below restates Eq. 2-1 and can be transformed as follows:

$$R = \frac{[F \cdot P]^{C \cdot \log(F \cdot P) + B}}{[P]^{C \cdot \log(P) + B}} \quad \text{(Eq. 2-2)}$$

$$\log(R) = \log\left([F \cdot P]^{C \cdot \log(F \cdot P) + B}\right) - \log\left([P]^{C \cdot \log(P) + B}\right) \quad \text{(Eq. 2-3)}$$

$$\log(R) = (C \cdot \log(F \cdot P) + B) \cdot \log(F \cdot P) - (C \cdot \log(P) + B) \cdot \log(P) \quad \text{(Eq. 2-4)}$$

$$\log(R) = (C \cdot [\log(F) + \log(P)] + B) \cdot [\log(F) + \log(P)] - (C \cdot \log(P) + B) \cdot \log(P) \quad \text{(Eq. 2-5)}$$

$$\log(R) = (C \cdot \log(F) + C \cdot \log(P) + B) \cdot [\log(F) + \log(P)] - C \cdot \log(P) \log(P) - B \cdot \log(P) \quad \text{(Eq. 2-6)}$$

$$\log(R) = C \cdot \log(F) \log(F) + C \cdot \log(F) \log(P) + C \cdot \log(P) \log(F) + C \cdot \log(P) \log(P) + B \cdot \log(F) + B \cdot \log(P) - C \cdot \log(P) \log(P) - B \cdot \log(P) \quad \text{(Eq. 2-7)}$$

$$\log(R) = \log(F)\,[2C \cdot \log(P) + C \cdot \log(F) + B] \quad \text{(Eq. 2-8)}$$

$$\underbrace{\log(R)}_{y} = \underbrace{2C \cdot \log(F)}_{m}\underbrace{\log(P)}_{x} + \underbrace{\log(F)\,[C \cdot \log(F) + B]}_{b}$$

(Eq. 2-9)

From Eq. 2-9, it is clear that a plot of log(PL polarization ratio) *versus* log(power density) will be linear when Eq. 2-1 holds.

CHAPTER 3. PLASMON RESONANCES IN SELF-ASSEMBLED TWO-DIMENSIONAL AU NANOCRYSTAL METAMOLECULES[2]

3.1 Introduction

Just as polycyclic aromatic hydrocarbons, the larger-size homologues of benzene, represent the building blocks of graphene,[126–129] plasmonic nanocrystal (NC) oligomers function as fundamental structural units for extended two-dimensional (2D) optical metamaterial assemblies. The interaction among individual plasmonic NCs bears many similarities to delocalization in π-conjugated organic systems,[130–133] resulting in NC "metamolecules" that possess unique properties tailorable by the number and arrangement of the constituent components. The extensive applications of metamaterials in areas such as electromagnetic cloaking, subwavelength imaging, and optical information processing[44,134–137] motivate the desire for an improved fundamental understanding of how to engineer the optical response of plasmonic systems.

Single metal NCs support plasmon resonances that depend on NC size,[35] shape,[36] and composition.[34] When two NCs are brought together, new collective resonances are engendered by the coupling of the particles in a manner well described by a plasmon hybridization model akin to molecular orbital theory.[39] As additional NCs are added,

---

[2] Much of this chapter appears in print: Adapted with permission from Greybush, N. J.; Liberal, I.; Malassis, L.; Kikkawa, J. M.; Engheta, N.; Murray, C. B.; Kagan, C. R. *ACS Nano* **2017**, *11*, 2917–2927. DOI: 10.1021/acsnano.6b08189 © 2017 American Chemical Society.

more complicated features can arise, including higher-order modes, magnetic dipole modes,[41] and Fano resonances.[40,138,139] Expression of these modes is sensitive to the precise geometrical arrangement of the individual plasmonic units.[138,140–142] As assemblies become very large, in the limit forming an infinite 2D sheet, they continue to display well-defined plasmonic properties determined by the constituent NCs and their interparticle spacing.[143–145] The collective response of a finite array of plasmonic NCs can be determined from the contributions of each pairwise interaction between particles. However, since the coupling strength decreases exponentially with interparticle separation,[146] the interaction between more distant particles in an array has limited influence. Therefore, the evolution of the characteristic optical response is expected to saturate as the number of particles increases.[147–149] While the endpoints of this evolution—namely, few-particle clusters and large-area arrays—are fairly well studied, the transition regime of intermediate-sized plasmonic oligomers is far less explored. Understanding the length scale of the coupling between the constituent particles and the types of plasmonic modes supported by metamolecule oligomers is critical for ultimately designing and realizing functional NC metamaterials.

A major obstacle in studying plasmonic oligomers is the challenge of producing them experimentally. As the quantity of individual components increases, the difficulty of achieving precision in their number and geometrical arrangement grows. While lithography and physical deposition of metal can be used to directly fabricate plasmonic oligomers,[150–154] tool resolution imposes a lower limit on the size of individual units and

especially on their interparticle spacing (typically to ~10 nm), which motivates the use of techniques for bottom-up assembly of chemically synthesized NCs. Fabrication by chemical methods also reduces the optical losses associated with the polycrystallinity of evaporated metal.[155,156] Once synthesized, individual NCs can be placed in a desired configuration by direct manipulation,[142,157,158] but this is time-consuming when more than one oligomer is desired. Conversely, a large number of NC clusters can be formed simultaneously by techniques relying purely on self-assembly.[139,159] However, in this case there is limited freedom in determining the types of arrangements that are formed. This issue can be addressed to some degree by tailoring the interparticle interactions, such as through DNA-mediated assembly.[160–162]

An alternative approach is to combine the advantages of lithographic control with the desirable properties of NC components by utilizing template-assisted self-assembly.[8,12,15,19,30,113,163,164] Using this method, NCs can be directed to assemble within topographical templates defined using electron-beam lithography. Previous studies have reported the assembly of both single-component[28,30,113,165] and multi-component[20] structures from plasmonic NCs. Here, we demonstrate the use of polygonal templates to direct the assembly of hexagonally packed Au NC oligomers having predefined geometries with "digital," single-NC precision. In particular, a sequence of oligomer metamolecules with increasing number of NCs is chosen to outline the evolution in optical response as the assembly grows from that of a single NC toward that of an extended 2D array. Darkfield scattering spectroscopy of individual oligomers in

combination with theoretical simulations is used to map the wavelength and nature of plasmonic modes as a function of metamolecule size and degree of disorder in NC packing.

3.2 Results and Discussion

The target configurations are depicted in Figure 3-1a. Beginning with a single spherical Au NC, each generation represents the addition of a shell of NCs equidistant from the central NC. In this fashion, hexagonally-packed oligomer metamolecules with 1, 7, 13, 19, and 31 NCs are formulated. Figure 3-1b presents a representative scanning electron microscopy (SEM) image from each generation of metamolecule. To achieve these arrangements experimentally, templates are defined in poly(methyl methacrylate) (PMMA) using electron-beam lithography on a germanium wafer coated with 250 nm of SiO_2. A germanium substrate is chosen instead of silicon to avoid scattering artifacts in the near-infrared (NIR) that can arise with silicon due to its NIR transparency. While previous works have mainly utilized circular or linear templates,[28,29,111,113,166] here the template shape is designed to match the outline of the target metamolecule, as portrayed in Figure 3-1a. Circular templates are effective for forming close-packed oligomers when the number of components is small (*e.g.* 7 spheres), but larger numbers of spheres can often pack within circles more efficiently in configurations that lack the desired hexagonal symmetry.[167] Thus, to impose hexagonal close-packing, polygonal templates are used for forming the oligomers in this study. An SEM image of empty templates

defined to target 31-member oligomers is shown in Figure 3-2 to demonstrate that polygonal template outlines are achieved as desired.

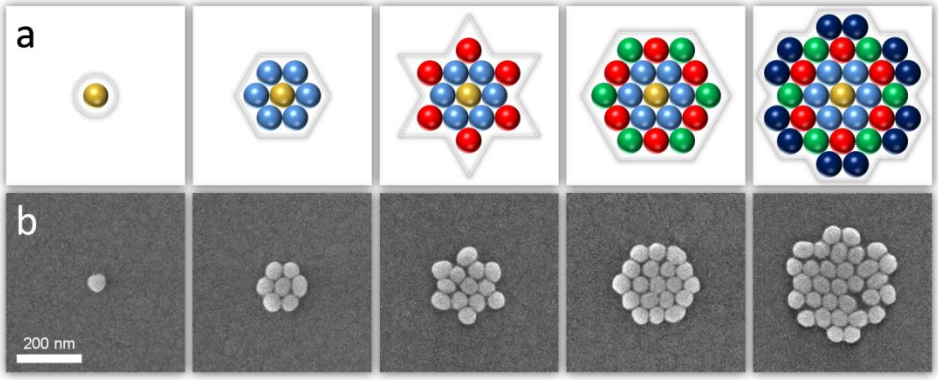

Figure 3-1. (a) Schematic of plasmonic oligomer metamolecules assembled in polygonal templates. The assemblies contain 1, 7, 13, 19, and 31 NCs. Like colors indicate NCs equidistant from the central NC, forming (light blue) first-, (red) second-, (green) third-, and (dark blue) fourth-nearest neighbor 2D shells. (b) Scanning electron micrographs of Au NC oligomers formed *via* template-assisted self-assembly, shown after resist liftoff.

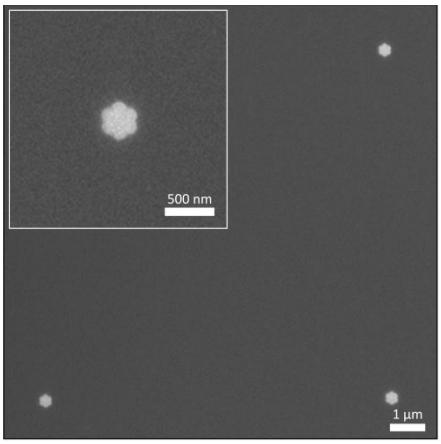

Figure 3-2. Representative scanning electron microscopy (SEM) image of empty templates defined in poly(methyl methacrylate) (PMMA) resist. The templates shown here have dimensions designed to assemble 31-membered oligomers. Inset: higher-magnification image of the top-right template.

Au NCs are assembled into the templates *via* capillary forces. The NCs have an average diameter of 55 ± 3 nm and are stabilized by cetyltrimethylammonium bromide (CTAB). A transmission electron microscopy (TEM) image of the NCs is provided in Figure 3-3. An aqueous dispersion of NCs is dispensed between the templated substrate and a fixed glass slide as shown schematically in Figure 3-4a. As the substrate is translated by a motorized stage relative to the fixed slide, the liquid meniscus passes over the templated features, and capillary forces direct the NCs into the templates. To avoid light scattering by the patterned PMMA templates and to eliminate stray NCs from the regions surrounding the assembled oligomers, the resist layer is subsequently removed by liftoff in acetone (Figure 3-4b). Following liftoff, the oligomers that have formed in the templated areas remain on the surface of the wafer, as shown in Figure 3-5. Several representative examples from each metamolecule configuration are selected for further study in order to build a statistical understanding of the typical optical response. SEM images of the oligomers are shown in Figure 3-6. It is evident that the prescribed template shapes are successful in dictating oligomer size and NC arrangement to achieve the target structures. A description of the oligomer formation yields is presented in Figure 3-7.

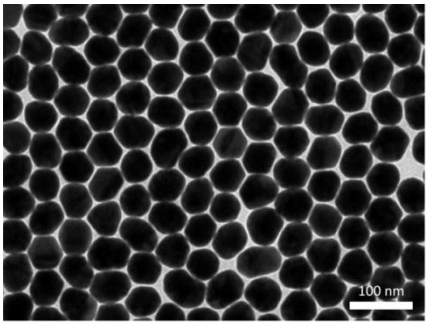

Figure 3-3. Transmission electron microscopy (TEM) image of the Au nanocrystals used for assembly. Average nanocrystal diameter is 55 ± 3 nm.

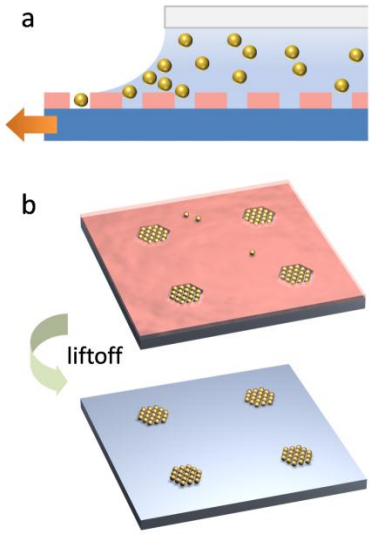

Figure 3-4. (a) Cross-sectional schematic of the template-assisted self-assembly process. As the substrate is translated relative to a fixed glass slide, capillary forces at the liquid meniscus direct the NCs to assemble within the templates defined in the resist. (b) Liftoff in acetone removes the resist layer and any stray NCs, leaving behind well-defined Au NC oligomers.

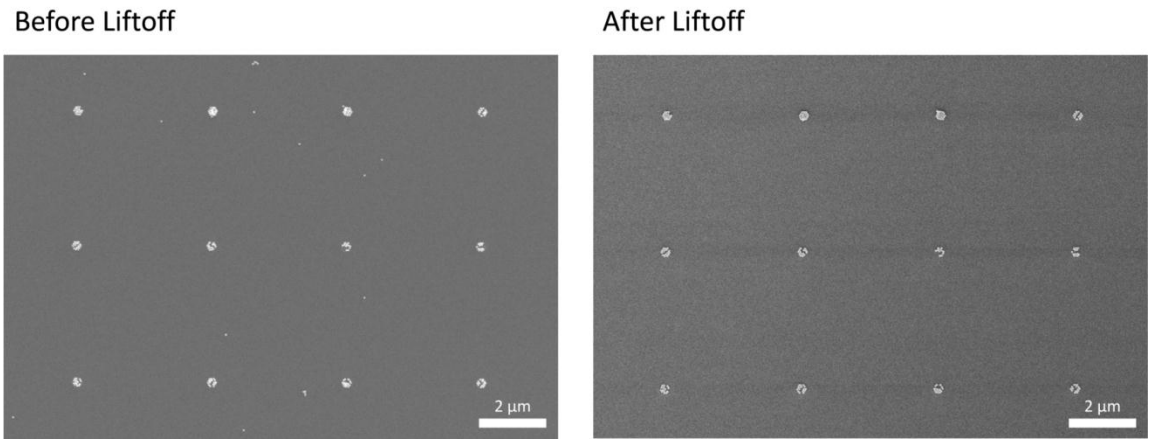

Figure 3-5. SEM images of an array of oligomers before and after liftoff. The position and integrity of the oligomers are preserved after liftoff, while the number of stray nanocrystals is reduced.

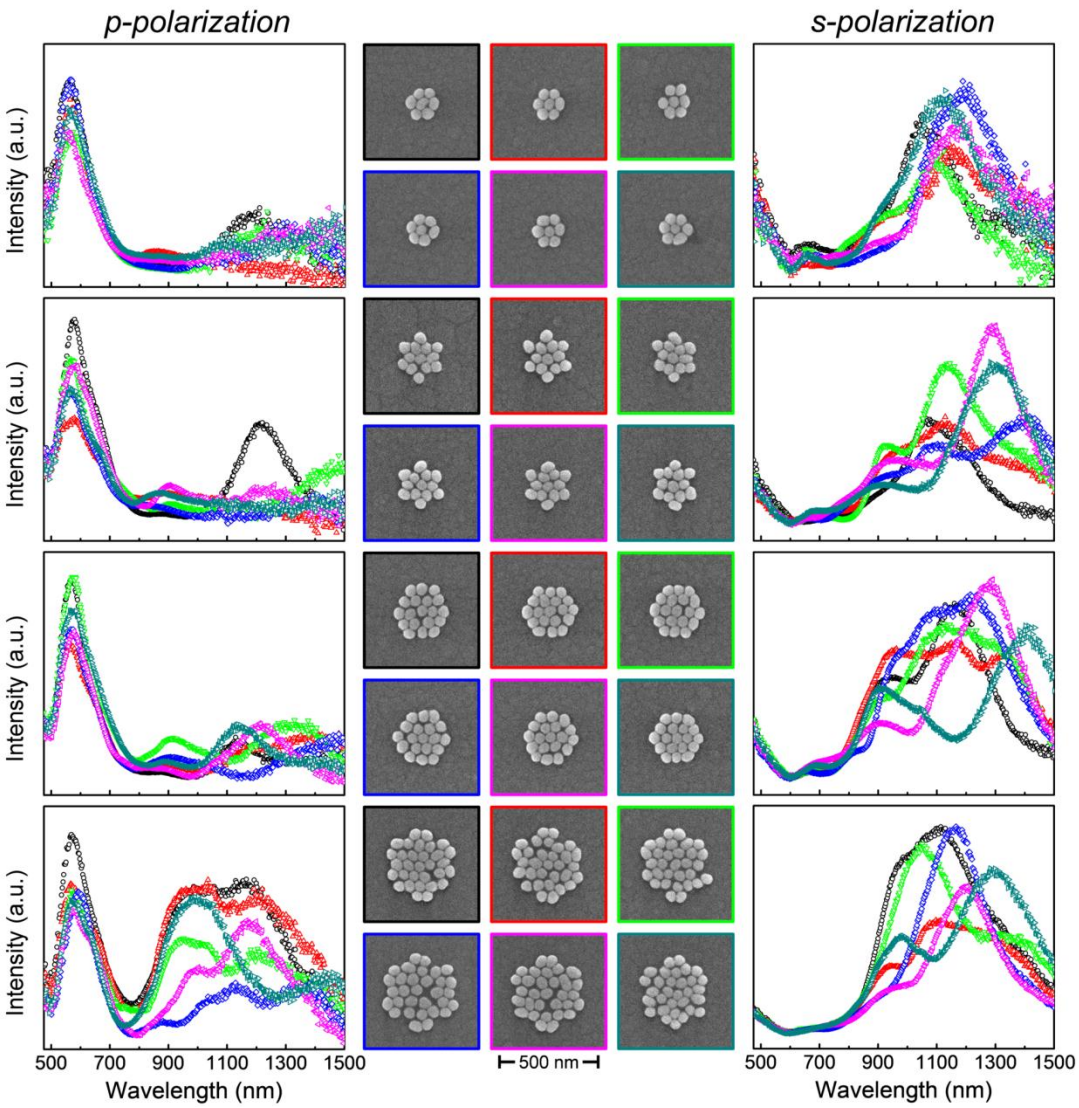

Figure 3-6. Scanning electron micrographs and single-oligomer darkfield scattering spectra of representative 7-, 13-, 19-, and 31-member Au-NC oligomers. Spectra for each different metamolecule configuration collected under p- and s-polarized excitation are presented separately in the left and right panels, respectively, with the color indicating the corresponding SEM image.

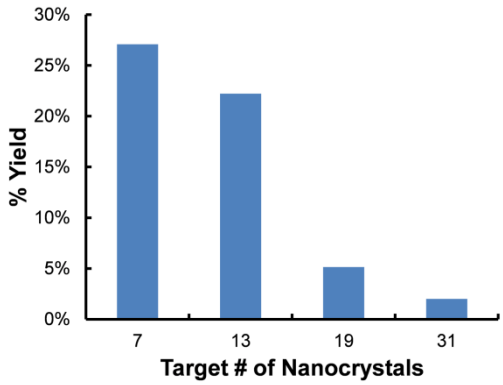

Figure 3-7. Estimated percent assembly yield for each metamolecule configuration. The average over all the configurations is 14%. A total of 704 template sites is surveyed. A success is scored only if the oligomer possesses exactly the target number of nanocrystals. The yield of templates having a nonzero number of nanocrystals is greater than 90%.

The plasmonic modes supported by each oligomer are probed using spatially-resolved, polarized darkfield scattering spectroscopy. The measurement setup is depicted schematically in Figure 3-8. Polarized broad-band light is focused obliquely on the sample, while the collection objective gathers light scattered within a cone oriented normal to the sample surface. The scattered light is routed by an optical fiber to a spectrometer for detection, with the 100 μm core of the fiber serving as an aperture to spatially restrict the corresponding collection area on the sample surface to a region approximately 2 μm in diameter. Individual template sites are spaced on a pitch of 10 μm so that the scattering spectrum from an individual oligomer can be collected independent of influence from neighboring oligomers. Conditions of p- and s-polarized excitation are established by orienting the polarizer axis vertically or horizontally, respectively. For an incident elevation angle of 10 degrees above horizontal, p-polarization establishes an electric field vector orientation predominantly perpendicular to the sample plane, while s-

polarization orients the electric field vector parallel to the sample plane. By separately considering p- and s-polarized excitation, out-of-plane and in-plane plasmonic responses are discerned.

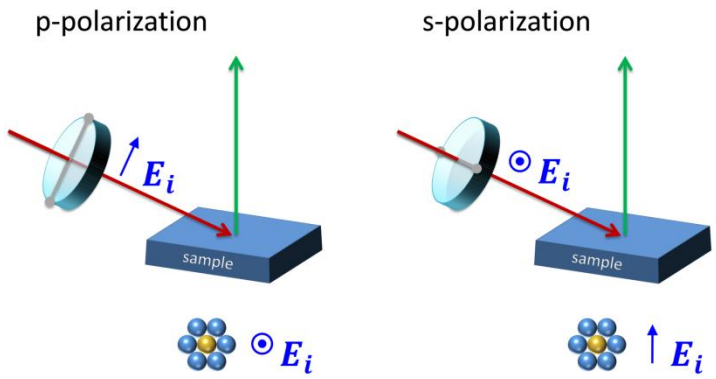

Figure 3-8. Schematic depiction of experimental setup, illustrating p- and s-polarization defined by rotating a linear polarizer in the excitation beam. The electric field for p-polarization is primarily out of the plane of the oligomers (with a small in-plane component) while the electric field for s-polarization is completely in plane. The upper row shows a perspective view of the setup, and the lower row illustrates a top view of the sample.

Scattering spectra from each of the individual oligomers studied are shown in Figure 3-6 for p- and s-polarization. For p-polarized excitation, the spectra from all metamolecule configurations display a prominent scattering peak centered between 540 and 590 nm. This feature arises from a localized surface plasmon resonance wherein the electric fields are oriented primarily perpendicular to the plane of the oligomer.[168,169] Since all of the metamolecule configurations consist of a single layer of NCs, the characteristic length scale for this resonance approximately corresponds to one NC diameter in all cases, leading to only a limited modification of the resonance wavelength as the number of NCs in the lateral direction increases. However, the addition of NCs

plus the intervening CTAB increases the dielectric constant of the local environment of each NC in the oligomer, consistent with a red shift in the out-of-plane resonance wavelength of the plasmonic structure with increasing oligomer size. This modest red shift is further illustrated by comparing the average p-polarization spectrum for each metamolecule configuration (Figure 3-9a). To quantify the spectral shift, each of the individual constituent scattering spectra is fit by a Lorentzian lineshape in energy units over the corresponding wavelength range of 500–750 nm. A representative fit for each metamolecule configuration is provided in Figure 3-10. Figure 3-9b presents the average center wavelength from the fitting as a function of oligomer size. The evolution of the resonance wavelength saturates as the number of NCs becomes sufficiently large that additional NCs do not strongly influence the average dielectric environment within the oligomer. The spectral evolution under p-polarization is interpreted through the development of an effective dielectric medium rather than plasmon hybridization because limited inter-NC coupling is expected for light polarized out-of-plane.[170] Under this polarization, the local electric fields are amplified in surrounding regions along the vertical direction, but the field intensity in the junctions between NCs is comparatively weak.

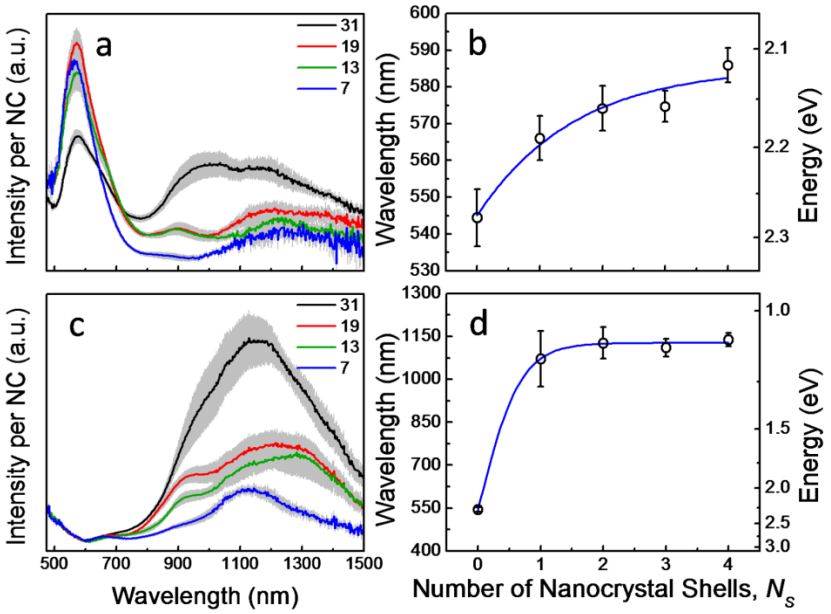

Figure 3-9. (a) Average darkfield scattering spectra for each metamolecule configuration under p-polarized excitation, normalized by the number of NCs in the oligomer. (b) Resonance center positions determined from Lorentzian fits over the 500–750 nm range of each of the spectra averaged in (a) as a function of the number of NC shells (N_S) surrounding the center NC. (c) Average darkfield scattering spectra for each metamolecule configuration under s-polarized excitation, normalized by the number of NCs in the oligomer. (d) Spectral centroid positions determined from each of the spectra averaged in (c) as a function of the number of NC shells. Shaded regions in (a,c) represent the standard error of the mean. Fitting curves in (b,d) are according to Eq. 3-1, and error bars represent one standard deviation.

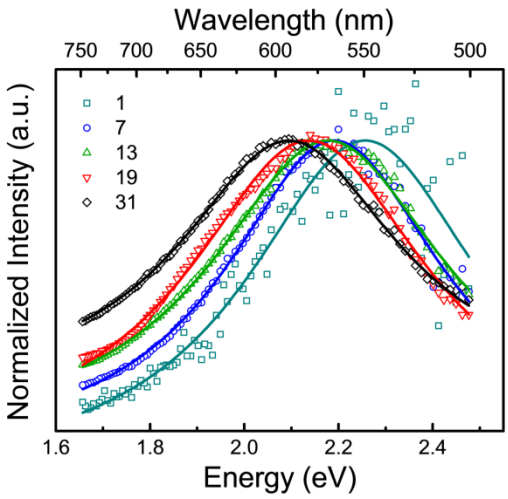

Figure 3-10. A representative scattering spectrum and corresponding Lorentzian fit curve for each metamolecule configuration under p-polarization. The number of nanocrystals in the oligomer is indicated in the legend. Intensity is normalized by the maximum value of each fit curve.

For s-polarization, where the incident electric field lies completely within the plane of the oligomers, the scattering is dominated by spectral features that are profoundly red-shifted with respect to the single-particle resonance, appearing in the 900–1500 nm range (Figure 3-6, right panel). The in-plane electric fields enable plasmonic modes representing cooperative interactions across multiple NCs to be supported.[168,169] Because of their larger spatial extent and the hybridization of several individual modes, these resonances appear at longer wavelengths than those associated with a single NC or with the out-of-plane modes observed under p-polarization. As discussed below, the overall oligomer response may include contributions from both electric dipole and magnetic dipole modes, leading to the complex features exhibited by many of the oligomers. Scattering features within the 900–1500 nm range are also present to varying degrees under p-polarization due to the small in-plane component of the

incident electric field. We note that, while appearing in a similar spectral window, the specific features from in-plane modes for a given single oligomer under p-polarization are not necessarily expected to match the features from in-plane modes under s-polarization. This is because the in-plane electric fields in the two polarization conditions are orthogonal to each other and the oligomers lack perfect rotational symmetry due to variations in the NC arrangement. We also cannot exclude the possibility that the oligomers may not be fully planar, which could introduce additional near-infrared modes under p-polarization.

To further evaluate the typical response under s-polarization as a function of oligomer size, the average spectrum for each metamolecule configuration is shown in Figure 3-9c, normalized by the number of NCs in the oligomer. We observe an increase in the scattering intensity per NC as the oligomers become larger, similar to a previous report on the longitudinal modes of NC chains[171] and consistent with the excitation of superradiant modes in which the dipoles of the NCs are coaligned.[165] We note that the in-plane component for p-polarization (Figure 3-9a, 900–1500 nm) follows the same trend. Since the spectral lineshape for s-polarization is not well represented by a simple function, the centroid of each constituent spectrum is calculated for the purpose of comparison. Figure 3-9d presents the average scattering centroid wavelength as a function of oligomer size. Note that for the single NC, the signal-to-noise ratio under s-polarization is too low to reliably extract a centroid wavelength so the Lorentzian fit from p-polarization (see Figure 3-10) is used instead since the single particle resonance should

not be significantly affected by incident polarization. The data of Figure 3-9d indicate that the resonance position substantially red-shifts with increasing oligomer size before approaching a constant value for the oligomers having more than two shells of NCs around the center NC (*i.e.* 13-member oligomers).

Our observations are consistent with previously reported theoretical and experimental studies of the spectral evolution with increasing particle number in many-particle plasmonic systems in the form of 1D chains,[29,171–175] 2D chains,[165,176–178] 2D oligomers and sheets,[111,147–149,154,170,179] and 3D supercrystals.[180,181] The saturating red shift with increasing oligomer size is also analogous to the trend of absorption wavelength for the homologous series of polycyclic aromatic hydrocarbons.[127] In plasmonic structures where the interparticle distance is close enough for near-field interactions among particles, the red shift with increasing particle number has been described by exponentially decaying functions.[29,149,171] This model allows for a description of the characteristic length scale of plasmonic coupling or "delocalization" in large assemblies. The delocalization length is sensitive to both the individual particle size and the gap distance between particles. Because of the single-NC precision conferred by our template-based assembly technique, we have a unique opportunity to characterize the distinctive behavior of 2D assemblies in contrast to the many previous reports on 1D arrays. Theoretical treatments have demonstrated the importance of dimensionality (*i.e.* 2D *versus* 1D) in determining the size-dependent optical properties of NC arrays.[147–149] It is predicted that a large 2D assembly will have a more red-shifted resonance than a large

1D assembly, with the amount of red shift saturating less quickly with increasing oligomer size than for the 1D case. This offers an expanded range of wavelength tunability for applications of 2D assemblies.

Here, the scattering centroid energy $E(N_S)$ in eV for s-polarization as a function of the number of NC shells N_S surrounding the center NC is fit by the function

$$E(N_S) = E_\infty + E_0 \exp\left[-\frac{N_S}{\gamma}\right] \qquad \text{(Eq. 3-1)}$$

where E_∞ represents the resonance energy of an $N_S = \infty$ array, E_0 represents the energy offset for $N_S = 0$, and γ describes the rate of evolution with 2D oligomer size. The fitting curve ($R^2 > 0.99$) is displayed in Figure 3-9d. The fit value for E_∞ is 1.10 eV, implying that an infinite array would have a scattering centroid wavelength λ_∞ of 1130 nm. The $1/e$ point for the function occurs for $N_S = \gamma = 0.33$, suggesting that the spectral response is largely determined by near-neighbor interactions rather than extensive delocalization across the entire oligomer. While it is very difficult to compare our results with reports on systems having different NC sizes and interparticle spacings, the spectra from our 2D oligomers appear to red-shift somewhat further than those for 1D arrays that had slightly larger NC building blocks[172] and much further than those reported for polydisperse ensembles of 2D clusters of slightly smaller NCs.[111]

Eq. 3-1 can also be applied to the data for p-polarization (Figure 3-9b). In this case, the fit value for E_∞ is 2.12 eV, projecting an infinite-array resonance wavelength λ_∞

of 585 nm. This represents a spectral shift $\Delta\lambda$ of only 40 nm from $N_S = 0$ to $N_S = \infty$ for p-polarization, in contrast to a spectral shift $\Delta\lambda$ of 585 nm for s-polarization. The evolution is also much slower for p-polarization, with the $1/e$ point occurring at $N_S = 1.5$. The progression of the spectra under p-polarization can be further explained by considering the average NC coordination number as the oligomer size increases. Coordination number is important in the context of establishing the local dielectric environment of the NCs described above. Figure 3-11 illustrates that the average coordination number gradually saturates for the larger oligomers as the relative proportion of edge-located NCs diminishes in favor of fully coordinated NCs. Superposing the experimental scattering data (Figure 3-11, blue points) shows that the spectral position under p-polarization evolves over a similar length scale as the average coordination number.

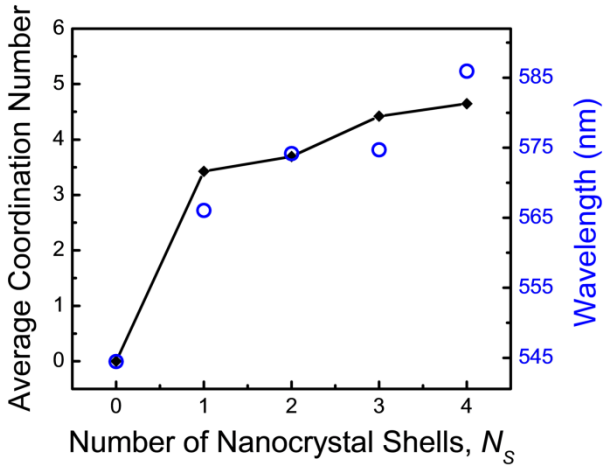

Figure 3-11. Calculated average nanocrystal coordination number (black) and experimental average scattering wavelength for p-polarization (blue) as a function of the number of nanocrystal shells in the oligomer.

A major advantage of single-oligomer measurements as performed here is that the plasmonic response can be analyzed on both an individual and an average basis, whereas ensemble measurements probe only the response as broadened by the inhomogeneity among the ensemble members.[182] It is evident that there are significant variations for each metamolecule configuration among the individual s-polarized spectra presented in Figure 3-6. These likely arise from the structural variations that can be seen in the corresponding SEM images, both in the individual NC components and in their arrangements. For example, the NCs are not perfectly spherical (circularity measured from TEM is 0.87 ± 0.02) and have a size polydispersity of approximately 5%, and several oligomers display visible gaps between NCs due to imperfect packing. To assess the correlation between NC arrangement and plasmon resonance position, quantitative image analysis is performed on the oligomer SEM images. As illustrated in Figure 3-12, the center coordinates of each NC are extracted and used to compute interparticle distances for each unique pair of particles within a given oligomer. Under the assumption of a constant average NC diameter, these center-to-center distances offer a metric for the expected coupling strength between NCs. Note that center-to-center distance is used rather than edge-to-edge distance due to the inability to precisely resolve the interparticle gaps using SEM imaging. It is expected that oligomers with the most tightly packed NCs would exhibit the most red-shifted spectra due to the stronger coupling among the NCs. To test this hypothesis, the correlation between interparticle distance and scattering spectrum centroid is examined for each metamolecule configuration. Figure 3-14a presents one

example, in which the centroid wavelength and average nearest-neighbor interparticle distance for seven different 7-member oligomers are plotted. Performing a linear regression reveals a negative-valued Pearson correlation coefficient of -0.63, indicating that a decrease in interparticle distance correlates with an increase (or red shift) in resonance wavelength as predicted. Figure 3-13 shows the correlation coefficient calculated for all of the metamolecule configurations using nearest-neighbor, second-nearest-neighbor, and third-nearest neighbor distances as well as using the sum of all sets of interparticle distances. In every case there is a negative-valued correlation coefficient, confirming the important role of NC separation in determining the spectral response of the oligomers. This trend is also discernable when the individual scattering spectra are stacked in order of decreasing interparticle spacing (Figure 3-15) for the metamolecule configurations having larger correlation coefficients (e.g. the 19-member configuration), though it is less obvious for others such as the 31-member configuration where smaller correlation coefficients are found.

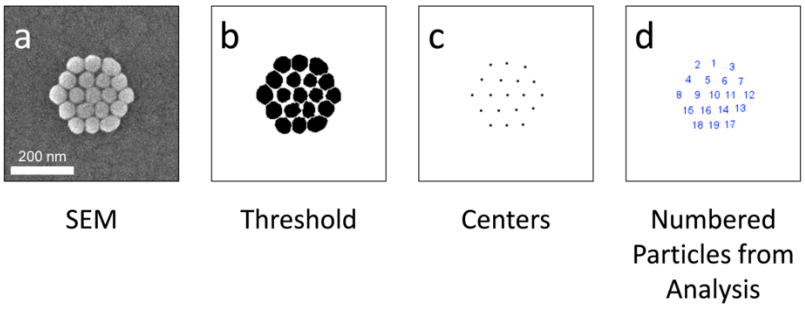

Figure 3-12. Illustration of quantitative image analysis procedure using ImageJ. (a) An SEM image of each oligomer is obtained. (b) A thresholding algorithm is performed to determine the boundaries of each nanocrystal. (c) The center of each nanocrystal is determined using the

"ultimate points" command. (d) (x,y) coordinates are determined for each of the numbered nanocrystals using the particle analysis plugin. The coordinates are then entered into a custom MATLAB script to extract information about interparticle distances.

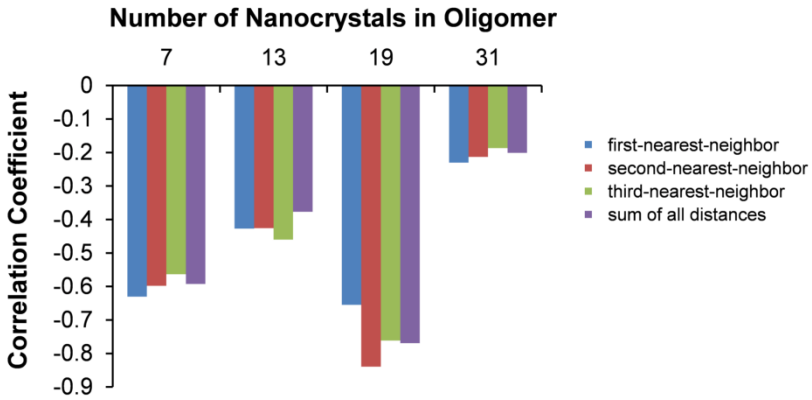

Figure 3-13. Correlation coefficient between average scattering spectrum centroid wavelength and four different interparticle distance metrics: first-nearest-neighbor, second-nearest-neighbor, third-nearest-neighbor, and the sum of all interparticle distances.

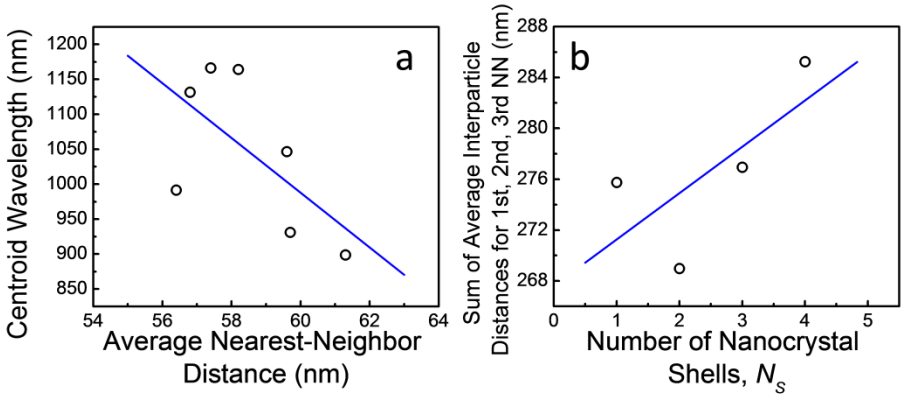

Figure 3-14. (a) Scattering centroid wavelength under s-polarization for seven different 7-member oligomers plotted *versus* the corresponding average nearest-neighbor (NN) interparticle distance within each oligomer. Each 7-member oligomer has 12 unique first-NN NC pairs. (b) Sum of the average first-, second-, and third-NN distances *versus* the number of NC shells (N_S) in each metamolecule configuration. More distant neighbors are excluded since the 7-member oligomers do not have fourth-NN particle pairs. Blue lines in (a) and (b) are linear regressions.

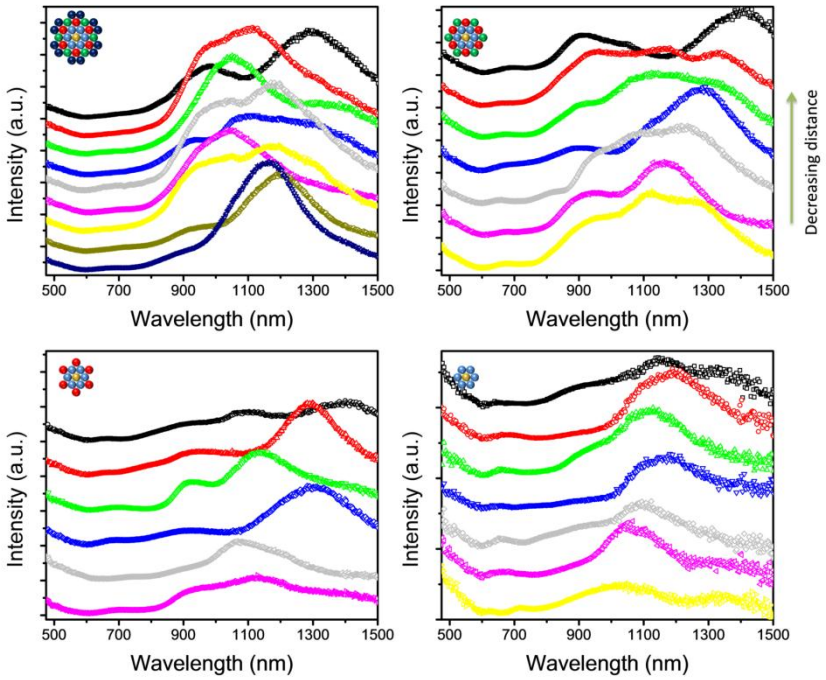

Figure 3-15. Individual s-polarized scattering spectra from each metamolecule configuration stacked in order of decreasing first-nearest-neighbor interparticle distance. In general, a red-shift is observed upon decreasing distance.

The relationship between the quantity of NCs in each metamolecule configuration and the quality of NC packing is also investigated. Figure 3-14b shows a positive correlation (correlation coefficient of 0.78) between the number of NCs in the oligomer and the sum of the average first-, second-, and third-nearest neighbor distances for each metamolecule configuration. While for idealized packing there would be zero correlation, the observed positive correlation indicates that the many-NC oligomers are generally more loosely packed than the few-NC oligomers. This may arise from frustration of the hexagonal lattice upon addition of NCs having non-optimal sizes or positions. The increasing disorder in the larger metamolecule configurations may somewhat diminish

the relative amount of red shift measured compared to that for smaller, more-ordered oligomers.

To gain a greater understanding of the plasmon resonances supported by the oligomers, simulations of the scattering response for each metamolecule configuration are performed. For p-polarization (Figure 3-16), the simulations exhibit a scattering peak at ~560 nm, in agreement with the experimental results and indicating limited interaction among NCs within the oligomer. Because the simulated incident electric field is predominantly orthogonal to the sample plane, spectral features in the 900–1500 nm range are not observable. The experimental spectra show features in this spectral range because the illumination consists of a solid angle of light, which includes additional in-plane electric field components. Under s-polarized illumination, the simulated normalized scattering spectra shown in Figure 3-17a display a significant red shift as the oligomer size increases. The extent of the red shift is similar to that observed in the experimental spectra. For a quantitative comparison, the simulated spectra of Figure 3-17a are analyzed in the same manner as the experimental spectra of Figure 3-9c,d, where the centroid of each curve is extracted to evaluate the spectral evolution. The resulting plot of simulated centroid wavelength *versus* oligomer size is presented in Figure 3-18. The simulations demonstrate a saturating red shift that resembles the experimentally measured behavior, confirming that the large metamolecule configurations begin to approach the response expected from an infinite array of NCs. The experimental results exhibit a slightly faster saturation with increasing oligomer size, which may be a result of the diminishing

compactness of the larger experimental oligomers as described in Figure 3-14b, in contrast to the idealized oligomers in the simulations. Other quantitative differences between the experimental and simulated results may arise from the sensitivity of the simulations to input parameters such as the interparticle spacing and the permittivity of the embedding medium, illustrated in Figure 3-19 and Figure 3-20, respectively.

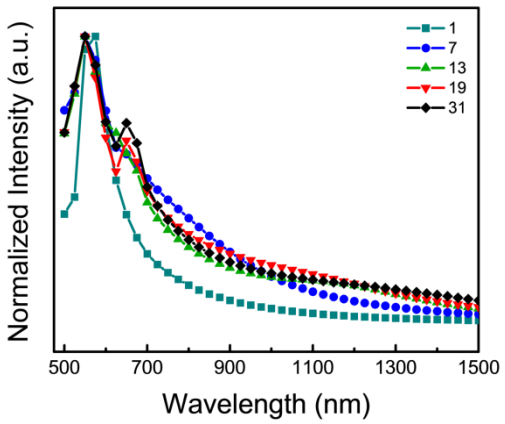

Figure 3-16. Normalized simulated scattering spectrum under p-polarized illumination for each metamolecule configuration. The incident electric field vector is oriented predominantly orthogonal to the substrate plane. The small shoulder visible in the spectra of the larger oligomers results from phase retardation of the incident plane wave across the lateral extent of the oligomers.

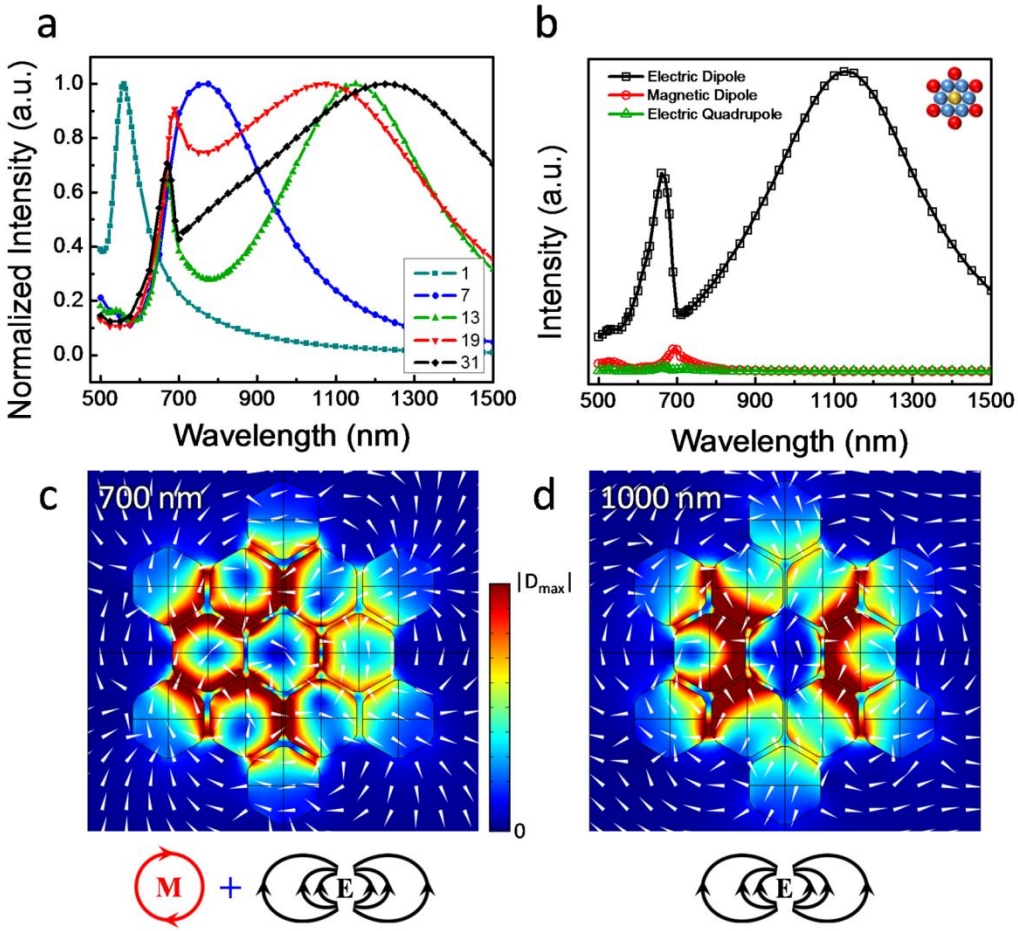

Figure 3-17. (a) Simulated normalized scattering cross-section for each metamolecule configuration. (b) Simulated contributions to the scattering cross section of the 13-NC oligomer from electric dipole, magnetic dipole, and electric quadrupole resonances. (c,d) Simulated electric displacement vector maps for the 13-NC oligomer at (c) 700 nm and (d) 1000 nm. Arrows represent an instantaneous spatial distribution of the vector orientations, and the color maps represent the time-averaged values of the vector magnitudes. Schematics below illustrate the combined electric (E)/magnetic (M) dipole nature of the plasmonic response at 700 nm and the predominantly electric dipole response at 1000 nm. All simulation results are shown for s-polarized illumination.

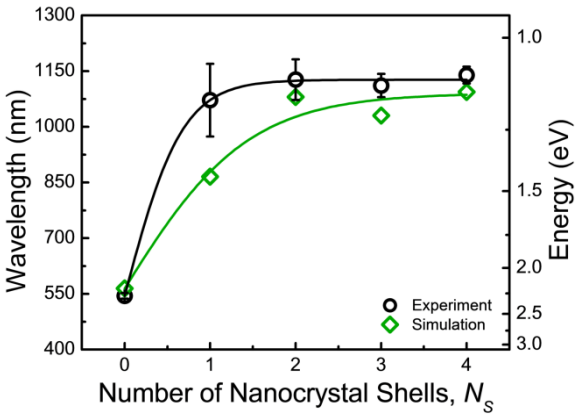

Figure 3-18. Experimental (black) and simulated (green) scattering centroid wavelength under s-polarized illumination *versus* oligomer size. Fit curves are performed using Eq. 3-1. The data points for N_s = 0 represent the center of Lorentzian fits to the single nanocrystal scattering spectra. Error bars represent one standard deviation.

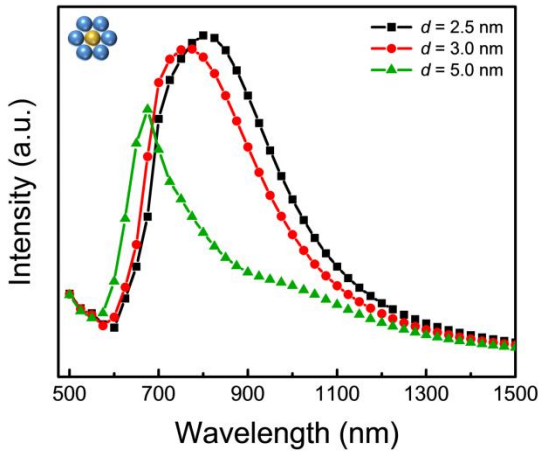

Figure 3-19. Simulated scattering spectra for a 7-membered oligomer under s-polarized illumination as a function of interparticle spacing *d*. Nanocrystals are modeled as faceted spheres in a surrounding medium of relative permittivity ε_r = 2.1.

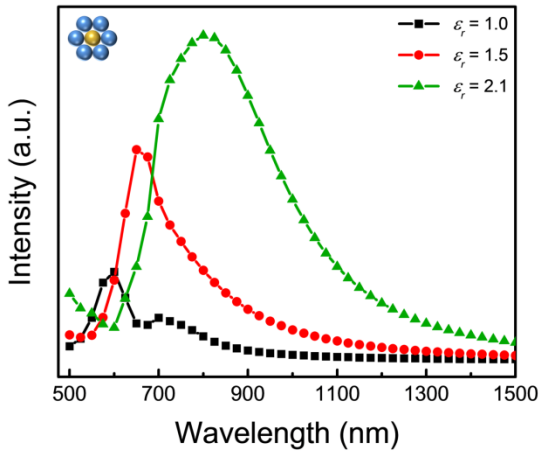

Figure 3-20. Simulated scattering spectra of a 7-membered oligomer under s-polarized illumination as a function of the relative permittivity ε_r of the surrounding medium. Nanocrystals are modeled as faceted spheres with an interparticle spacing of d = 2.5 nm.

The simulated scattering spectra in Figure 3-17a for the larger metamolecule configurations exhibit multiple scattering features, similar to those present in many of the experimental spectra in the right panel of Figure 3-6. The origin of these features is better understood through simulation of the electric dipole, magnetic dipole, and electric quadrupole contributions to the total scattering cross-section. As an example, Figure 3-17b considers the case for the 13-NC metamolecule configuration. Here, the scattering response is largely dominated by an electric dipole resonance, but there is a significant dip in the spectrum at 700 nm, which coincides with the position of a magnetic dipole resonance. As shown by Shafiei *et al.*, the interference between a broad, radiant electric dipole resonance and a narrow, subradiant magnetic dipole mode can result in an optical Fano resonance manifested as a characteristic dip in the scattering spectrum.[142] The combined electric and magnetic dipole nature of the plasmon modes in our oligomers is

further demonstrated by electric displacement vector maps calculated at the spectral position of the Fano dip (700 nm, Figure 3-17c) and within the broad electric dipole resonance (1000 nm, Figure 3-17d). While the field map at 1000 nm displays the classic pattern associated with an electric dipole, the field map at 700 nm also reveals electric displacement vectors oriented in a circular manner due to the magnetic dipole orthogonal to the plane of the oligomer. The circulating field distributions in our plasmonic oligomers are also reminiscent of ring currents in polycyclic aromatic hydrocarbons such as coronene.[183] The multipolar analysis and electric displacement field maps for the rest of the metamolecule configurations are included in Figure 3-21. The single-NC and 7-NC oligomers exhibit predominantly electric dipole responses, while the 13-NC and larger oligomers express the influence of magnetic dipole contributions. The electric quadrupole contribution is nearly negligible for all metamolecule configurations, increasing slightly for the largest structures.

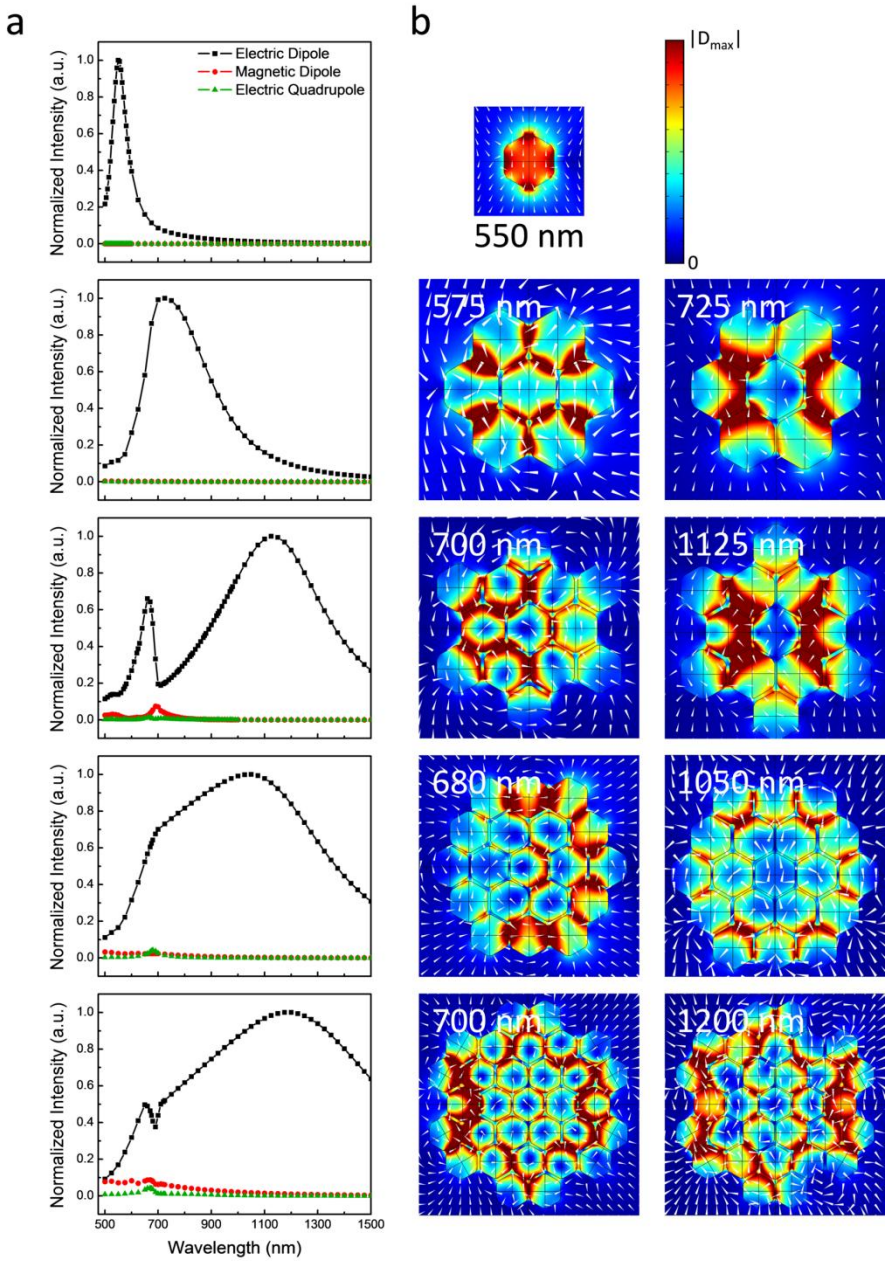

Figure 3-21. (a) Simulated electric dipole, magnetic dipole, and electric quadrupole contributions to the overall scattering cross section for each metamolecule configuration under s-polarized illumination. (b) Simulated electric displacement vector distributions at the indicated wavelengths. Color scale represents the time-averaged magnitude of the electric displacement. Nanocrystals are the same size in each simulation; figures are scaled for clarity.

Simulations also enable an exploration of the role of NC positional disorder in determining the plasmonic response of the oligomers. As an illustration, the scattering spectra of an ordered and a disordered 19-NC oligomer are simulated, with the geometrical arrangement of the NCs extracted from experimental SEM images, as shown in Figure 3-22. The oligomer with greater positional order (and thus smaller average interparticle gaps) displays a significantly red-shifted resonance in the simulation compared to the disordered (more widely spaced) oligomer. This result is consistent with the experimentally measured spectra for these two oligomers (Figure 3-23), and exemplifies the general trend observed in the experimental data of increasing red shift for well-ordered oligomers. Comparison of the simulated multipole analysis of the two oligomers in Figure 3-22 suggests that disorder enhances the influence of magnetic dipole and electric quadrupole resonances on the overall plasmonic response. This is in agreement with the report of Shafiei *et al.* that symmetry breaking magnifies the interaction of otherwise orthogonal electric and magnetic modes.[142] The simulated scattering cross section for the disordered oligomer therefore exhibits greater complexity in the spectral features than for the more ordered case. The multiple peaks and dips in the simulated spectrum resemble the features observed in many of the experimental scattering spectra. The variations in NC position within our experimentally realized oligomers also account for the range of plasmonic responses measured for different examples of each metamolecule configuration.

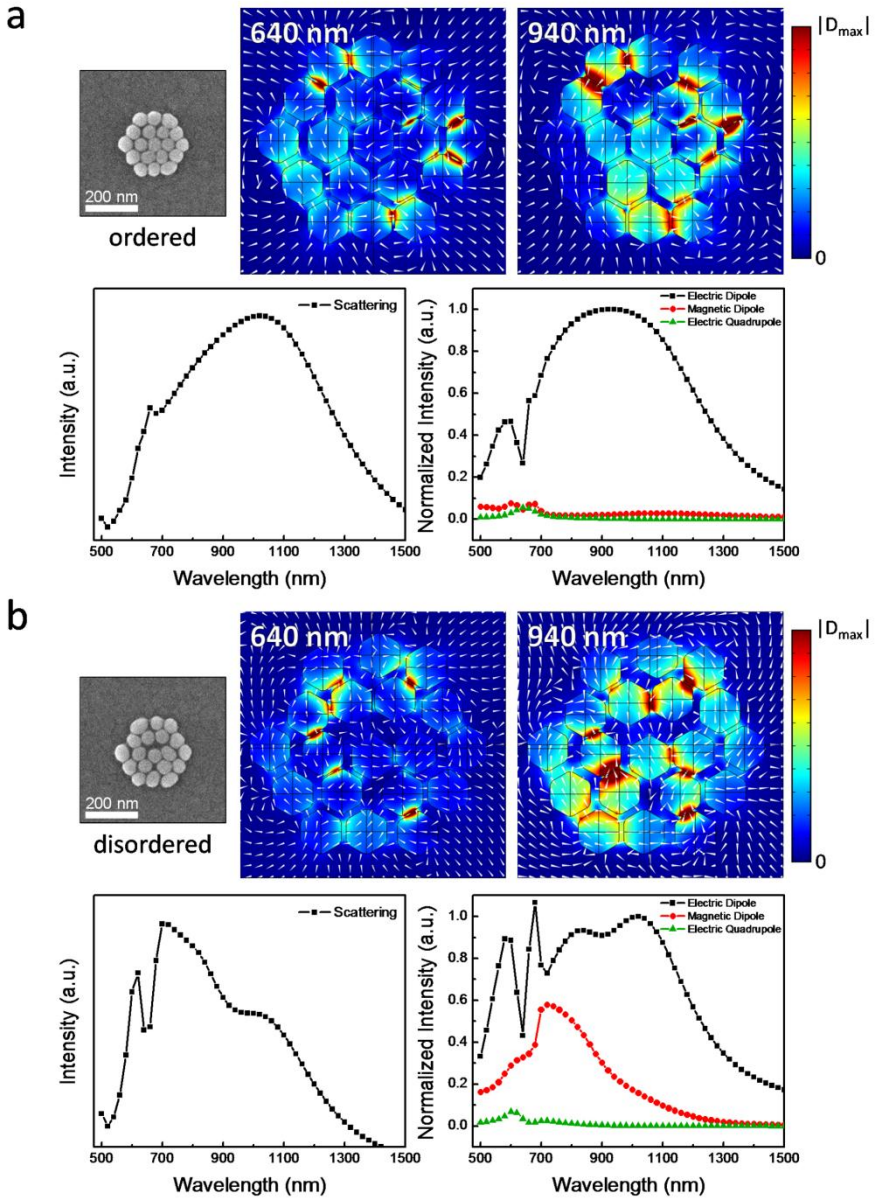

Figure 3-22. Simulated electric displacement vector maps, scattering spectra, and multipole analysis for (a) an ordered and (b) a disordered 19-NC oligomer under s-polarized illumination. The geometrical arrangement of the particles is extracted from the SEM images of the two experimentally formed oligomers shown. Note that the interparticle spacing for the ordered oligomer is scaled by 5% to avoid overlapping NC volumes in the simulation.

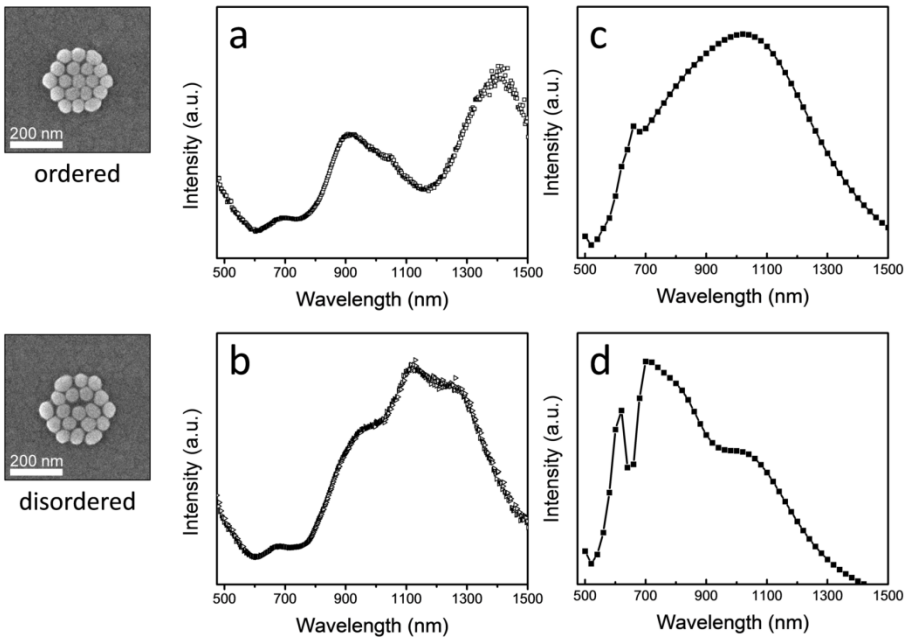

Figure 3-23. Experimental (a,b) and simulated (c,d) scattering spectra for the pictured ordered and disordered 19-membered oligomers (also described in Figure 3-22). In both experiment and simulation, the ordered oligomer displays a more red-shifted scattering spectrum centroid than the less ordered oligomer.

3.3 Conclusions

In summary, we utilize polygonal templates to direct the self-assembly of precise, hexagonally-packed oligomers containing 1, 7, 13, 19, and 31 Au NCs. Polarized darkfield scattering spectroscopy with single-oligomer sensitivity enables us to probe the out-of-plane and in-plane plasmonic modes supported by individual oligomers. We observe an exponentially saturating red shift of the plasmon resonance wavelength with increasing oligomer size, mapping the plasmonic response as the metamolecule configurations begin to approach an infinite two-dimensional array of NCs. Image analysis reveals the role of NC positional disorder in determining the unique optical

response of individual oligomers, while simulations confirm the size-dependent spectral characteristics and elucidate the contribution of electric dipole, magnetic dipole, and Fano resonant modes to the scattering spectra. With this improved understanding of the plasmonic properties of intermediate-sized NC metamolecules prepared through a versatile assembly method, a greater diversity of functional metamaterials can be achieved with attractive future applications.

3.4 Methods

3.4.1 Nanocrystal Synthesis

Preparation of CTAB-coated Au NCs is based on the method reported by Liz-Marzán *et al*.[184] Briefly, a solution of ascorbic acid (AA) is injected into a solution of $HAuCl_4$ and CTAB at 35°C under vigorous stirring with [Au] = 1 mM, [CTAB] = 1.5 mM, and [AA] = 2 mM. The injection is quickly followed by the addition of Au seeds previously prepared using the Turkevich method. The size of the NCs is tuned by adjusting the amount of seed injected into the solution.

3.4.2 Template Fabrication and Nanocrystal Assembly

Double-side-polished germanium wafers (undoped, 250 μm thickness, Wafer World Inc.) serve as the substrate. After sonication in acetone and rinsing with acetone and isopropyl alcohol (IPA), the wafers are cleaned using an O_2 plasma (Gatan Solarus) for 5 min. Then, 250 nm of SiO_2 is deposited on the wafers by plasma-enhanced chemical vapor deposition (PECVD, Oxford Plasmalab System 100). The SiO_2 thickness is

confirmed using spectral reflectance measurements (Filmetrics F40). Poly(methyl methacrylate) (PMMA) positive e-beam resist (MicroChem) is spun onto the substrate in two layers: (1) 495K molecular weight (MW) PMMA in anisole is spun at 2400 rpm for 90 sec followed by a 4 min bake at 180 ℃, and then (2) 950K MW PMMA in anisole is spun at 2400 rpm for 90 sec followed by a 4 min bake at 180 °C. The total PMMA thickness measured by spectral reflectance is 67 nm. The template pattern is written by electron-beam lithography (Elionix ELS-7500EX) using a 50 kV accelerating voltage and a 50 pA beam current. The resist is developed by a 90-second immersion in a solution of methyl isobutyl ketone (MIBK) and IPA of a 1:3 ratio, followed by rinsing with IPA. An 8-second O_2 plasma descum treatment is then performed, resulting in a final PMMA thickness of 59 nm. Au NCs are assembled using the custom-built capillary assembly apparatus described above (Figure 3-4a). An aqueous dispersion of Au NCs is dispensed between the substrate and a fixed glass slide. The substrate is translated by a motorized linear stage (New Focus Picomotor) at a rate of 8 μm/sec, and capillary forces at the meniscus direct the assembly of NCs into the template features. The entire assembly apparatus is enclosed in a humidity-controlled environment, and the substrate temperature is regulated by a water-cooled stage monitored by a thermocouple. During assembly the substrate temperature is 15 ℃, and the ambient dew point is maintained at 0 ℃ through the controlled introduction of dry nitrogen. Following assembly, resist liftoff is performed by soaking in acetone.

3.4.3 Structural and Optical Measurements

Scanning electron microscopy is performed using a JEOL 7500F HRSEM and an FEI Quanta 600 ESEM operating at 10 kV. Transmission electron microscopy is performed on a JEOL JEM-1400 TEM operating at 120 kV. Reflection-mode darkfield scattering is collected using a modified Olympus BX51 microscope. White light from a 150-W quartz tungsten halogen lamp with an aluminum reflector is routed to the microscope through an optical fiber bundle. After collimation by a plano-convex lens, the light passes through a rotatable broad-band linear polarizer before being refocused on the sample surface by another lens. The illumination spot is projected across the entire field of view of the collection objective. The elevation angle of the illumination is approximately 10 degrees above horizontal. Scattered light from the sample is collected by a NIR-optimized objective lens (Olympus LCPLN50XIR, NA 0.65). The indicated illumination and collection geometry establishes a darkfield configuration where direct reflection of the incident light is outside the collection cone of the objective. The scattered light is routed by a 100-μm-core optical fiber to the final stage of a Princeton Instruments Tri-Vista 555 spectrometer equipped with a PIXIS-256E Si 2D array detector and an OMA-V InGaAs linear array detector for visible and NIR measurement, respectively. Each scattering spectrum is normalized by the spectral profile of the illumination source, followed by subtraction of baseline scattering from a blank area of the substrate containing no NCs.

3.4.4 Simulations

All numerical calculations are carried out in COMSOL Multiphysics® using the frequency domain solver. The oligomers are illuminated by an incident plane-wave with an elevation angle of 10 degrees above horizontal, and the simulation setup is terminated into a spherical surface covered by a perfect matched layer. We use faceted NCs constructed from the intersection of a sphere of diameter 60 nm and a hexagonal prism of height 55 nm. This ensures that the face-to-face distance is 55 nm. Faceted particles are chosen in order to approximate the nearly planar interfaces between NCs observed in the experimental TEM and SEM images. The separation between particle edges of adjacent nanocrystals is 3 nm. The NCs are surrounded by a dielectric medium of height 110 nm and relative permittivity ε_r = 2.1, with the permittivity chosen to approximate that reported[185] for the CTAB surfactant. Note that the effects of varying the interparticle spacing and the permittivity are reported in Figure 3-19 and Figure 3-20, respectively. The substrate is not represented explicitly in the simulations, which may slightly reduce the overall red shift compared to the experimental results. However, the influence of the substrate is effectively incorporated by embedding the oligomers in the surrounding dielectric medium.[186] Material data for the Au NCs is obtained from empirical data sets.[187] Separate calculations are conducted for p- and s-polarizations of the incident field. After computation of the electromagnetic fields by the numerical solver, the scattering cross-section (SCS) spectra are obtained from field integration

$$\mathrm{SCS} = \frac{1}{S_i}\frac{1}{2}\oint_A \mathrm{Re}\{\boldsymbol{E_s} \times \boldsymbol{H_s^*}\} \cdot \hat{\mathbf{n}} dS \qquad \text{(Eq. 3-2)}$$

where $\boldsymbol{E_s}$, $\boldsymbol{H_s}$ are the scattered electric and magnetic fields, respectively, and $S_i = |E_0|^2/(2\eta_0)$ is the incident power density. Following Shafiei *et al.*,[142] additional post-processing is utilized to determine the contributions of different multipoles to the SCS. These are identified from the distribution of polarization current, $\boldsymbol{J}_p(\mathbf{r}) = -i\omega\varepsilon_0[\varepsilon_r(\mathbf{r}) - 1]\boldsymbol{E}(\mathbf{r})$, in the following manner

$$\mathbf{p} = -\frac{1}{i\omega}\int_V \boldsymbol{J}_p(\mathbf{r}')\, dV' \qquad \text{(Eq. 3-3)}$$

$$\mathbf{m} = \frac{1}{2}\int_V \mathbf{r}' \times \boldsymbol{J}_p(\mathbf{r}')\, dV' \qquad \text{(Eq. 3-4)}$$

$$\overleftrightarrow{\mathbf{Q}} = -\frac{1}{i\omega}\int_V \left[\mathbf{r}'\boldsymbol{J}_p(\mathbf{r}') + \boldsymbol{J}_p(\mathbf{r}')\mathbf{r}'\right] dV' \qquad \text{(Eq. 3-5)}$$

Their contributions to the scattered power are given by

$$\text{Electric Dipole} = \frac{k_0^4}{12\pi\eta_0\varepsilon_0^2}\,|\mathbf{p}|^2 \qquad \text{(Eq. 3-6)}$$

$$\text{Magnetic Dipole} = \frac{k_0^4\eta_0}{12\pi}\,|\mathbf{m}|^2 \qquad \text{(Eq. 3-7)}$$

$$\text{Electric Quadrupole} = \frac{k_0^6}{40\pi\eta_0\varepsilon_0^2}\,\left\|\overleftrightarrow{\mathbf{Q}}\right\|^2 \qquad \text{(Eq. 3-8)}$$

CHAPTER 4. PLASMONIC OPTICAL AND CHIROPTICAL RESPONSE OF SELF-ASSEMBLED AU NANOROD EQUILATERAL TRIMERS

4.1 Introduction

Plasmonic oligomers inspired by nature's molecular building blocks continue to draw interest as a pathway toward optical metamaterials that interact with light in unique ways.[131,188,189] While the properties of oligomers composed of spherical nanocrystals have been extensively explored,[28,139,140,157,190] arrangements of high-aspect-ratio nanoparticles beyond variations of simple end-to-end and side-to-side configurations have received far less treatment. The non-isotropic nature of nanorods, however, opens new avenues for engineering the collective plasmonic response of oligomers. A triangular arrangement of nanorods, in particular, has been proposed as an important structural unit for forming assemblies with magnetic–magnetic hybridized plasmon modes and all-magnetic Fano interferences.[191] The optically-induced amplified magnetic field intensity within the triangle also offers a promising route to enhance magnetic dipole transitions[192–194] in luminescent materials. Furthermore, in contrast to a triangular arrangement of spheres, in a nanorod trimer the mirror symmetry can be broken while retaining rotational symmetry, generating planar chiral enantiomers with potential chiroptical properties. Developing chiral metamaterials remains an active research area,

motivated by applications including chiral catalysis,[195] high-sensitivity DNA detection,[196,197] and enantioselective sensing of chemical analytes.[198]

While nanospheres often form trimers during random self-assembly because of their close-packed structure,[139] nanorods often assemble in side-to-side and end-to-end arrangements with a distribution of inter-rod angles.[199–204] To achieve the necessary control to obtain triangular configurations of Au nanorods, here we utilize template-assisted self-assembly[16,28,30,164] to direct the nanorod arrangement. We characterize the optical properties of individual nanorod trimers using spatially-resolved darkfield scattering spectroscopy. In conjunction with numerical simulations, we elucidate the orientation- and polarization-dependent plasmonic modes under linearly and circularly polarized excitation, including the interplay of electric and magnetic plasmon modes and their chiroptical response.

4.2 Results and Discussion

We design templates in the shape of an equilateral triangle to assemble Au nanorods (Au NRs) into triangular arrangements. As shown in Figure 4-1, configurations consisting of one, two, and three Au NRs assembled along the edges of a triangular template are formed. The templates are defined as topographical features in poly(methyl methacrylate) (PMMA) and are patterned using electron-beam lithography. The template dimensions are tailored so that each side of the triangle accommodates a single Au NR. A transmission electron microscopy (TEM) image of the Au NRs, which have an average length of 110 ± 8 nm and diameter of 22 ± 3 nm (aspect ratio 5:1), is given in Figure

4-2a. The Au NRs support localized surface plasmon resonances along their longitudinal and transverse axes, which appear as peaks in their extinction spectrum at 915 nm and 510 nm, respectively (Figure 4-2b).

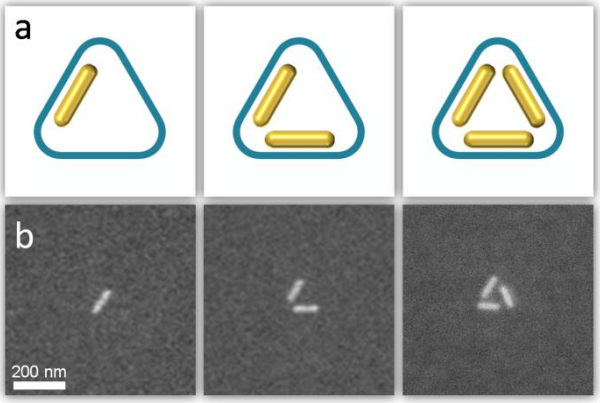

Figure 4-1. Assembly of one, two, and three Au nanorods along the edges of triangular templates. (a) Schematic representation. (b) Scanning electron microscopy (SEM) images, shown after resist liftoff.

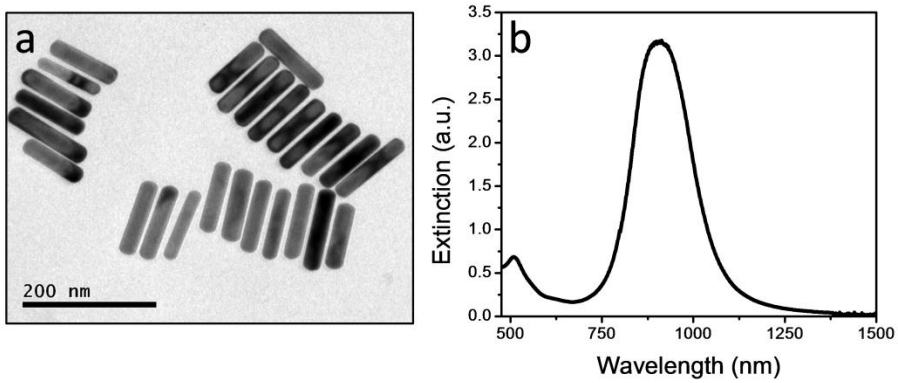

Figure 4-2. (a) TEM image of Au nanorods having average length of 110 ± 8 nm and diameter of 22 ± 3 nm. (b) Ensemble extinction spectrum of the nanorods dispersed in water, exhibiting longitudinal and transverse surface plasmon resonances centered at 915 nm and 510 nm, respectively.

The Au NRs are assembled into the triangular templates using a capillary assembly method previously demonstrated by our group for the assembly of Au NRs[20] and Au nanocrystals.[21] Briefly, an aqueous dispersion of Au NRs is dispensed between the templated substrate and a fixed glass slide, and as the substrate is translated by a motorized stage, capillary forces at the liquid meniscus direct the Au NRs to assemble within the templates. Additional details about the assembly process are provided in Section 4.4.2. Following assembly, liftoff in acetone removes the patterned PMMA resist layer, leaving behind Au NR assemblies at precise locations on the sample surface.

The assemblies are characterized structurally using SEM; then, the correlated optical properties of selected individual Au NR structures are probed using spatially-resolved darkfield scattering spectroscopy.[21] The scattering spectra are first measured under two conditions of linear polarization, as depicted in Figure 4-3. Broad-band light passing through a linear polarizer is focused obliquely on the sample at an elevation angle of 10°, and the light scattered normal to the sample surface is collected by the microscope objective. The numerical aperture of the objective (N.A. = 0.65) is chosen such that the direct reflection of the incident beam is excluded from collection, establishing a darkfield measurement geometry. The scattered light is routed to a spectrometer for detection by an optical fiber, whose 100 μm core spatially restricts the corresponding collection area on the sample surface to a region approximately 2 μm in diameter. Because the individual templates are positioned in an array with a spacing of 10 μm, the scattering spectrum from an individual Au NR structure can be obtained. By orienting the linear polarizer

either vertically or horizontally, conditions of p-polarization and s-polarization are established, respectively. As illustrated in Figure 4-3b, under p-polarization the incident electric field is oriented primarily out of the plane of the substrate (with a small in-plane component), while under s-polarization the incident electric field is completely parallel to the plane of the substrate.

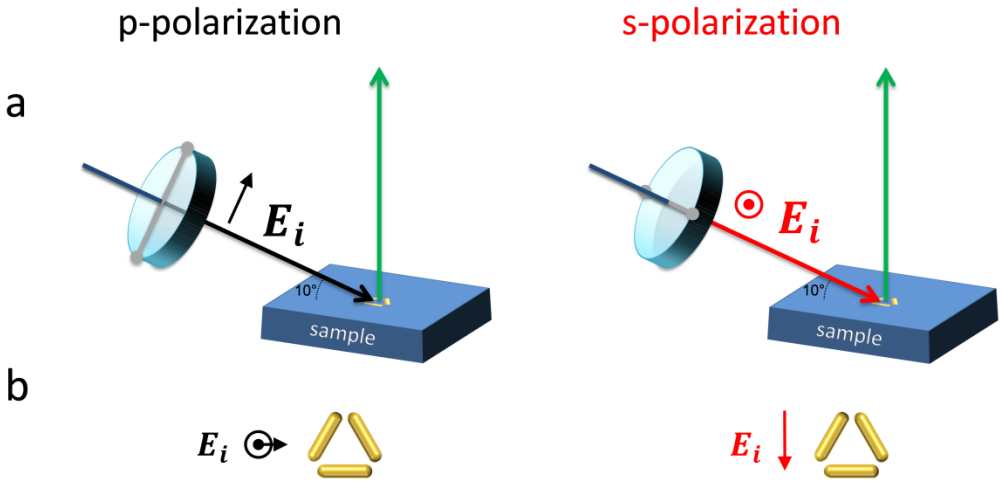

Figure 4-3. Schematics of the darkfield scattering geometry for p-polarization and s-polarization. (a) Perspective view. (b) Top view. The excitation is incident from left to right. With a 10° incident elevation angle, for p-polarization the electric field is oriented primarily out of the substrate plane with a small in-plane component. For s-polarization, the incident electric field is oriented completely within the plane of the substrate. Note that the in-plane electric field components for p- and s-polarization are orthogonal to each other.

To better understand the collective plasmonic response of the Au NR trimer, we consider how the scattering spectrum evolves as the configuration is constructed one Au NR at a time. Figure 4-4 presents individual scattering spectra from one, two, and three Au NRs assembled along the edges of triangular templates. For the single Au NR, a strong scattering feature is present at around 900 nm, resulting from excitation of the

longitudinal surface plasmon resonance. The position of the resonance is similar to that in the solution-phase ensemble measurement (Figure 4-2b), but the line shape is much narrower because the single-particle scattering measurement excludes the heterogeneous broadening associated with Au NR size polydispersity in the ensemble measurement. The signal for s-polarization is much stronger than that for p-polarization, since the electric field under s-polarization and the longitudinal axis of the Au NR are both parallel to the plane of the substrate. Features associated with out-of-plane electric fields (*i.e.* transverse to the Au NR) are expected to be weak due to the low scattering efficiency of the transverse plasmon mode. The peak that appears for p-polarization is instead due to the in-plane electric field component's excitation of the longitudinal plasmon resonance.

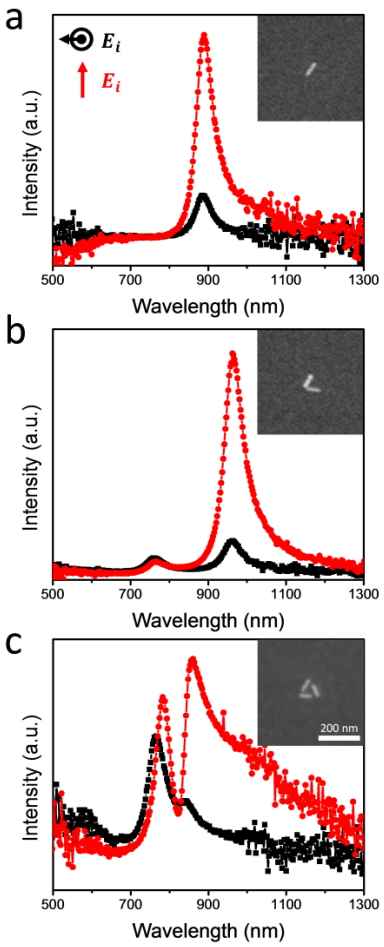

Figure 4-4. Darkfield scattering spectra of the structures shown in the inset SEM images: (a) one, (b) two, and (c) three Au nanorods assembled along the edges of a triangular template. Excitation light is incident from the right with either p-polarization (black) or s-polarization (red). Within each panel, intensity is normalized by the peak intensity of the s-polarization spectrum.

For the structure containing two nanorods (Figure 4-4b), the scattering spectrum exhibits two peaks. The more intense peak (at around 965 nm) is red-shifted with respect to the longitudinal plasmon resonance of the single rod, while the weaker peak (at around 765 nm) is blue-shifted. This behavior is consistent with the hybridization of the longitudinal resonances of the two individual nanorods into collective bonding and

antibonding hybrid modes appearing at lower and higher energy, respectively, as previously reported for angled nanorod dimers.[201,203–205] The bonding mode arises from out-of-phase charge oscillations in the two nanorods, while the antibonding mode is associated with in-phase oscillations. The greater relative intensity of the long-wavelength bonding mode seen in Figure 4-4b is also consistent with previous observations.[204]

The scattering spectrum of the three-rod triangle (Figure 4-4c) displays two closely-spaced features. Previous reports on trimers made up of spherical particles[140,141] and of fabricated elongated Ag disks[191] suggest that the features may arise from two different plasmon resonances, one with magnetic dipole character and the other with electric dipole character. The magnetic mode is associated with a head-to-tail arrangement of electric dipoles along the long axes of the nanorods, setting up a circulating pattern around the periphery of the triangle. In this configuration, a magnetic dipole is oriented perpendicular to the plane of the triangle, while there is no net electric dipole moment. In contrast, the electric mode contains head-to-head arrangements of electric dipoles and therefore a non-zero net electric dipole moment. Preferential excitation of the magnetic *versus* the electric mode is strongly dependent on the excitation geometry, with the magnetic mode only excited when the incident light has a magnetic field component perpendicular to the plane of the triangle.[141,191] For our obliquely incident illumination geometry, s-polarization contains an out-of-plane magnetic field while p-polarization does not. Therefore, s-polarization is expected to

excite the magnetic mode to a greater extent than p-polarization. The spectra of Figure 4-4c show that the peak at around 860 nm is preferentially excited by s-polarization, while the 775 nm peak is excited by both s- and p-polarization. While not a definitive indication that the 860 nm peak results from a magnetic mode, this observation is not incompatible with an assignment as a magnetic mode. The magnetic mode is expected to have a lower energy than the electric mode,[141,191] which is also consistent with an assignment of the low-energy 860 nm feature as a magnetic mode and the higher-energy 775 nm feature as an electric mode.

To better understand the plasmon modes and spectral features, we numerically simulate the optical response of the three-rod structure. Figure 4-5 presents the simulated scattering spectrum under s-polarized illumination overlaid with the corresponding experimentally measured spectrum. The wavelengths of the two spectral features as well as their relative intensities are overall in agreement with the experimental results. In order to interpret the modes associated with the scattering features, maps of the electric field distribution at the wavelengths of the two features are simulated (Figure 4-6). Because the incident electric field is oriented in the *y* direction in the plane of the triangle, the two rods pointing mainly in the +*y* direction interact strongly with the incident light but the rod oriented along the *x* direction is not strongly excited. In the field map for the high-energy spectral feature (Figure 4-6a), a head-to-head configuration of electric dipoles is visible, supporting our assignment of this mode as an electric dipole mode. However, the assignment of the low-energy mode (Figure 4-6b) from the field map is more ambiguous.

Therefore, future simulations will decompose the scattering spectrum into its magnetic dipole and electric dipole contributions[21,142] to further assess the nature of the low-energy mode.

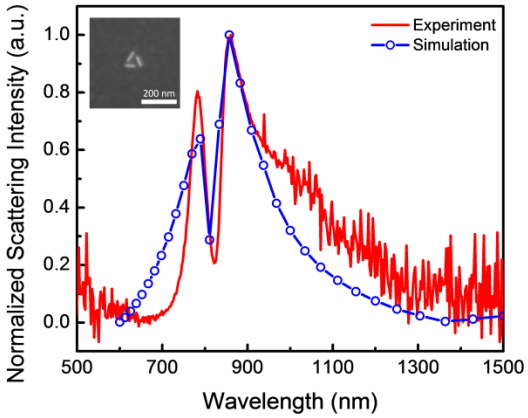

Figure 4-5. Experimental (red) and simulated (blue) scattering spectra for the Au nanorod trimer shown in the inset SEM image under s-polarized illumination. The intensity of each spectrum is normalized by its maximum value.

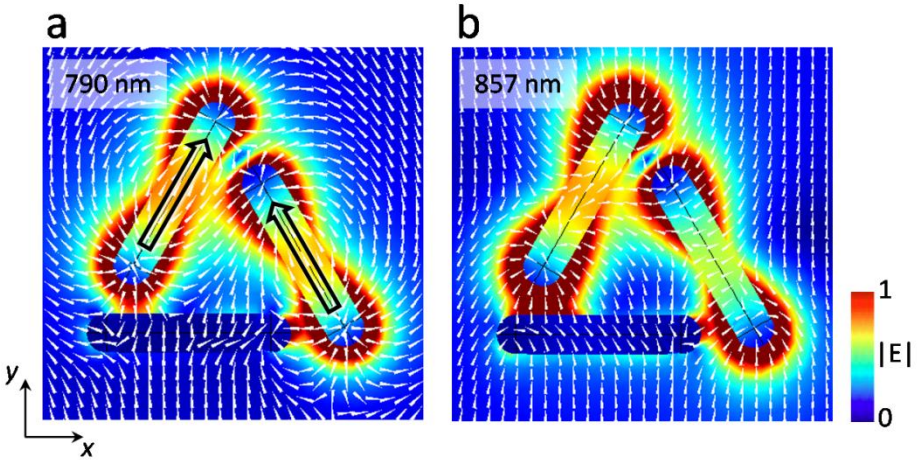

Figure 4-6. Simulated electric field distributions under s-polarized illumination. The incident electric field is oriented along the *y* direction. Simulations are at the wavelengths of the two scattering features shown in Figure 4-5: (a) 790 nm and (b) 857 nm. The small white arrows indicate the direction of the electric displacement field. The overlay of black arrows in (a)

emphasizes the head-to-head configuration of electric dipoles, while the field map in (b) is more ambiguous to assign.

The experimentally measured scattering spectra of the Au nanorod trimers are sensitive to structural deviations in the nanorod arrangement. To illustrate, Figure 4-7 presents scattering spectra from nine different nanorod trimers. While the spectra generally exhibit two or three peaks in the 700–950 nm wavelength range, the positions and relative intensities of the peaks vary. There are several sources that contribute to this variation that can be seen by examination of the inset SEM images in Figure 4-7. First, there is some polydispersity in the size of the individual nanorods that make up the trimers. Second, the spacing between individual Au NRs (and therefore the strength of their coupling) varies. Third, there are small angular deviations of the rod alignment with respect to an ideal equilateral triangle. Symmetry breaking induced by these geometrical variations may have important consequences for the formation of Fano interferences between different plasmonic modes.[141,191]

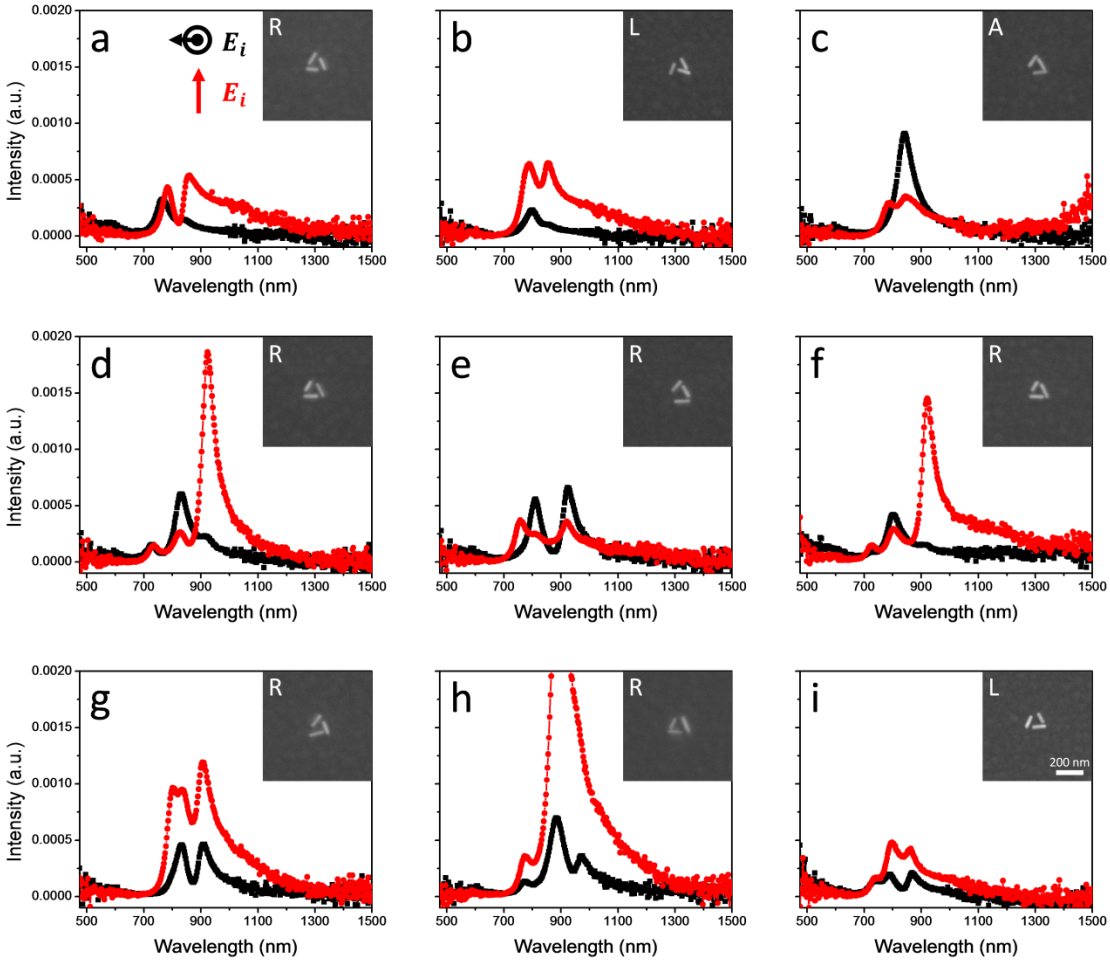

Figure 4-7. Darkfield scattering spectra of the Au nanorod trimer structures shown in the inset SEM images. Excitation light is incident from the right with either p-polarization (black) or s-polarization (red). Labels of L, R, and A refer to designations as left-enantiomer, right-enantiomer, and achiral structures.

The Au NR trimers can further be classified by the 2D chirality of their geometry. Figure 4-8 illustrates that a Au NR configuration having mirror symmetry planes along each altitude of the triangle represents an achiral structure, while "left-handed" and "right-handed" 2D enantiomers result when the rods are displaced axially from the centers of the triangle edges in either of two directions. While the enantiomers as

illustrated can be superimposed by rotation in three dimensions and are therefore not chiral in three dimensions, the structures can be said to be two-dimensionally chiral. Including the fact that the structures are supported by a substrate, however, removes the mirror symmetry across the plane of the triangle, and may render the structures fully three-dimensionally chiral. The geometry of the darkfield scattering measurement introduces further symmetry breaking, since the excitation is from only one direction in 3D space. This type of excitation can result in "extrinsic chirality" in the optical response of otherwise intrinsically achiral structures.[205]

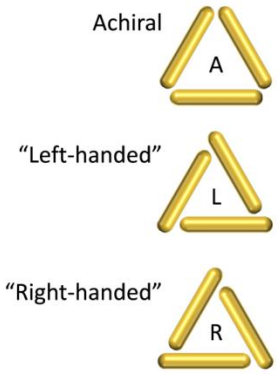

Figure 4-8. Schematic depiction of an achiral nanorod trimer and left-handed and right-handed 2D chiral enantiomers. The choice of L *versus* R as the designation is arbitrary.

Chirality in the optical response of the Au NR trimers is investigated by performing darkfield scattering measurements using circularly polarized illumination. By comparing the scattering intensity under left-circular polarization (LCP) and right-circular polarization (RCP), the preference of the structure for interaction with light of a certain chirality is evaluated. To set up LCP and RCP in our darkfield scattering system, a quarter wave plate is inserted in the excitation path after the linear polarizer. By

orienting the fast axis of the quarter wave plate at ± 45° with respect to the axis of linear polarization, LCP or RCP illumination is obtained. The absence of significant residual linear polarization (which would result in elliptical rather than circular polarization) is confirmed by measuring the illumination intensity as a second linear polarizer is rotated after the quarter wave plate (Figure 4-9).

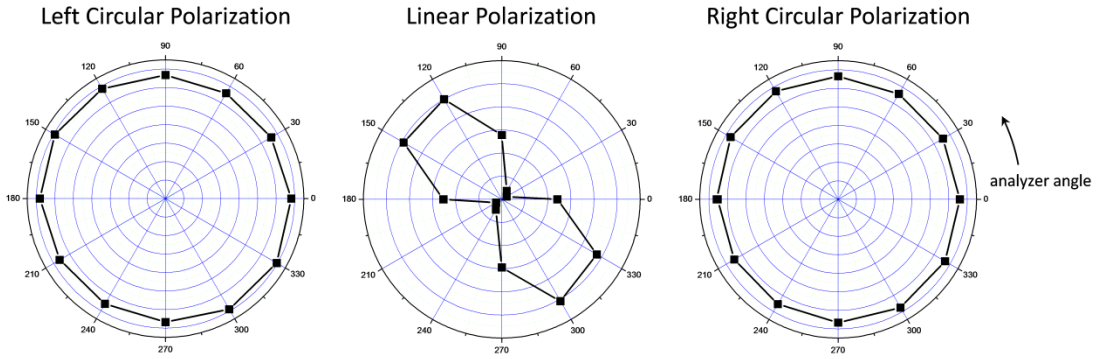

Figure 4-9. Polar plots of illumination intensity as a function of the rotation of an analyzer polarizer placed after the quarter wave plate. Residual ellipticity in the LCP and RCP illumination is low, as desired.

The degree of chiroptical response is assessed by calculating the percent circular differential scattering (%CDS):

$$\%\mathrm{CDS} = \frac{(I_{LCP} - I_{RCP})}{\left(\frac{I_{LCP} + I_{RCP}}{2}\right)} \times 100\% \qquad \text{(Eq. 4-1)}$$

where I_{LCP} and I_{RCP} are the scattering intensities under LCP and RCP illumination, respectively. An example is pictured in Figure 4-10, which shows individual spectra for LCP and RCP illumination and the resulting %CDS spectrum for a representative nanorod trimer structure. The spectra indicate that each of the peaks shows a preferential

excitation by either LCP or RCP illumination, leading to positive or negative values of %CDS, respectively.

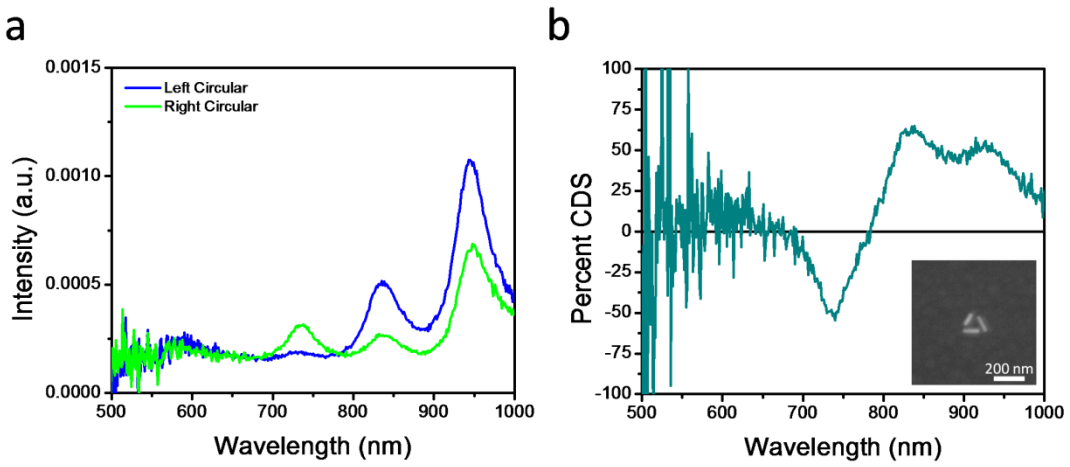

Figure 4-10. (a) Scattering spectra under left-circular and right-circular polarized illumination and (b) percent CDS spectrum for the structure pictured in the inset SEM image. The excitation is incident from the right.

To evaluate whether the nonzero %CDS may be a result of the particular azimuthal angle of excitation used (0°, or incident from the right in Figure 4-10), the %CDS was measured at increments of 30° over a full 360° in-plane rotation of the sample. The %CDS spectrum averaged over these azimuthal angles is shown in Figure 4-11. The averaged spectrum exhibits a predominantly positive %CDS in the spectral region of the plasmon resonances (~700–1000 nm), which may suggest that this particular configuration of Au NRs interacts overall more strongly with LCP than with RCP illumination. Future experiments and simulations will assess whether this preference can be reproducibly correlated with the geometric 2D chirality of a given trimer. Control experiments measuring the %CDS of a single Au NR and a single Au sphere will also be

performed to indicate whether an average non-zero %CDS is a property conferred by the 2D chiral nature of the trimer structure.

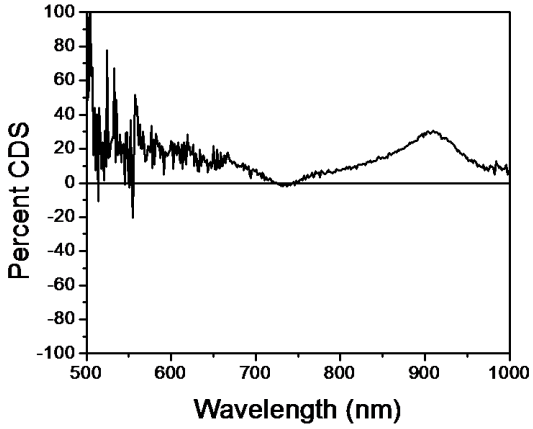

Figure 4-11. Percent CDS spectrum averaged over azimuthal rotations of the sample in 30° increments through a full 360° rotation.

4.3 Conclusions

In this chapter, we employ triangular templates to direct the assembly of Au nanorods along the edges of an equilateral triangle. Using spatially-resolved darkfield scattering spectroscopy in concert with numerical simulations, we characterize the collective surface plasmon resonances of individual one-, two-, and three-rod assemblies. The Au NR assemblies exhibit rotation- and polarization-dependent hybridized plasmon modes, which are sensitive to variations in nanorod size, position, and orientation. Ongoing work will clarify the interplay of electric and magnetic dipole plasmon resonances in determining the overall plasmonic response of the Au nanorod trimers. The nanorod trimers display planar geometric chirality, and preliminary measurements of circular differential scattering suggest that the structural chirality is accompanied by a

significant chiroptical response. Continuing work will correlate the structural and spectral chiral properties of the nanorod trimers. Our results represent an important step in realizing and characterizing metamaterial assemblies based on anisotropic plasmonic building blocks, with implications for optical magnetic field enhancement and chiral plasmonics.

4.4 Methods

4.4.1 Au Nanorod Synthesis

The Au NRs are synthesized by a seeded growth method according to a previously reported recipe.[123] The Au NRs have an average length of 110 ± 8 nm and diameter of 22 ± 3 nm (aspect ratio 5:1) as measured by TEM.

4.4.2 Template Fabrication and Nanocrystal Assembly

Double-side-polished germanium wafers (undoped, 250 μm thickness, Wafer World Inc.) serve as the substrate. A germanium substrate is chosen instead of silicon to avoid scattering artifacts in the near-infrared (NIR) that can arise with silicon due to its NIR transparency. After sonication in acetone and rinsing with acetone and isopropyl alcohol (IPA), the wafers are cleaned using an O_2 plasma (Gatan Solarus) for 5 min. Then, 250 nm of SiO_2 is deposited on the wafers by plasma-enhanced chemical vapor deposition (PECVD, Oxford Plasmalab System 100). The SiO_2 thickness is confirmed using spectral reflectance measurements (Filmetrics F40). Poly(methyl methacrylate) (PMMA) positive e-beam resist (MicroChem) is spun onto the substrate in two layers: (1)

495K molecular weight (MW) PMMA (1% solids in anisole) is spun at 4000 rpm for 90 sec followed by a 4 min bake at 180 ℃, and then (2) 950K MW PMMA (1% solids in anisole) is spun at 4000 rpm for 90 sec followed by a 4 min bake at 180 ℃. The total PMMA thickness measured by spectral reflectance is 55 nm. The template pattern is written by electron-beam lithography (Elionix ELS-7500EX) using a 50 kV accelerating voltage and a 50 pA beam current. The resist is developed by a 90-second immersion in a solution of methyl isobutyl ketone (MIBK) and IPA of a 1:3 ratio, followed by rinsing with IPA. An 8-second O_2 plasma descum treatment is then performed, resulting in a final PMMA thickness of 43 nm. Au NRs are assembled using the custom-built capillary assembly apparatus described above (Figure 3-4a). An aqueous dispersion of Au NRs is dispensed between the substrate and a fixed glass slide. The substrate is translated by a motorized linear stage (New Focus Picomotor) at a rate of 8 μm/sec, and capillary forces at the meniscus direct the assembly of NRs into the template features. The entire assembly apparatus is enclosed in a humidity-controlled environment, and the substrate temperature is regulated by a water-cooled stage monitored by a thermocouple. During assembly the substrate temperature is 25 ℃, and the ambient dew point is maintained at 10 ℃ through the controlled introduction of dry nitrogen. Following assembly, resist liftoff is performed by soaking in acetone.

4.4.3 Structural and Optical Measurements

Scanning electron microscopy is performed using a JEOL 7500F HRSEM and an FEI Quanta 600 ESEM operating at 10 kV. Transmission electron microscopy is

performed on a JEOL JEM-1400 TEM operating at 120 kV. Reflection-mode darkfield scattering is collected using a modified Olympus BX51 microscope. White light from a 150-W quartz tungsten halogen lamp with an aluminum reflector is routed to the microscope through an optical fiber bundle. After collimation by a plano-convex lens, the light passes through a rotatable broad-band linear polarizer before being refocused on the sample surface by another lens. For measurements of circular differential scattering, a broad-band quarter wave plate (Thorlabs SAQWP05M-1700) is inserted after the linear polarizer, and the fast axis of the wave plate is aligned at ± 45° to the plane of linear polarization to establish left-circular and right-circular polarization. The illumination spot is projected across the entire field of view of the collection objective. The elevation angle of the illumination is approximately 10° above horizontal. The azimuthal angle of the illumination with respect to the sample can be varied by rotating the sample on a rotation–translation stage (Olympus U-SRP, U-FMP). Scattered light from the sample is collected by a NIR-optimized objective lens (Olympus LCPLN50XIR, NA 0.65). The indicated illumination and collection geometry establishes a darkfield configuration where direct reflection of the incident light is outside the collection cone of the objective. The scattered light is routed by a 100-μm-core optical fiber to the final stage of a Princeton Instruments Tri-Vista 555 spectrometer equipped with a PIXIS-256E Si 2D array detector and an OMA-V InGaAs linear array detector for visible and NIR measurement, respectively. Each scattering spectrum is normalized by the spectral profile

of the illumination source, followed by subtraction of baseline scattering from a blank area of the substrate containing no Au NRs.

4.4.4 Simulations

The numerical simulations are performed using the frequency domain solver of the commercial software COMSOL Multiphysics®. Gold is used for the nanoparticles with a dispersive complex permittivity following Johnson and Christy's experimental data.[187] They are placed within a dielectric cube of relative permittivity $\varepsilon_r = 1.5$ with lateral dimensions 220 nm. The nanoparticles are illuminated with an oblique incident wave (under different polarizations) with an elevation angle of 10 degrees above the horizontal, and the whole structure (nanoparticle + dielectric) is placed within a sphere covered with a perfect matched layer to avoid undesirable reflections. Note that the substrate is not directly introduced in the numerical calculations, which can produce a frequency shift of the resonances. However, as reported by Vernon *et al.*,[186] its influence is taken into account by immersing the nanoparticles within a dielectric medium. For each polarization (p-, s-, LCP, and RCP) different simulations are performed and the scattering cross-section is calculated as:

$$Scattering = \frac{1}{I_0}\oint_A \mathrm{Re}\{\boldsymbol{E_s} \times \boldsymbol{H_s^*}\} \cdot \hat{\boldsymbol{n}} dS \qquad \text{(Eq. 4-2)}$$

where $I_0 = |E_0|^2/(2\eta_0)$ is the incident power density and $\boldsymbol{E_s}$ and $\boldsymbol{H_s}$ are the scattered electric and magnetic fields, respectively.

CHAPTER 5. EXTENSIONS AND FUTURE DIRECTIONS

5.1 Introduction

The discussion in the preceding chapters highlights the versatility of the templated assembly approach for forming well-defined arrangements of nanocrystals that have a variety of different shapes and compositions. The spatially-resolved spectroscopy measurements detailed above offer a suite of techniques to probe the optical response of individual assemblies, elucidating the physics of the interparticle coupling in both homogeneous and heterogeneous plasmonic systems. This chapter presents several extensions of this assembly and measurement scheme that take advantage of opportunities to explore additional materials systems and more intricate assembly geometries. For example, by incorporating new materials, such as phase-change materials and dielectric "dopants," and by building arrangements in three dimensions or with fractal-like self-similarity, a greater range of functional nanostructures can be realized and characterized.

5.2 Engineering Plasmon Resonances by Tailoring Nanocrystal Separation

The strength of the interaction between adjacent plasmonic structures is highly dependent on the interparticle spacing. In fact, the well-defined relation between the spatial separation of the particles and the spectral shift resulting from the interparticle coupling has motivated the concept of a "plasmon ruler" for indicating nanometer-scale distances through optical means.[146] Plasmonic nanoparticles could then be used, for

example, as probes to report distances as they interact within biological systems. A full understanding and implementation of plasmonic systems with varied interparticle spacings requires knowledge of the behavior not only of particle pairs, but also of more extended 1D,[29,171] 2D,[144,145,149] and 3D[180,206] assemblies and for particles of various shapes[203] and sizes.[165] Because template-assisted self-assembly can be generalized to numerous nanocrystal types, it may prove a valuable strategy for further exploring how to engineer the optical properties of a nanocrystal assembly by tailoring the interparticle separation.

As an example, nanocrystals can be prepared with the same metallic core but different surface coatings. Figure 5-1 illustrates 55 nm Au nanocrystals with either cetyltrimethylammonium bromide (CTAB) surfactant or with an SiO_2 coating. While a bilayer of CTAB is expected to be around 3.2 nm in thickness,[207] here the SiO_2 coating is approximately 12 nm thick. Therefore, assemblies of nanocrystals having each of the two coating types would have a significantly different magnitude of interparticle coupling. Assemblies formed using the CTAB-coated nanocrystals are discussed in Chapter 3, and assemblies using the SiO_2-coated nanocrystals (denoted as Au@SiO_2) are described below. Future work could make a direct comparison between the two systems for a given set of geometries, investigating the impact of the interparticle spacing on the collective optical response.

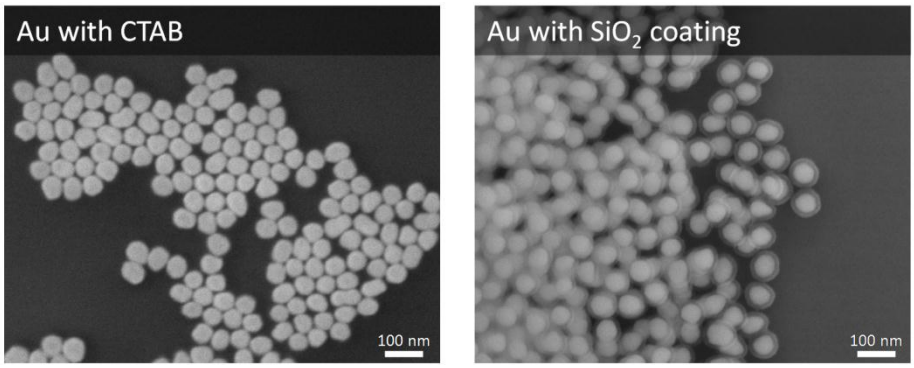

Figure 5-1. Scanning electron microscopy (SEM) images of Au nanocrystals with the same size (55 nm diameter) but different surface coatings: CTAB (left) and SiO_2 (right).

Additional experiments could include assembling nanocrystals prepared with several different values for the SiO_2 thickness. Another alternative is to use dendritic ligands to precisely engineer the interparticle spacing and optical properties, as was demonstrated in ensemble measurements of Au spheres.[208] While these strategies involve starting from several distinct populations of nanocrystals with different coatings, it is also possible to tune the coating—and therefore the interparticle separation—after the assembly has occurred. Motivated by reports of post-assembly ligand exchange strategies,[209,210] we envision assembling nanocrystals into templates and then subsequently displacing and replacing the original ligands with new ligands of varying sizes. The interparticle spacing could also be tuned by ligand desorption upon light irradiation.[211] Finally, the role of solvent annealing[212] in introducing subtle adjustments of nanocrystal arrangement and spacing can be explored.

5.3 Nanocrystal Assembly at Polygon Vertices and Edges

Chapter 3 describes the use of polygonal templates to direct the self-assembly of hexagonally close-packed nanocrystal oligomers. In these structures, the aim is to completely fill the interior space of the template to form a densely assembled cluster. However, it is also possible to realize "hollow" 2D oligomers where the nanocrystals only assemble at the periphery of the template.[163] Figure 5-2 presents images of $Au@SiO_2$ nanocrystals assembled at the vertices and edges of polygonal templates having 2-, 3-, 4-, 5-, and 6-fold rotational symmetries. The preference for vertex *versus* edge sites can be tuned to some extent by the shape of the template (Figure 5-3). While "regular polygons" suggest a preference for edge-directed nanocrystal assembly, "star polygons" suggest a preference for assembly at the polygon vertices. By varying the sharpness of the vertices (Figure 5-3), the transition from edge preference to vertex preference could be investigated in more detail. Templates of the same shape but different size can also be used for assembly (Figure 5-4).

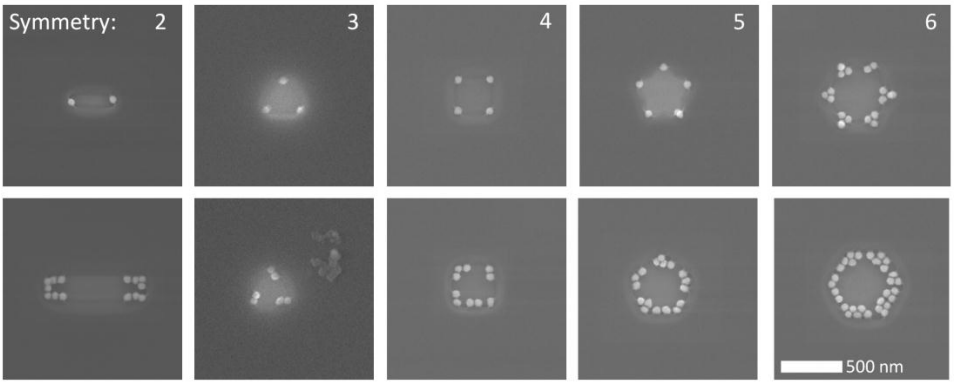

Figure 5-2. SEM images of $Au@SiO_2$ nanocrystals assembled at the vertices (top row) and edges (bottom row) of templates with 2-, 3-, 4-, 5-, and 6-fold rotational symmetries.

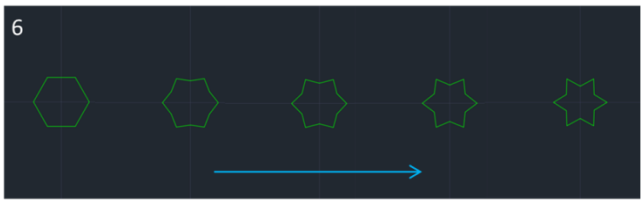

Figure 5-3. Template designs for six-fold symmetric polygons ranging from a “regular polygon” (left) to a “star polygon” (right).

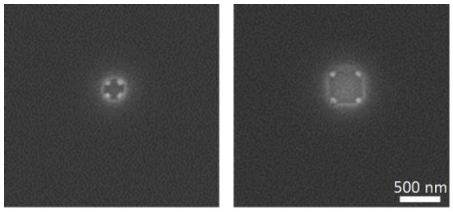

Figure 5-4. SEM images of nanocrystals assembled at the vertices of square templates having two different sizes.

Assemblies where the nanocrystals are arranged at the periphery of polygonal templates may exhibit interesting optical properties, especially magnetic plasmon resonances.[213] For the vertex-assembled structures, the polygonal templates act to specify the number and spacing of the nanocrystals making up an overall ring-like arrangement. For the edge-assembled structures, the nanocrystals arrange in rings that are polygonal rather than circular. Varying the size and symmetry of these arrangements may have important implications for the nature of the magnetic plasmon response.

The 6-fold vertex-assembled structure in the upper right of Figure 5-2 also exemplifies the possibility of directing the nanocrystal assembly on multiple length scales. This structure consists of local units of nanocrystal trimers that are themselves organized into a larger 6-fold-symmetric superstructure. Future work could explore the strength of plasmonic interactions both within and among the individual trimer units, and

the role of overall symmetry and symmetry-breaking. The use of templates enables access to non-space-filling symmetries (*e.g.* 5-fold, Figure 5-5) that are less frequently encountered in self-assembly experiments,[214] but are important unit structures for quasicrystalline[215,216] patterns. While not space-filling for a single size of nanocrystal, 5-fold rotationally symmetric patterns can accommodate differences in size among nanocrystals, as shown in Figure 5-6. Here, the central nanocrystal is noticeably smaller than the surrounding nanocrystals, leading the cluster to adopt a pentagonal type of arrangement. Assembling two populations of nanocrystals intentionally having different sizes into 5-fold-symmetric templates may promote the formation of such arrangements.

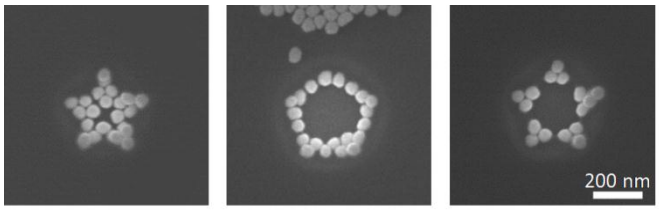

Figure 5-5. SEM images of Au nanocrystals assembled in 5-fold symmetric templates.

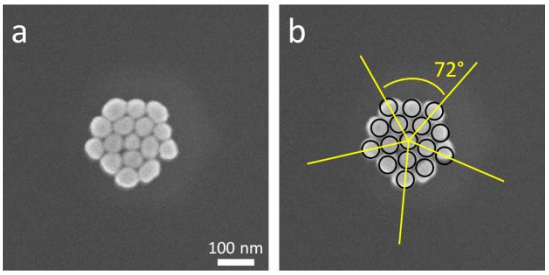

Figure 5-6. (a) SEM image of nanocrystals assembled into a close-packed structure with approximately 5-fold rotational symmetry, enabled by the small size of the central nanocrystal. (b) Overlay of an ideal 5-fold symmetric pattern.

5.4 Assembly of Plasmonic Nanocrystals around Post Templates

In addition to assembling within templates defined as areas of low topography in the resist layer, nanocrystals can also be directed to assemble around elevated topographic features such as posts.[14,217] Figure 5-7 illustrates the assembly of Au@SiO_2 nanocrystals around poly(methyl methacrylate) (PMMA) posts. The density and width of the assembled ring structures can vary from nearly isolated nanocrystals to single-layer and double-layer rings. As mentioned in Section 5.3, rings of plasmonic nanocrystals can support magnetic plasmon resonances.[213] An incomplete ring of nanocrystals could also serve as a nanocrystal realization of a split-ring resonator,[218,219] which has served as an archetypical unit in metamaterial design. By varying the size of the template post, the number of nanocrystals constituting the assembly can be tuned, and the discrete nature of the individual nanocrystals could have important implications on the collective optical response as the number of nanocrystals becomes small. While the example shown here uses a template composed of the electron-beam lithography resist PMMA, the posts could be formed from different materials to introduce an interaction with the plasmonic ring structure. For example, posts of a magnetically responsive material may couple with the magnetic plasmon resonance of the nanocrystal ring. An additional extension is to combine the concepts of elevated and sunken topographical features to form structures such as the annular template pictured in Figure 5-8, which can be viewed as a post within a larger circular template.

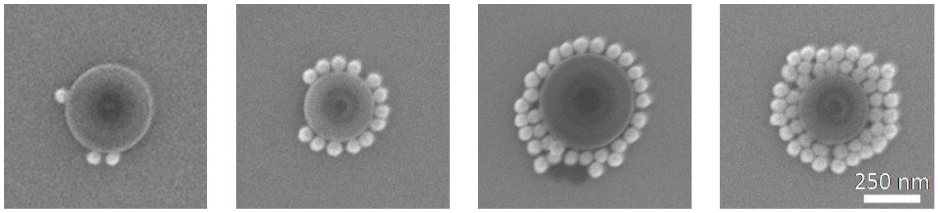

Figure 5-7. SEM images of Au@SiO_2 nanocrystals assembled around PMMA post templates.

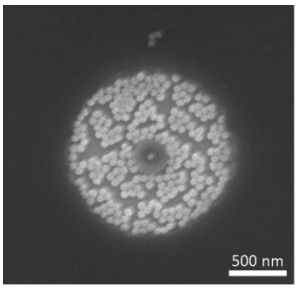

Figure 5-8. SEM image of Au@SiO_2 nanocrystals assembled within an annular template.

5.5 Three-Dimensional Plasmonic Nanocrystal Clusters

A significant advantage of template-assisted self-assembly compared to direct lithographic patterning is the ability to define three-dimensional structures based on the packing of multiple layers of nanocrystals. This approach can overcome the necessity for multiple aligned lithography steps, where nanometer-scale registry between the layers can be challenging to achieve. In addition, the shape of the nanocrystal components used for templated assembly can be engineered in 3D through chemical synthesis methods, in contrast to the largely 2D shape control for the layers of an aligned lithography process.

Figure 5-9 illustrates the formation of a 3D nanocrystal structure using templated assembly, where the nanocrystals are positioned at the vertices of a tetrahedron. Here, the template outline is circular, but two layers of nanocrystals have assembled within the templates, yielding 3D clusters. Figure 5-9b shows two orientations of such a structure,

either sitting on its dimer edge or on its trimer base. This nanocrystal arrangement is expected to be the smallest cluster to exhibit completely 3D isotropic optical properties, therefore representing a structure of fundamental interest.[160] Similarly, a slightly larger cluster, where six particles are arranged at the face centers of a cube, has been proposed as the fundamental magnetic plasmon molecule,[41] offering further motivation for methods to form 3D clusters. Future directions may also include 3D clusters where one of the nanocrystals is of a different material type, which could lead to Fano interferences between electric and magnetic plasmon modes, as suggested by simulations of structural symmetry breaking in 3D tetramers.[160]

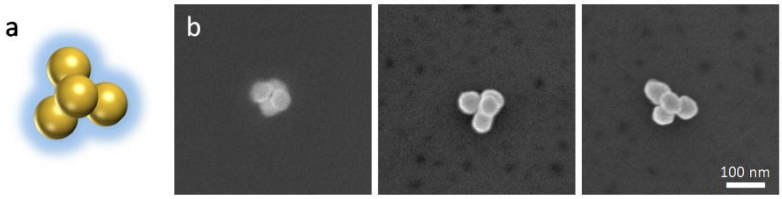

Figure 5-9. (a) Schematic and (b) SEM images of 3D tetrahedral Au nanocrystal assemblies formed through templated assembly.

5.6 Dielectric-Doped Plasmonic Oligomers

In nanocrystal assemblies, the deliberate introduction of nanocrystal impurities can be considered analogous to the concept of atomic doping in semiconductor materials.[220] The impact of the impurities on the global properties of the assembly depends on the identity and density of the nanocrystal dopants. As discussed in Chapter 3, disorder and symmetry-breaking can have a significant impact on the optical properties of plasmonic nanocrystal oligomers. While that discussion considers only positional disorder in the nanocrystal packing, compositional disorder in the form of nanocrystal

doping is likely to also have a strong influence on the optical response. To explore these effects in more detail, we propose the substitutional doping of dielectric nanoparticles within oligomers composed of plasmonic metal nanocrystals.

The optical response of a large plasmonic nanocrystal oligomer as pictured in Figure 5-10a approximates that of an infinite array of nanocrystals (see Chapter 3). However, the introduction of a certain concentration of dielectric dopants would be expected to perturb this response. By measuring the spectra of oligomers with dopant nanocrystals assembled in specific concentrations and locations (*e.g.* Figure 5-10b), the impact on the overall plasmonic modes of the oligomer can be investigated and the density of defects necessary for "destabilizing" the quasi-infinite optical response ascertained.

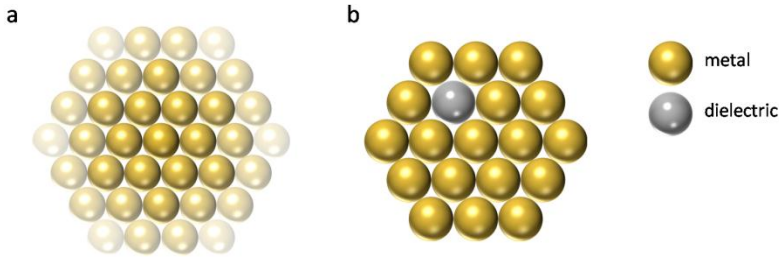

Figure 5-10. (a) Schematic of a large nanocrystal oligomer, whose optical response approximates that of an infinite array of nanocrystals. (b) Schematic of introducing a dielectric nanoparticle "dopant" into a metal nanocrystal oligomer.

As a basic experimental proof-of-concept, Figure 5-11 presents an SEM image of Au nanocrystals and SiO_2 nanoparticles having similar sizes that are co-assembled randomly on an unstructured substrate. Groupings of particles are visible in which the two types of materials appear to have assembled within the same lattice. Future work

entails verifying the suitability of assembling SiO_2 nanoparticles within templates and then assembling SiO_2-doped Au nanocrystal oligomers for optical characterization.

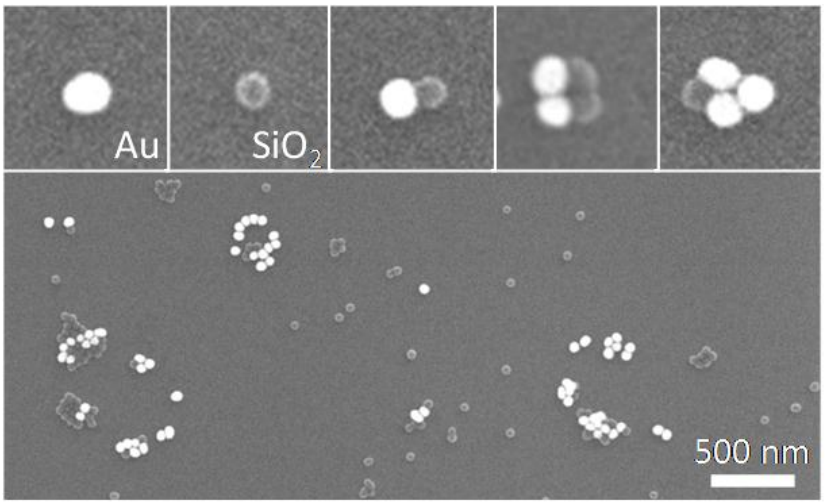

Figure 5-11. SEM image of a random co-assembly of Au nanocrystals (bright) and SiO_2 nanoparticles (gray) on an unstructured substrate. Insets show magnified regions.

5.7 Heterostructures of Plasmonic and Phase-Change Materials

The ability to design materials whose optical properties respond to external stimuli such as light, electricity, and heat represents an ongoing goal of metamaterials research.[221] One way to modulate the optical response is to take advantage of the metal–insulator transition in phase-change materials such as vanadium dioxide (VO_2) and the difference in optical properties between the two phases. For example, VO_2 has been applied as a thin film to modify the response of a plasmonic metasurface patterned with split-ring resonators.[222] The VO_2 itself can also be patterned to realize tunable metasurfaces,[223] and size effects influence not only the wavelength of operation but also the behavior of the phase transition.[224] As anticipated theoretically,[225] VO_2 can also be

introduced between individual metal plasmonic resonators to modulate the plasmonic coupling.

We propose to use template-assisted self-assembly to form heterostructures consisting of nanostructured VO_2 and plasmonic nanocrystals. As described in Section 5.4, raised posts can function as sites to direct the assembly of nanocrystal rings. We therefore generate posts of VO_2 that serve a dual role: first to template nanocrystal assembly and then to modulate the response of the plasmonic nanocrystals as the VO_2 undergoes its reversible phase transition. Following the procedure of Paik *et al.*,[223] we first synthesize VO_x nanocrystals, which are assembled and then subsequently transformed into VO_2 through rapid thermal annealing. Figure 5-12 presents an image of pillars of VO_x nanocrystals that are formed by assembly of the nanocrystals into circular templates followed by resist liftoff. The height of the pillars as determined by atomic force microscopy (AFM) is approximately 200 nm. Upon rapid thermal annealing for 5 minutes at 500 °C to convert the VO_x into VO_2, the individual pillars spread out laterally while maintaining the original array pitch, as shown in Figure 5-13. AFM analysis of the annealed pillars indicates that the lateral expansion is accompanied by a height reduction from 200 nm to approximately 20 nm (Figure 5-14).

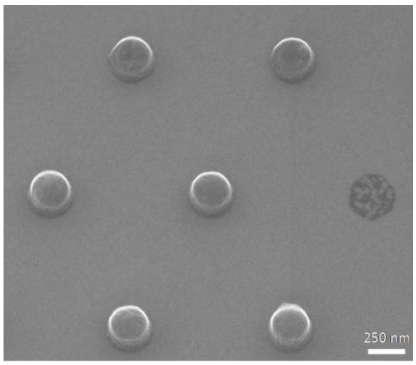

Figure 5-12. SEM image of pillars formed through templated assembly of VO_x nanocrystals before rapid thermal annealing. Sample is tilted by 20°.

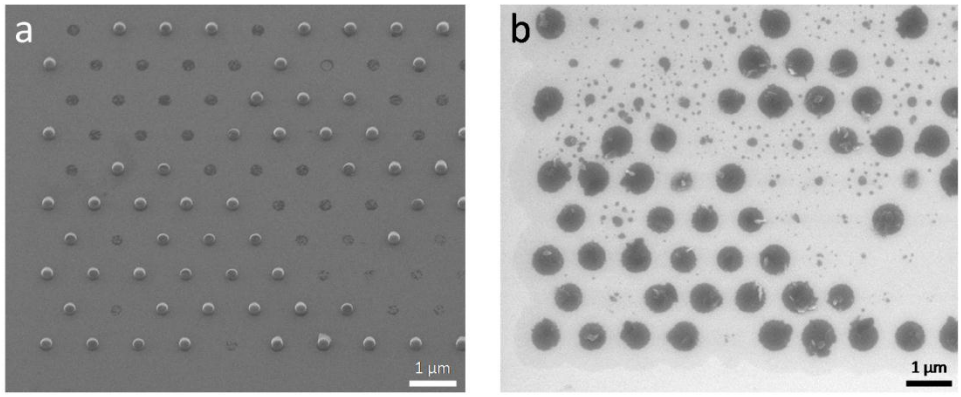

Figure 5-13. SEM image of pillars formed through templated assembly of VO_x nanocrystals (a) before and (b) after rapid thermal annealing. Sample in (a) is tilted by 30°.

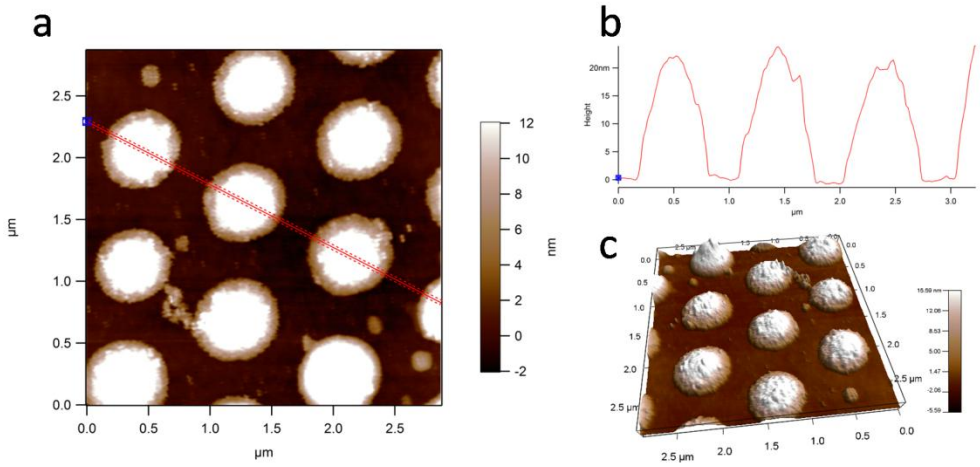

Figure 5-14. (a) Representative AFM image of VO_2 pillars after rapid thermal annealing. (b) Height profile across the line indicated in (a) showing a height of approximately 20 nm. (c) 3D rendering of the pillar structures.

The SEM image of Figure 5-13b indicates that the spreading of the pillars upon annealing also introduces polydispersity in the pillar diameters, which may be detrimental to achieving uniform optical properties. One strategy to reduce the uneven spreading of the pillars may be to perform the annealing while the pillars are confined in a template. While the temperature of the annealing (500 °C) is too high to be compatible with the PMMA resist, circular patterns in the resist can be transferred into an alternative material using reactive ion etching (RIE). As a simple test, RIE was performed on a PMMA template to etch the pattern into the underlying SiO_2 layer thermally grown on the silicon wafer substrate. Figure 5-15a depicts the result of assembling the VO_x nanocrystals in the etched template. Two types of structures are visible, with the features in the top left and bottom right likely showing pillars raised above the top of the SiO_2 surface that were assembled in the PMMA layer before liftoff. The other features likely show VO_x

nanocrystals assembled within the etched regions beneath the SiO_2 surface. Following rapid thermal annealing (Figure 5-15b), the VO_2 is confined within the templated regions, as desired, rather than spread out laterally. If the templates are only partially filled with VO_2, the template sites then offer topographical relief to direct the assembly of additional nanocrystals above the VO_2 layer. If raised pillars of VO_2 as initially described are desired, the material that is etched to form the templates should be designed to be a sacrificial layer that can be removed by a method that does not harm the confined VO_2 structures, with the requirement that the sacrificial layer material must remain compatible with the 500 °C thermal annealing process.

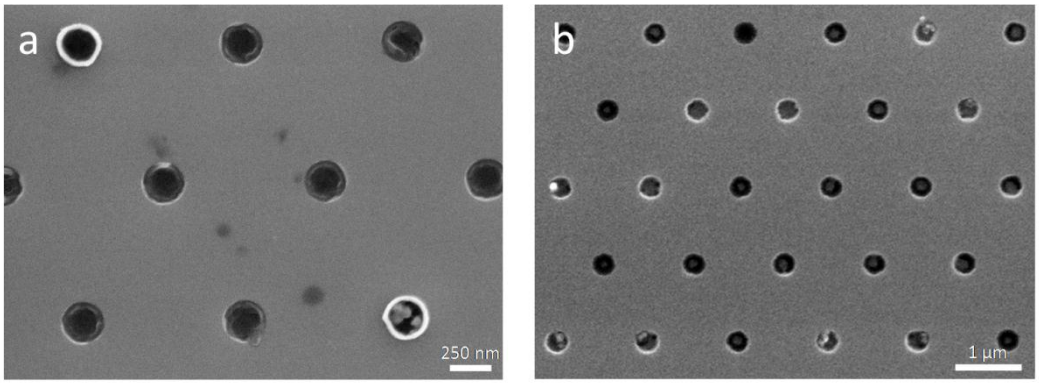

Figure 5-15. SEM images of pillars formed through assembly of VO_x nanocrystals into templates etched into SiO_2 using a PMMA mask (a) before and (b) after rapid thermal annealing.

Paik *et al.* reported that VO_2 nanostructures of this size have plasmon resonances in the 1500–2000 nm spectral range.[223] Compatible plasmonic materials for co-assembly that would interact with the VO_2 by virtue of resonances in a similar spectral range could therefore include indium-doped cadmium oxide (ICO).[226] Figure 5-16a shows a solution-phase absorption spectrum of ICO nanocrystals indicating a plasmon resonance at around

1560 nm, within the spectral range of the VO_2 resonances. The relative narrowness of the ICO resonance compared to the broad resonances reported for VO_2 pillars[223] could be favorable for the generation of Fano interference between the ICO and the VO_2. A demonstration of the assembly of ICO nanocrystals is given in Figure 5-16b, which shows a PMMA pillar decorated with ICO. Future work would optimize the size and reliable formation of VO_2 pillars for the assembly of ICO. The optical response of the coupled system could then be probed as the VO_2 phase is cycled between insulator and metal.

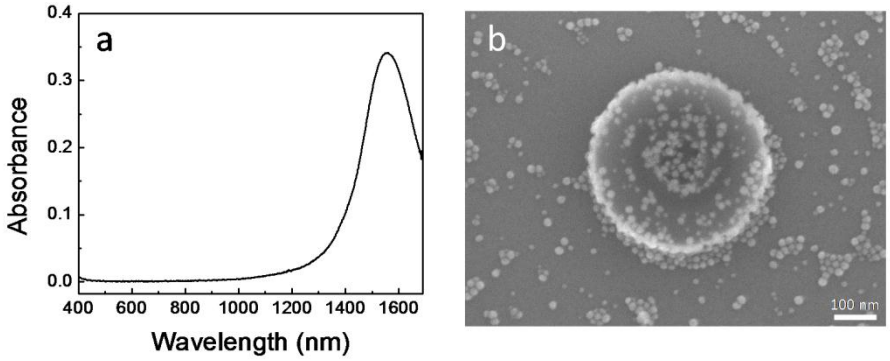

Figure 5-16. (a) Solution-phase absorption spectrum of ICO nanocrystals. (b) SEM image of a PMMA pillar decorated with ICO nanocrystals.

5.8 Fractal-Like Assembly of Two-Component Systems

Chapter 2 demonstrates the utility of shape-selective templates for forming heterostructures consisting of two different nanocrystal components. To assemble the rod–phosphor heterodimers for that study, the template design matches the outline of the desired final structure. The assembly is performed in two steps. Assembling the phosphor first before the nanorod fills the center of the template, ensuring that the remaining space

in the template is compatible only with assembling a single nanorod on either side. In a sense, the phosphor becomes part of the template, acting to refine the template shape for the rod assembly.

In this section, we extend this concept to form self-similar, or fractal-like, arrangements of multiple nanocrystals within templates where each assembly step refines the available space within the template to suit the subsequent nanocrystal assembly. The strategy is akin to the generation of fractal patterns such as the Sierpinski triangle and Apollonian gasket (Figure 5-17), in which interstices in the structure are filled with successively smaller shapes. As an initial example, Figure 5-18 illustrates the subsequent assembly of two different nanocrystals types into a triangular template. The first assembly step results in the oriented assembly of a $NaYF_4$:Er^{3+},Yb^{3+} nanocrystal having a hexagonal platelet morphology with face diagonal 510 nm (Figure 5-18b). The hexagonal shape of the nanocrystal creates smaller triangular regions at each of the vertices of the original triangular template. These small triangles serve as "second-generation" templates for the assembly of additional nanocrystals, in this case Au@SiO_2 spheres (Figure 5-18c).

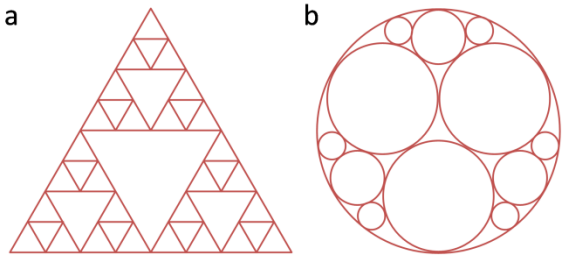

Figure 5-17. Fractal geometries. (a) Sierpinski triangle. (b) Apollonian gasket.

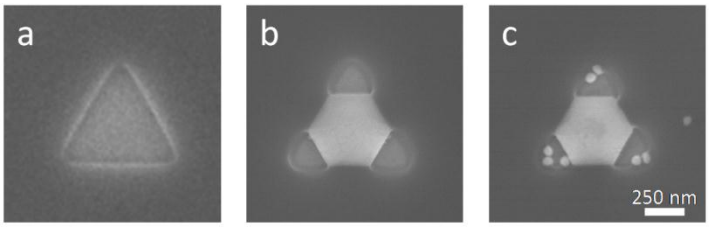

Figure 5-18. SEM images of (a) an empty triangular template, (b) a single 510 nm hexagonal $NaYF_4$:Er^{3+},Yb^{3+} nanocrystal assembled in a triangular PMMA template, and (c) Au@SiO_2 nanocrystals co-assembled with a $NaYF_4$:Er^{3+},Yb^{3+} nanocrystal.

To improve the size complementarity of the two nanocrystal components with a triangular template, the size of the hexagonal $NaYF_4$ nanoplates is reduced to 265 nm. With this size, each of the second-generation templates is optimal for accepting a single Au@SiO_2 nanocrystal. As demonstrated in Figure 5-19, structures with one, two, or three filled vertices can be assembled. Additional structures observed to form include those with two nanocrystals at each vertex (Figure 5-20a) and well-ordered triangles of Au@SiO_2 when no nanophosphor is present (Figure 5-20b).

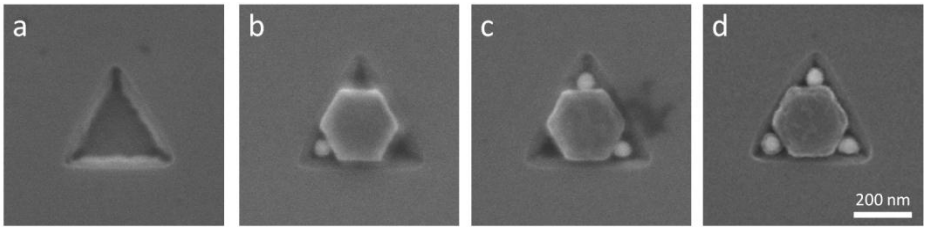

Figure 5-19. (a) SEM image of an empty triangular template etched in SiO_2. (b-d) SEM images of the self-similar filling of a triangular template with a 265 nm hexagonal $NaYF_4$:Er^{3+},Yb^{3+} nanocrystal and (b) one, (c) two, and (d) three Au@SiO_2 nanocrystals.

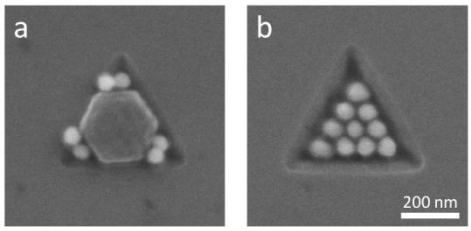

Figure 5-20. SEM images of (a) the filling of a triangular template etched in SiO_2 with a $NaYF_4$:Er^{3+},Yb^{3+} nanocrystal and two Au@SiO_2 nanocrystals at each vertex and (b) filling of a triangular template with a triangular arrangement of Au@SiO_2 nanocrystals.

The Au@SiO_2 nanocrystals support a surface plasmon resonance at approximately 545 nm, making them ideal for enhancing the photoluminescence from the 545 nm emission band (see Figure 2-1b) of the nanophosphors. Furthermore, the 12 nm SiO_2 coating of the Au nanocrystals introduces a controlled spacing from the nanophosphor, which limits the potential for quenching of the luminescence. Future work entails measuring and comparing the magnitude of enhancement for the structures with one, two, and three Au@SiO_2 nanocrystals using the spatially-resolved spectroscopy techniques described in Chapter 2. In contrast to the rod–phosphor heterodimer of Chapter 2, where the nanorod plasmon resonance was tuned to magnify the phosphor excitation, the hierarchical nanocrystal–phosphor structure of this section targets an enhancement of the phosphor emission. An understanding of nanocrystal assembly strategies to enhance both excitation and emission processes in luminescent systems underpins the successful deployment of plasmonic enhancement strategies for real-world applications.

The self-similar filling of templates with nanocrystals of different sizes can also be applied to achieve novel arrangements of two different plasmonic components. Figure

5-21 presents schematics of several target structures made up of spheres with sizes 55 nm and 20 nm (size ratio 2.75:1) as well as the template outlines proposed to achieve them. An SEM image of Au nanocrystals with these two sizes is shown in Figure 5-22a. Preliminary examples of the assembly of the nanocrystals into circular templates are given in Figure 5-22b–e. With future work to refine the sizes and shapes of the templates, the target heterostructures can be assembled and their collective plasmon resonances probed through darkfield scattering spectroscopy as described in Chapter 3. The symmetry-breaking induced by utilizing two nanocrystal sizes is likely to promote unique optical responses such as Fano resonances.[227] Future experiments could also introduce two different material compositions for the two differently sized nanocrystals, which would offer an additional means for tuning the collective modes of the hierarchical structures.[228–230] Adding a third nanocrystal type of smaller size may impart additional properties such as enhanced nonlinear circular dichroism.[231]

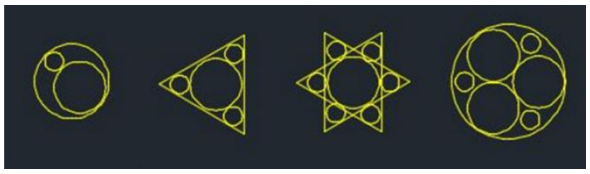

Figure 5-21. Schematic of the self-similar filling of templates with spheres having a size ratio 2.75:1.

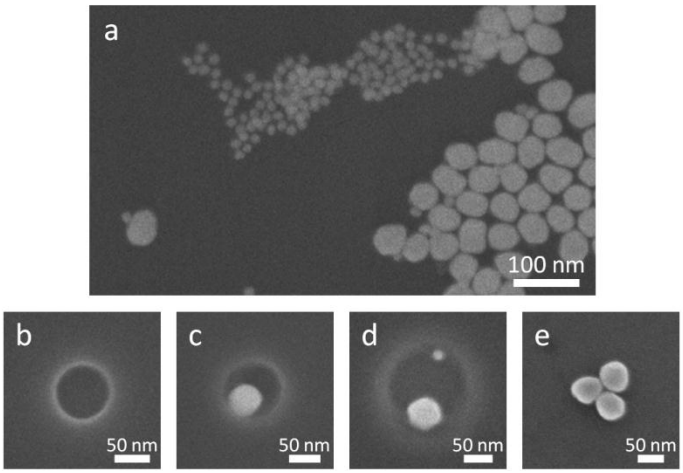

Figure 5-22. SEM images of (a) 55 nm and 20 nm Au nanocrystals, (b) an empty circular template, (c) a single 55 nm Au nanocrystal assembled in a template, (d) a 55 nm and a 20 nm Au nanocrystal co-assembled in a template, and (e) a trimer of 55 nm Au nanocrystals. The structure in (e) is shown after resist liftoff.

5.9 Assembly Yield Optimization

Maximizing the yield of successfully assembling the various structures described throughout this chapter requires an understanding of the experimental parameters that can be tuned to influence assembly. Figure 5-23 highlights several of these factors, which include substrate velocity, template depth, surface chemistry, nanocrystal concentration, and evaporation rate. This section will explore aspects of each of these factors. While the discussion focuses on the capillary assembly method, we note that the "squeegee method" described in Section 2.4.2 can also be effective for nanocrystal assembly. A comparison of assembly methods is presented in Figure 5-24. The manual squeegee method, in which the flexible wiper in direct contact with the substrate is translated by hand to draw the nanocrystal solution across the substrate, offers the advantage of ease of use and low equipment requirements. It is especially suited to nanocrystal solutions with

a fast evaporation rate. However, performing the assembly manually is subject to user variability in translation velocity, angle of application, and downward pressure exerted. To reduce variability, the flexible wiper can be mounted to the mechanized capillary assembly apparatus, enabling a "mechanized squeegee method" (Figure 5-24) where the velocity, angle, and pressure of the wiper can be specified reproducibly. Future work entails optimizing these parameters for attaining reliable, high-yield assembly of nanocrystals, as well as further comparing the suitability of choosing the squeegee method *versus* capillary assembly for a given application.

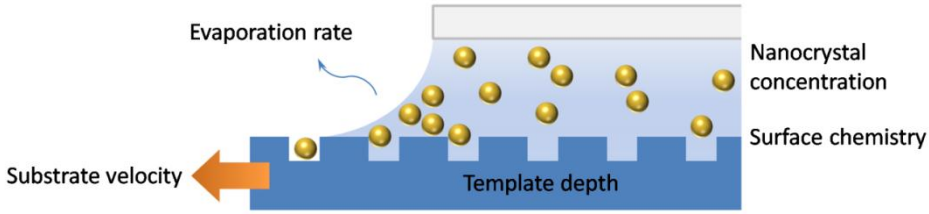

Figure 5-23. Schematic illustrating several of the factors influencing the performance of template-assisted self-assembly.

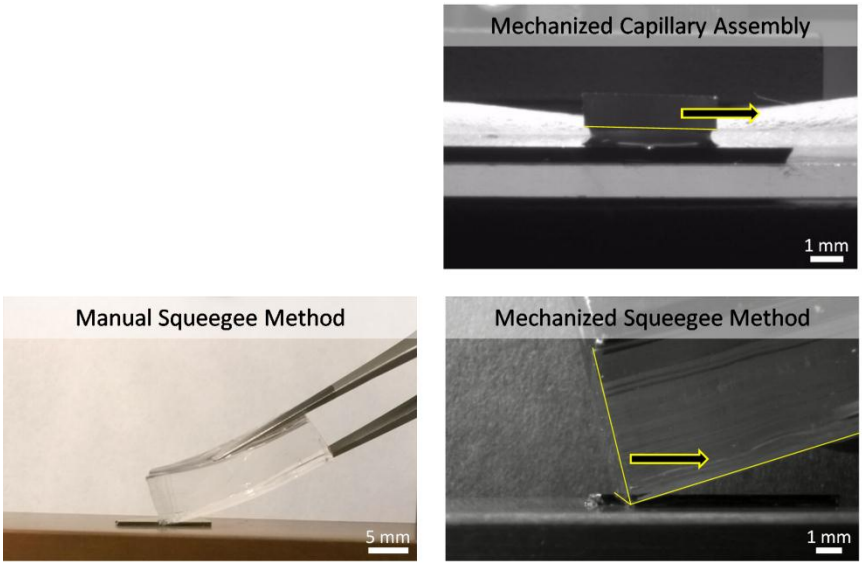

Figure 5-24. Side-view photographs of three different nanocrystal assembly methods.

When performing capillary assembly, the rate of substrate translation is an important factor in determining assembly yield.[232] Figure 5-25a presents the estimated yield for a series of assemblies with different substrate velocities. Here, in calculating yield a success is reported if the template site has a non-zero number of nanocrystals within. For substrate velocities less than 20 μm/s, yields of above 80% are observed, while a high velocity of 60 μm/s results in less than 20% yield. While this could suggest that a very low velocity would be desirable, for the lowest velocity studied (2 μm/s) the formation of undesirable Au nanocrystal islands non-specifically on the surface is observed (Figure 5-25b) that are not present at 8 μm/s (Figure 5-25c). For the set of conditions in this experiment, 8 μm/s is found to be a good choice for substrate velocity, but we note that a different choice may be optimal if any of the other experimental parameters (*e.g.* evaporation rate) is modified.

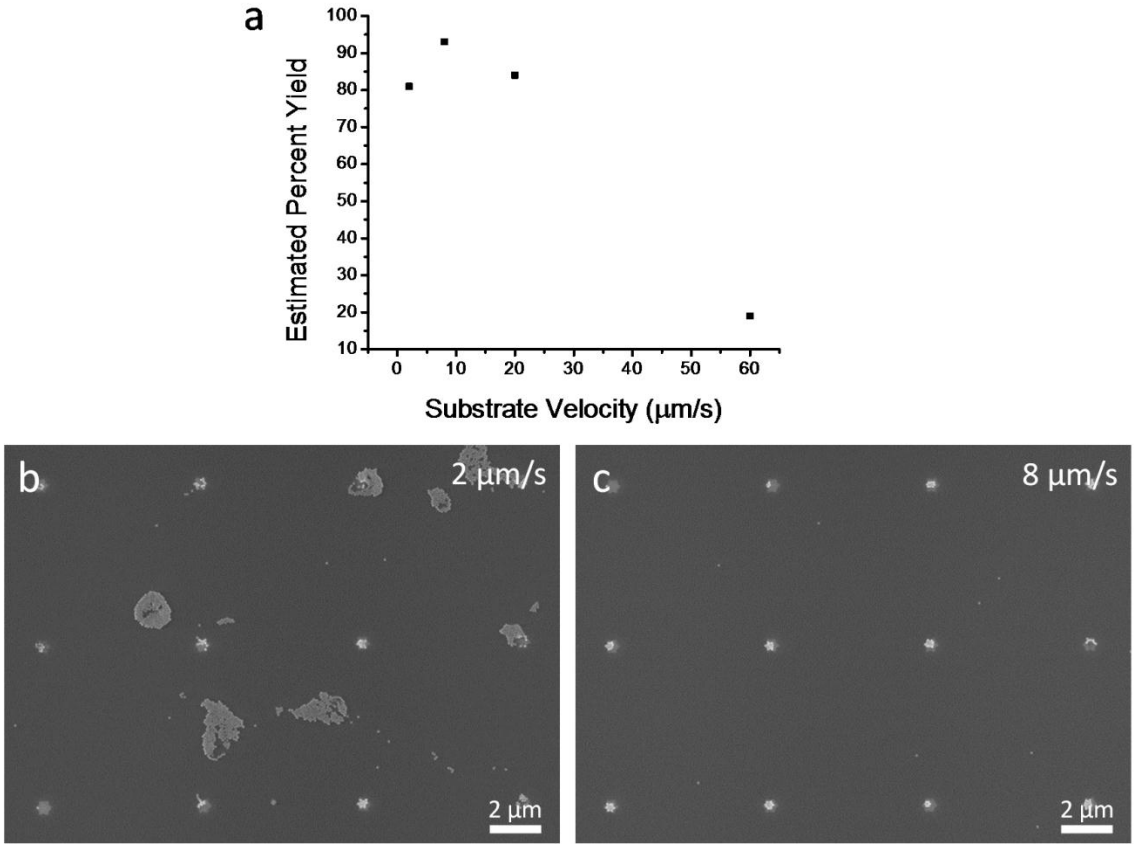

Figure 5-25. (a) Estimated percent assembly yield as a function of substrate withdrawal velocity in the capillary assembly of Au nanocrystals. (b,c) SEM images of assemblies with substrate velocities of 2 μm/s and 8 μm/s, respectively.

The depth of the topographical templates is also an important parameter for achieving high yield. Figure 5-26a suggests that the template thickness should not exceed the dimensions of the nanocrystal that is being assembled by too great a margin. The schematics of Figure 5-26b,c illustrate that for templates with too great a depth (or aspect ratio), nanocrystals would be less likely to reach the substrate at the bottom of the template. Instead the nanocrystal may be trapped on the template wall, if at all, and be removed with the resist if liftoff is performed. Conversely, template depths that are not a

significant fraction of the nanocrystal size are also not very effective at promoting assembly.[19,30]

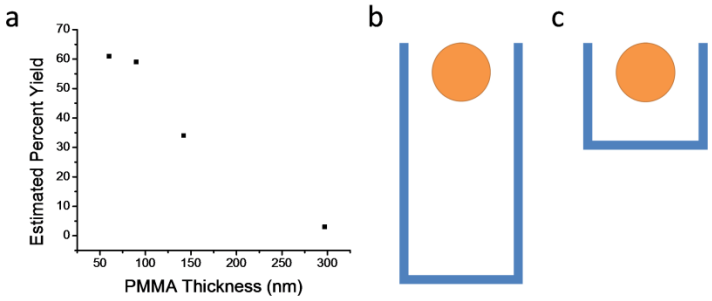

Figure 5-26. (a) Estimated percent assembly yield of Au nanocrystals with 55 nm diameter in PMMA templates of varying depths. (b,c) Schematic depictions of nanocrystals in (b) deep and (c) shallow templates.

The interaction between the nanocrystals and the templated substrate can be tuned by choosing different template and substrate materials, or through chemical functionalization. For example, as described above, patterns defined in PMMA can be transferred to the underlying wafer through reactive ion etching. Figure 5-27a,b demonstrates that the geometry of the PMMA templates is largely preserved upon etching. However, the etching process introduces significant roughness to the remaining PMMA layer (Figure 5-27c,d), which may modify the wetting properties of the template and therefore the interaction with the nanocrystal solution. Depending on the surface chemistry and electrostatic charge of the nanocrystals, different materials other than SiO_2 that interact more favorably can be chosen for the material directly beneath the resist layer. Similarly, it is possible to combine chemical templating with topographic templating by functionalizing the underlying substrate with a desired capping group. For SiO_2, silanes[233] with various chemistries could be employed. Of course, promoting ideal

nanocrystal–template interactions also can be engineered by modifying the surface chemistry of the nanocrystals themselves.

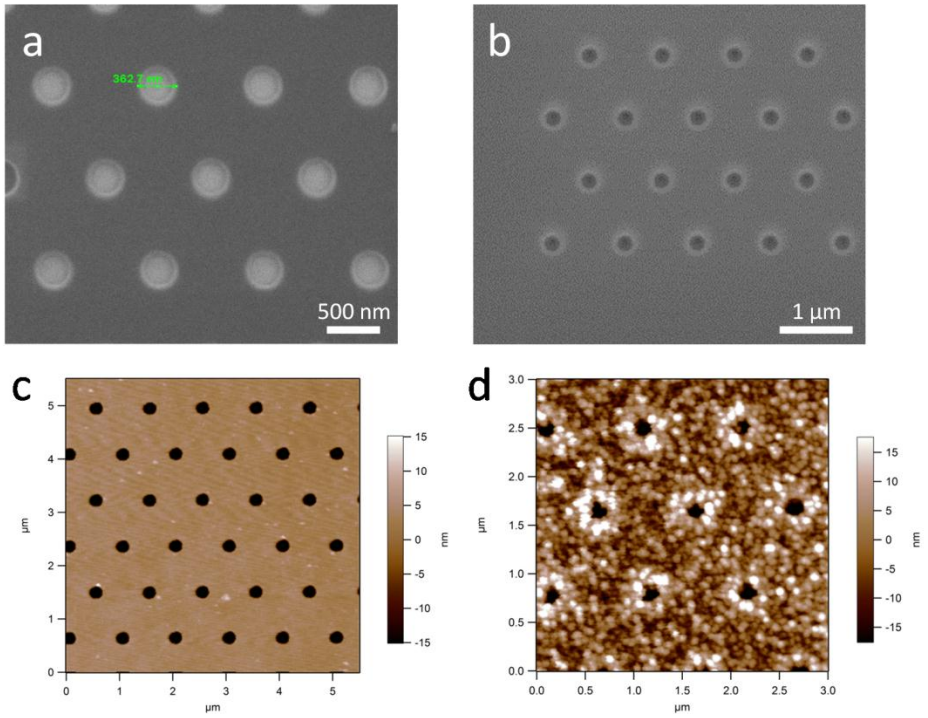

Figure 5-27. (a,b) SEM images of circular templates (a) before and (b) after reactive ion etching. (c,d) AFM images of the templates in (a) and (b), respectively. Note the increased roughness after etching.

The concentration of the nanocrystal solution can be adjusted to achieve high assembly yield while avoiding an unacceptable amount of nonspecific nanocrystal deposition. One example is shown in Figure 5-28, where assembly yield is already high but increasing the nanocrystal concentration increases slightly the average number of nanocrystals per template. For reference, an absorption spectrum of the aqueous Au nanocrystal solution having the concentration labeled as "1:5 dilution from stock" is provided in Figure 5-29. A note of caution when diluting nanocrystal solutions is that the

shelf life of the solution may be diminished compared to the concentrated solution. As illustrated in Figure 5-30, performing an assembly from a solution stored in dilute form can result in very poor yield.

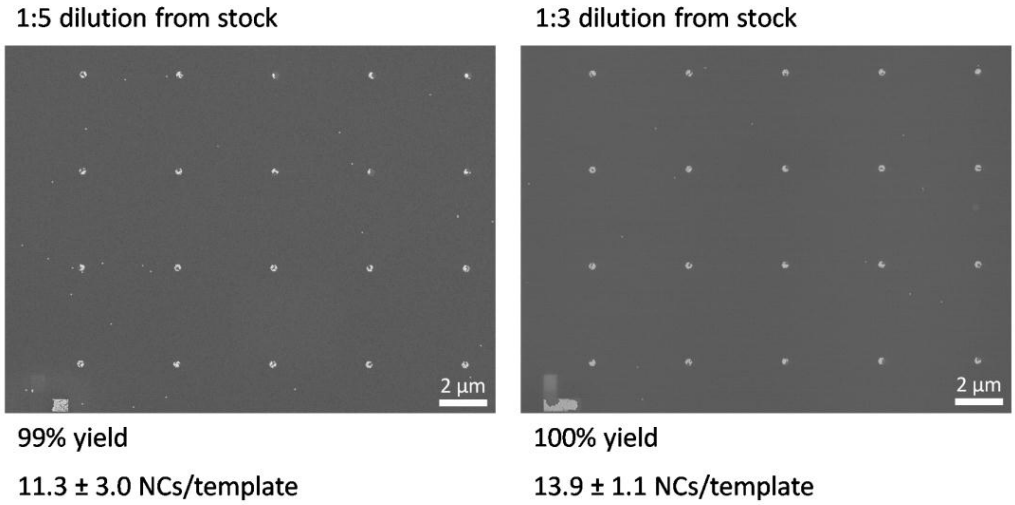

Figure 5-28. SEM images and yield statistics for assemblies performed using nanocrystal solutions with the two indicated dilution ratios.

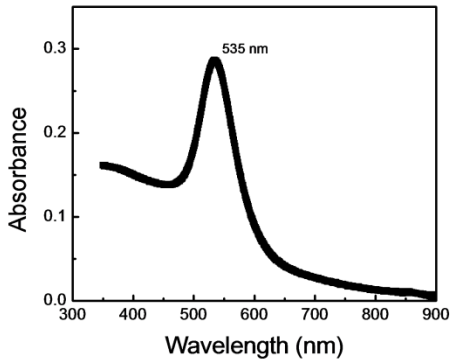

Figure 5-29. Aqueous-phase absorption spectrum of the Au nanocrystal solution referenced as "1:5 dilution from stock" in Figure 5-28.

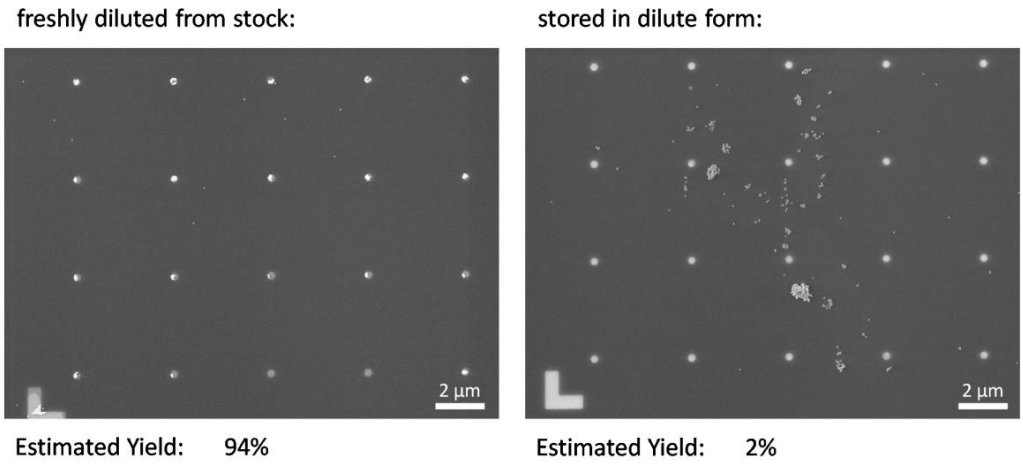

Figure 5-30. SEM images and yield statistics for assemblies using nanocrystal solutions having the same concentration, but either freshly diluted before assembly or stored in dilute form.

Because the capillary assembly method relies on the deposition of nanocrystals at the edge of the solvent meniscus, the evaporation rate of the solvent plays an important role in the assembly. Previous reports have indicated the importance of establishing an "accumulation zone" of nanocrystals at the meniscus that forms due to evaporation.[15,18] When the evaporation rate is not high enough, the local concentration of nanocrystals at the receding meniscus is not great enough to promote assembly. In our experiments the evaporation rate of aqueous nanocrystal solutions is controlled by enclosing the assembly apparatus in an environment with adjustable humidity and substrate temperature. By setting the substrate temperature to a given offset above the dew point of the ambient environment, the rate of water evaporation can be tuned. While a sufficiently high offset to form the nanocrystal accumulation zone is suggested, too high a temperature can drive the evaporation too quickly, reducing the assembly yield and leading to uniform nonspecific nanoparticle deposition over the sample surface (Figure 5-31).

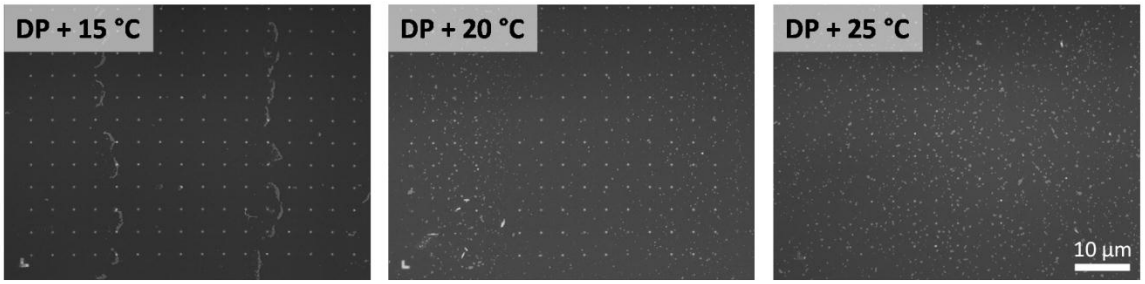

Figure 5-31. SEM images and yield statistics for assemblies prepared at the indicated temperature offsets above the dew point (DP) temperature.

The relative substrate temperature offset above the ambient dew point can be used to tune the evaporation rate, but the actual value of the temperature can also be critical in certain situations. For example, Figure 5-32 shows the result of using a stage temperature of 17 °C for the assembly of Au nanorods. The sample surface is covered with large (~30 × 60 µm) platelet structures rather than a clean deposition of Au nanorods. Energy dispersive x-ray spectroscopy (EDS) elemental mapping (Figure 5-33) indicates that the platelets are enriched in bromine and carbon, suggesting that their origin is from free cetyltrimethylammonium bromide (CTAB) surfactant in the nanorod solution. Increasing the stage temperature to 24 °C eliminated the formation of the platelets, indicating that their formation was driven by a reduced temperature. This example highlights the importance of independent stage temperature and ambient humidity control for the assembly apparatus.

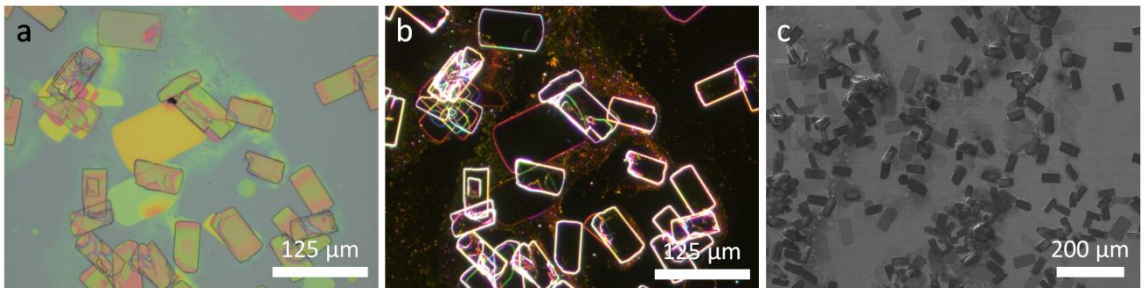

Figure 5-32. (a) Brightfield optical microscope, (b) darkfield optical microscope, and (c) scanning electron microscope images of platelets observed to form at low Au nanorod solution temperatures.

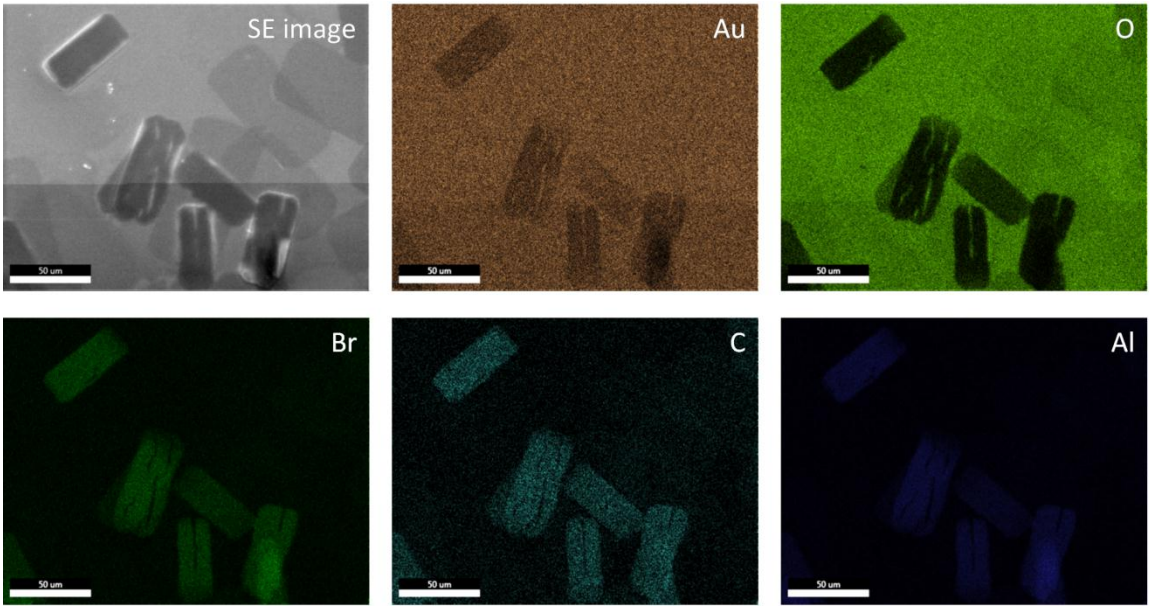

Figure 5-33. SEM secondary electron (SE) image and energy dispersive x-ray spectroscopy (EDS) elemental analysis maps of the platelets shown in Figure 5-32. Note that the Al signal for the platelets is likely to be actually from Br Lα signal (1.480 keV), which overlaps with the energy of Al Kα signal (1.486 keV).

Finally, we note that multiple assembly steps can be employed on the same sample to increase the assembly yield. Figure 5-34a presents statistics on yield for four different samples after one and two deposition steps. The yield improves significantly

after the second deposition for samples with initially low yield, and slightly for those already with high yield. Figure 5-34b shows SEM images of the same templates after the first and second assembly steps. Both the filling of initially unfilled templates and the addition of more nanocrystals to partially-filled templates can be observed after the second deposition. The loss of nanocrystals from the templates due to contact with the solvent was not observed, further suggesting that multiple assembly steps are generally additive to the number of assembled nanocrystals.

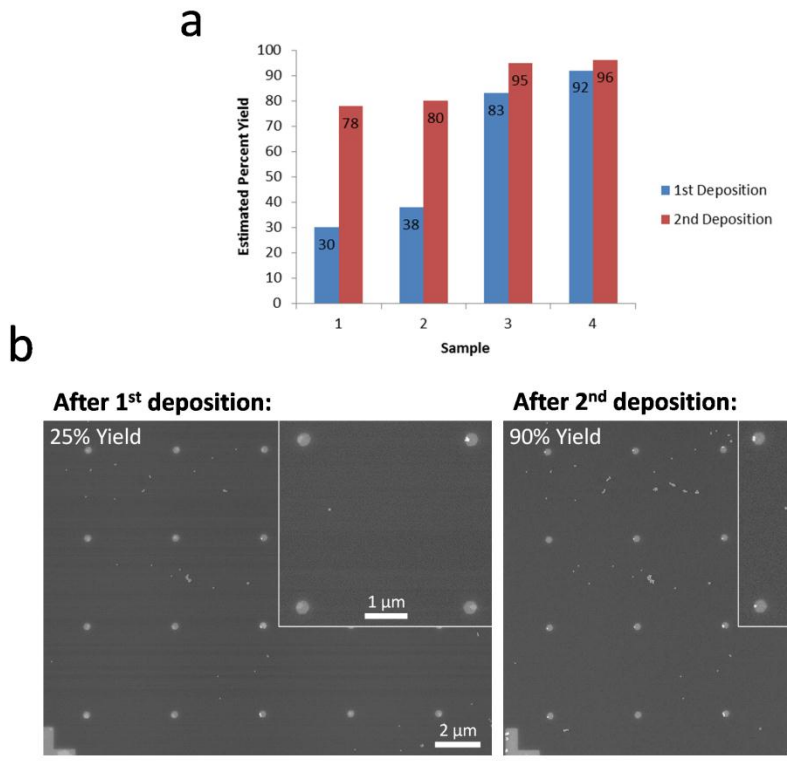

Figure 5-34. (a) Assembly yield statistics for four different samples after a 1st and 2nd deposition of nanocrystals. (b) SEM images of the same field of view after a 1st and 2nd deposition of nanocrystals.

5.10 Conclusions

This chapter has highlighted several extensions and future directions for applying template-assisted self-assembly to realize unique nanocrystal arrangements. In one-component systems, the coupling between nanocrystals can be engineered by tuning the interparticle separation and by specifying different geometries including circular and polygonal rings. 3D assemblies of plasmonic nanocrystals offer an additional dimension for designing the plasmonic response. Two-component systems incorporating constituents such as upconversion phosphors and phase-change materials harness the cooperative interactions among the individual components to enhance the overall functionality. The introduction of compositional and structural asymmetry by design enables access to new modes of nanocrystal arrangement and coupling. Through future work to structurally and spectroscopically characterize the assemblies, their functional properties can be determined and refined.

CHAPTER 6. CONCLUDING REMARKS

Throughout this dissertation we have been guided by the fundamental principles of materials science, namely, that understanding the relationships among processing, structure, and properties lead to improved materials performance. By utilizing template-assisted self-assembly to process plasmonic nanocrystals into new structural arrangements, we have explored how the plasmonic coupling in individual nanocrystal assemblies determines their collective optical properties. Our results point toward the improved performance of optical metamaterial assemblies in sensing, photovoltaics, optical information processing, and more.

The path toward ubiquitous implementation of nanostructured materials is only beginning to take shape. It is likely that many of the applications that will emerge have yet to be imagined. It is our hope that this dissertation offers a small step forward, and that a vigorous and collaborative scientific discourse will pave the way to unprecedented scientific vistas.

REFERENCES

(1) Shevchenko, E. V.; Talapin, D. V.; Kotov, N. A.; O'Brien, S.; Murray, C. B. Structural Diversity in Binary Nanoparticle Superlattices. *Nature* **2006**, *439*, 55–59.

(2) Ye, X.; Chen, J.; Eric Irrgang, M.; Engel, M.; Dong, A.; Glotzer, S. C.; Murray, C. B. Quasicrystalline Nanocrystal Superlattice with Partial Matching Rules. *Nat. Mater.* **2016**, *16*, 214–219.

(3) Kovalenko, M. V; Manna, L.; Cabot, A.; Hens, Z.; Talapin, D. V; Kagan, C. R.; Klimov, V. I.; Rogach, A. L.; Reiss, P.; Milliron, D. J.; *et al.* Prospects of Nanoscience with Nanocrystals. *ACS Nano* **2015**, 150122081035000.

(4) Boles, M. A.; Engel, M.; Talapin, D. V. Self-Assembly of Colloidal Nanocrystals: From Intricate Structures to Functional Materials. *Chem. Rev.* **2016**, acs.chemrev.6b00196.

(5) Wang, D.; Möhwald, H. Template-Directed Colloidal Self-Assembly – the Route to "top-Down" Nanochemical Engineering. *J. Mater. Chem.* **2004**, *14*, 459–468.

(6) van Blaaderen, A.; Ruel, R.; Wiltzius, P. Template-Directed Colloidal Crystallization. *Nature* **1997**, *385*, 321–324.

(7) Yin, Y.; Lu, Y.; Xia, Y. A Self-Assembly Approach to the Formation of Asymmetric Dimers from Monodispersed Spherical Colloids. *J. Am. Chem. Soc.* **2001**, *123*, 771–772.

(8) Yin, Y.; Lu, Y.; Gates, B.; Xia, Y. Template-Assisted Self-Assembly: A Practical Route to Complex Aggregates of Monodispersed Colloids with Well-Defined Sizes, Shapes, and Structures. *J. Am. Chem. Soc.* **2001**, *123*, 8718–8729.

(9) Yin, Y.; Lu, Y.; Xia, Y. Assembly of Monodispersed Spherical Colloids into One-Dimensional Aggregates Characterized by Well-Controlled Structures and Lengths. *J. Mater. Chem.* **2001**, *11*, 987–989.

(10) Yin, Y.; Xia, Y. Self-Assembly of Spherical Colloids into Helical Chains with Well-Controlled Handedness. *J. Am. Chem. Soc.* **2003**, *125*, 2048–2049.

(11) Xia, Y.; Yin, Y.; Lu, Y.; McLellan, J. Template-Assisted Self-Assembly of Spherical Colloids into Complex and Controllable Structures. *Adv. Funct. Mater.* **2003**, *13*, 907–918.

(12) Cui, Y.; Björk, M. T.; Liddle, J. A.; Sönnichsen, C.; Boussert, B.; Alivisatos, A. P.

Integration of Colloidal Nanocrystals into Lithographically Patterned Devices. *Nano Lett.* **2004**, *4*, 1093–1098.

(13) Liddle, J. A.; Cui, Y.; Alivisatos, P. Lithographically Directed Self-Assembly of Nanostructures. *J. Vac. Sci. Technol. B Microelectron. Nanom. Struct.* **2004**, *22*, 3409.

(14) Malaquin, L.; Kraus, T.; Schmid, H.; Delamarche, E.; Wolf, H. Controlled Particle Placement through Convective and Capillary Assembly. *Langmuir* **2007**, *23*, 11513–11521.

(15) Kraus, T.; Malaquin, L.; Schmid, H.; Riess, W.; Spencer, N. D.; Wolf, H. Nanoparticle Printing with Single-Particle Resolution. *Nat. Nanotechnol.* **2007**, *2*, 570–576.

(16) Rycenga, M.; Camargo, P. H. C.; Xia, Y. Template-Assisted Self-Assembly: A Versatile Approach to Complex Micro- and Nanostructures. *Soft Matter* **2009**, *5*, 1129.

(17) Kuemin, C.; Stutz, R.; Spencer, N. D.; Wolf, H. Precise Placement of Gold Nanorods by Capillary Assembly. *Langmuir* **2011**, *27*, 6305–6310.

(18) Kuemin, C.; Nowack, L.; Bozano, L.; Spencer, N. D.; Wolf, H. Oriented Assembly of Gold Nanorods on the Single-Particle Level. *Adv. Funct. Mater.* **2012**, *22*, 702–708.

(19) Zhou, Y.; Zhou, X.; Park, D. J.; Torabi, K.; Brown, K. A.; Jones, M. R.; Zhang, C.; Schatz, G. C.; Mirkin, C. A. Shape-Selective Deposition and Assembly of Anisotropic Nanoparticles. *Nano Lett.* **2014**, *14*, 2157–2161.

(20) Greybush, N. J.; Saboktakin, M.; Ye, X.; Della Giovampaola, C.; Oh, S. J.; Berry, N. E.; Engheta, N.; Murray, C. B.; Kagan, C. R. Plasmon-Enhanced Upconversion Luminescence in Single Nanophosphor–Nanorod Heterodimers Formed through Template-Assisted Self-Assembly. *ACS Nano* **2014**, *8*, 9482–9491.

(21) Greybush, N. J.; Liberal, I.; Malassis, L.; Kikkawa, J. M.; Engheta, N.; Murray, C. B.; Kagan, C. R. Plasmon Resonances in Self-Assembled Two-Dimensional Au Nanocrystal Metamolecules. *ACS Nano* **2017**, *11*, 2917–2927.

(22) Yang, Y.; Edwards, T. D.; Bevan, M. a. Modeling Depletion Mediated Colloidal Assembly on Topographical Patterns. *J. Colloid Interface Sci.* **2014**, *449*, 270–278.

(23) Mehraeen, S.; Asbahi, M.; Wang, F.; Yang, J. K. W.; Cao, J.; Tan, M. C. Directed Self-Assembly of Sub-10 Nm Particles: Role of Driving Forces and Template

Geometry in Packing and Ordering. *Langmuir* **2015**, 150706170646002.

(24) Ni, S.; Leemann, J.; Wolf, H.; Isa, L. Insights into Mechanisms of Capillary Assembly. *Faraday Discuss.* **2015**, *181*, 225–242.

(25) Pinedo Rivera, T.; Lecarme, O.; Hartmann, J.; Rossitto, E.; Berton, K.; Peyrade, D. Assisted Convective-Capillary Force Assembly of Gold Colloids in a Microfluidic Cell: Plasmonic Properties of Deterministic Nanostructures. *J. Vac. Sci. Technol. B Microelectron. Nanom. Struct.* **2008**, *26*, 2513–2519.

(26) Rivera, T. P.; Lecarme, O.; Hartmann, J.; Inglebert, R. L.; Peyrade, D. Spectroscopic Studies of Plasmonic Interactions in Colloidal Dimers Fabricated by Convective-Capillary Force Assembly. *Microelectron. Eng.* **2009**, *86*, 1089–1092.

(27) Lecarme, O.; Pinedo-Rivera, T.; Berton, K.; Berthier, J.; Peyrade, D. Plasmonic Coupling in Nondipolar Gold Colloidal Dimers. *Appl. Phys. Lett.* **2011**, *98*, 0–3.

(28) Fan, J. A.; Bao, K.; Sun, L.; Bao, J.; Manoharan, V. N.; Nordlander, P.; Capasso, F. Plasmonic Mode Engineering with Templated Self-Assembled Nanoclusters. *Nano Lett.* **2012**, *12*, 5318–5324.

(29) Chen, T.; Pourmand, M.; Feizpour, A.; Cushman, B.; Reinhard, B. M. Tailoring Plasmon Coupling in Self-Assembled One-Dimensional Au Nanoparticle Chains through Simultaneous Control of Size and Gap Separation. *J. Phys. Chem. Lett.* **2013**, *4*, 2147–2152.

(30) Flauraud, V.; Mastrangeli, M.; Bernasconi, G. D.; Butet, J.; Alexander, D. T. L.; Shahrabi, E.; Martin, O. J. F.; Brugger, J. Nanoscale Topographical Control of Capillary Assembly of Nanoparticles. *Nat. Nanotechnol.* **2016**.

(31) Maier, S. A. *Plasmonics: Fundamentals and Applications*; Springer: New York, 2007.

(32) Pelton, M.; Aizpurua, J.; Bryant, G. Metal-nanoparticle Plasmonics. *Laser Photonics Rev.* **2008**, *2*, 136–159.

(33) Gong, J.; Li, G.; Tang, Z. Self-Assembly of Noble Metal Nanocrystals: Fabrication, Optical Property, and Application. *Nano Today* **2012**, *7*, 564–585.

(34) Naik, G. V; Shalaev, V. M.; Boltasseva, A. Alternative Plasmonic Materials: Beyond Gold and Silver. *Adv. Mater.* **2013**, *25*, 3264–3294.

(35) Tcherniak, A.; Ha, J. W.; Dominguez-Medina, S.; Slaughter, L. S.; Link, S. Probing a Century Old Prediction One Plasmonic Particle at a Time. *Nano Lett.*

2010, *10*, 1398–1404.

(36) Mock, J. J.; Barbic, M.; Smith, D. R.; Schultz, D. A.; Schultz, S. Shape Effects in Plasmon Resonance of Individual Colloidal Silver Nanoparticles. *J. Chem. Phys.* **2002**, *116*, 6755.

(37) Rycenga, M.; Cobley, C. M.; Zeng, J.; Li, W.; Moran, C. H.; Zhang, Q.; Qin, D.; Xia, Y. Controlling the Synthesis and Assembly of Silver Nanostructures for Plasmonic Applications. *Chem. Rev.* **2011**, *111*, 3669–3712.

(38) Biagioni, P.; Huang, J.; Hecht, B. Nanoantennas for Visible and Infrared Radiation. *Reports Prog. Phys.* **2012**, 76.

(39) Prodan, E.; Radloff, C.; Halas, N. J.; Nordlander, P. A Hybridization Model for the Plasmon Response of Complex Nanostructures. *Science* **2003**, *302*, 419–422.

(40) Luk'yanchuk, B.; Zheludev, N. I.; Maier, S. A.; Halas, N. J.; Nordlander, P.; Giessen, H.; Chong, C. T. The Fano Resonance in Plasmonic Nanostructures and Metamaterials. *Nat. Mater.* **2010**, *9*, 707–715.

(41) Alù, A.; Engheta, N. The Quest for Magnetic Plasmons at Optical Frequencies. *Opt. Express* **2009**, *17*, 5723–5730.

(42) Halas, N. J.; Lal, S.; Chang, W. S.; Link, S.; Nordlander, P. Plasmons in Strongly Coupled Metallic Nanostructures. *Chemical Reviews*, 2011, *111*, 3913–3961.

(43) Atwater, H. A.; Polman, A. Plasmonics for Improved Photovoltaic Devices. *Nat. Mater.* **2010**, *9*, 865–865.

(44) Engheta, N. Circuits with Light at Nanoscales: Optical Nanocircuits Inspired by Metamaterials. *Science* **2007**, *317*, 1698–1702.

(45) Anker, J. N.; Hall, W. P.; Lyandres, O.; Shah, N. C.; Zhao, J.; Van Duyne, R. P. Biosensing with Plasmonic Nanosensors. *Nat. Mater.* **2008**, *7*, 442–453.

(46) Hou, W.; Cronin, S. B. A Review of Surface Plasmon Resonance-Enhanced Photocatalysis. *Adv. Funct. Mater.* **2013**, *23*, 1612–1619.

(47) Kawata, S.; Inouye, Y.; Verma, P. Plasmonics for near-Field Nano-Imaging and Superlensing. *Nat. Photonics* **2009**, *3*, 388–394.

(48) Chen, P. Y.; Soric, J.; Al??, A. Invisibility and Cloaking Based on Scattering Cancellation. *Adv. Mater.* **2012**, *24*, 281–304.

(49) Chen, H.; Shao, L.; Li, Q.; Wang, J. Gold Nanorods and Their Plasmonic Properties. *Chem. Soc. Rev. Chem. Soc. Rev* **2013**, *42*, 2679–2724.

(50) Haase, M.; Schäfer, H. Upconverting Nanoparticles. *Angew. Chem. Int. Ed. Engl.* **2011**, *50*, 5808–5829.

(51) Heer, S.; Kömpe, K.; Güdel, H.-U.; Haase, M. Highly Efficient Multicolour Upconversion Emission in Transparent Colloids of Lanthanide-Doped $NaYF_4$ Nanocrystals. *Adv. Mater.* **2004**, *16*, 2102–2105.

(52) Yi, G.; Lu, H.; Zhao, S.; Ge, Y.; Yang, W.; Chen, D.; Guo, L.-H. Synthesis, Characterization, and Biological Application of Size-Controlled Nanocrystalline $NaYF_4$:Yb,Er Infrared-to-Visible Up-Conversion Phosphors. *Nano Lett.* **2004**, *4*, 2191–2196.

(53) Mai, H.-X.; Zhang, Y.-W.; Si, R.; Yan, Z.-G.; Sun, L.; You, L.-P.; Yan, C.-H. High-Quality Sodium Rare-Earth Fluoride Nanocrystals: Controlled Synthesis and Optical Properties. *J. Am. Chem. Soc.* **2006**, *128*, 6426–6436.

(54) Ye, X.; Collins, J. E.; Kang, Y.; Chen, J.; Chen, D. T. N.; Yodh, A. G.; Murray, C. B. Morphologically Controlled Synthesis of Colloidal Upconversion Nanophosphors and Their Shape-Directed Self-Assembly. *Proc. Natl. Acad. Sci. U. S. A.* **2010**, *107*, 22430–22435.

(55) Wang, F.; Han, Y.; Lim, C. S.; Lu, Y.; Wang, J.; Xu, J.; Chen, H.; Zhang, C.; Hong, M.; Liu, X. Simultaneous Phase and Size Control of Upconversion Nanocrystals through Lanthanide Doping. *Nature* **2010**, *463*, 1061–1065.

(56) Chan, E. M.; Han, G.; Goldberg, J. D.; Gargas, D. J.; Ostrowski, A. D.; Schuck, P. J.; Cohen, B. E.; Milliron, D. J. Combinatorial Discovery of Lanthanide-Doped Nanocrystals with Spectrally Pure Upconverted Emission. *Nano Lett.* **2012**, *12*, 3839–3845.

(57) Gargas, D. J.; Chan, E. M.; Ostrowski, A. D.; Aloni, S.; Altoe, M. V. P.; Barnard, E. S.; Sanii, B.; Urban, J. J.; Milliron, D. J.; Cohen, B. E.; *et al.* Engineering Bright Sub-10-Nm Upconverting Nanocrystals for Single-Molecule Imaging. *Nat. Nanotechnol.* **2014**, *9*, 300–305.

(58) Trupke, T.; Green, M. A.; Wurfel, P. Improving Solar Cell Efficiencies by Up-Conversion of Sub-Band-Gap Light. *J. Appl. Phys.* **2002**, *92*, 4117–4122.

(59) Shalav, A.; Richards, B. S.; Trupke, T.; Krämer, K. W.; Güdel, H. U. Application of $NaYF_4$:Er^{3+} Up-Converting Phosphors for Enhanced Near-Infrared Silicon Solar Cell Response. *Appl. Phys. Lett.* **2005**, *86*, 13505.

(60) van der Ende, B. M.; Aarts, L.; Meijerink, A. Lanthanide Ions as Spectral Converters for Solar Cells. *Phys. Chem. Chem. Phys.* **2009**, *11*, 11081–11095.

(61) Briggs, J. A.; Atre, A. C.; Dionne, J. A. Narrow-Bandwidth Solar Upconversion: Case Studies of Existing Systems and Generalized Fundamental Limits. *J. Appl. Phys.* **2013**, *113*, 124509.

(62) Lim, S. F.; Riehn, R.; Ryu, W. S.; Khanarian, N.; Tung, C.; Tank, D.; Austin, R. H. In Vivo and Scanning Electron Microscopy Imaging of Upconverting Nanophosphors in Caenorhabditis Elegans. *Nano Lett.* **2006**, *6*, 169–174.

(63) Nyk, M.; Kumar, R.; Ohulchanskyy, T. Y.; Bergey, E. J.; Prasad, P. N. High Contrast in Vitro and in Vivo Photoluminescence Bioimaging Using Near Infrared to Near Infrared Up-Conversion in Tm^{3+} and Yb^{3+} Doped Fluoride Nanophosphors. *Nano Lett.* **2008**, *8*, 3834–3838.

(64) Chatterjee, D. K.; Rufaihah, A. J.; Zhang, Y. Upconversion Fluorescence Imaging of Cells and Small Animals Using Lanthanide Doped Nanocrystals. *Biomaterials* **2008**, *29*, 937–943.

(65) Wang, F.; Banerjee, D.; Liu, Y.; Chen, X.; Liu, X. Upconversion Nanoparticles in Biological Labeling, Imaging, and Therapy. *Analyst* **2010**, *135*, 1839–1854.

(66) Esipova, T. V; Ye, X.; Collins, J. E.; Sakadžić, S.; Mandeville, E. T.; Murray, C. B.; Vinogradov, S. A. Dendritic Upconverting Nanoparticles Enable in Vivo Multiphoton Microscopy with Low-Power Continuous Wave Sources. *Proc. Natl. Acad. Sci. U. S. A.* **2012**, *109*, 20826–20831.

(67) Milliez, J.; Rapaport, A.; Bass, M.; Cassanho, A.; Jenssen, H. P. High-Brightness White-Light Source Based on Up-Conversion Phosphors. *J. Disp. Technol.* **2006**, *2*, 307–311.

(68) Liu, X.; Dong, G.; Qiao, Y.; Qiu, J. Transparent Colloid Containing Upconverting Nanocrystals: An Alternative Medium for Three-Dimensional Volumetric Display. *Appl. Opt.* **2008**, *47*, 6416–6421.

(69) Rapaport, A.; Milliez, J.; Bass, M.; Cassanho, A.; Jenssen, H. Review of the Properties of Up-Conversion Phosphors for New Emissive Displays. *J. Disp. Technol.* **2006**, *2*, 68–78.

(70) Boyer, J.-C.; van Veggel, F. C. J. M. Absolute Quantum Yield Measurements of Colloidal $NaYF_4$: Er^{3+}, Yb^{3+} Upconverting Nanoparticles. *Nanoscale* **2010**, *2*, 1417–1419.

(71) Faulkner, D. O.; Petrov, S.; Perovic, D. D.; Kherani, N. P.; Ozin, G. A. Absolute Quantum Yields in $NaYF_4$:Er,Yb Upconverters – Synthesis Temperature and Power Dependence. *J. Mater. Chem.* **2012**, *22*, 24330.

(72) Liu, H.; Xu, C. T.; Lindgren, D.; Xie, H.; Thomas, D.; Gundlach, C.; Andersson-Engels, S. Balancing Power Density Based Quantum Yield Characterization of Upconverting Nanoparticles for Arbitrary Excitation Intensities. *Nanoscale* **2013**, *5*, 4770–4775.

(73) Wang, F.; Liu, X. Recent Advances in the Chemistry of Lanthanide-Doped Upconversion Nanocrystals. *Chem. Soc. Rev.* **2009**, *38*, 976–989.

(74) Liu, C.; Zhang, L.; Zheng, Q.; Luo, F.; Xu, Y.; Weng, W. Advances in the Surface Engineering of Upconversion Nanocrystals. *Sci. Adv. Mater.* **2012**, *4*, 1–22.

(75) Qiu, P.; Zhou, N.; Chen, H.; Zhang, C.; Gao, G.; Cui, D. Recent Advances in Lanthanide-Doped Upconversion Nanomaterials: Synthesis, Nanostructures and Surface Modification. *Nanoscale* **2013**, *5*, 11512–11525.

(76) Chen, G.; Yang, C.; Prasad, P. N. Nanophotonics and Nanochemistry: Controlling the Excitation Dynamics for Frequency Up- and Down-Conversion in Lanthanide-Doped Nanoparticles. *Acc. Chem. Res.* **2013**, *46*, 1474–1486.

(77) Wang, F.; Deng, R.; Wang, J.; Wang, Q.; Han, Y.; Zhu, H.; Chen, X.; Liu, X. Tuning Upconversion through Energy Migration in Core-Shell Nanoparticles. *Nat. Mater.* **2011**, *10*, 968–973.

(78) Wang, J.; Deng, R.; MacDonald, M. A.; Chen, B.; Yuan, J.; Wang, F.; Chi, D.; Hor, T. S. A.; Zhang, P.; Liu, G.; *et al*. Enhancing Multiphoton Upconversion through Energy Clustering at Sublattice Level. *Nat. Mater.* **2014**, *13*, 157–162.

(79) Kulakovich, O.; Strekal, N.; Yaroshevich, A.; Maskevich, S.; Gaponenko, S.; Nabiev, I.; Woggon, U.; Artemyev, M. Enhanced Luminescence of CdSe Quantum Dots on Gold Colloids. *Nano Lett.* **2002**, *2*, 1449–1452.

(80) Song, J.-H.; Atay, T.; Shi, S.; Urabe, H.; Nurmikko, A. V. Large Enhancement of Fluorescence Efficiency from CdSe/ZnS Quantum Dots Induced by Resonant Coupling to Spatially Controlled Surface Plasmons. *Nano Lett.* **2005**, *5*, 1557–1561.

(81) Pompa, P. P.; Martiradonna, L.; Della Torre, A.; Della Sala, F.; Manna, L.; De Vittorio, M.; Calabi, F.; Cingolani, R.; Rinaldi, R. Metal-Enhanced Fluorescence of Colloidal Nanocrystals with Nanoscale Control. *Nat. Nanotechnol.* **2006**, *1*, 126–130.

(82) Kühn, S.; Håkanson, U.; Rogobete, L.; Sandoghdar, V. Enhancement of Single-Molecule Fluorescence Using a Gold Nanoparticle as an Optical Nanoantenna. *Phys. Rev. Lett.* **2006**, *97*, 17402.

(83) Kinkhabwala, A.; Yu, Z.; Fan, S.; Avlasevich, Y.; Müllen, K.; Moerner, W. E. Large Single-Molecule Fluorescence Enhancements Produced by a Bowtie Nanoantenna. *Nat. Photonics* **2009**, *3*, 654–657.

(84) Anger, P.; Bharadwaj, P.; Novotny, L. Enhancement and Quenching of Single-Molecule Fluorescence. *Phys. Rev. Lett.* **2006**, *96*, 113002.

(85) Saboktakin, M.; Ye, X.; Oh, S. J.; Hong, S.-H.; Fafarman, A. T.; Chettiar, U. K.; Engheta, N.; Murray, C. B.; Kagan, C. R. Metal-Enhanced Upconversion Luminescence Tunable through Metal Nanoparticle–Nanophosphor Separation. *ACS Nano* **2012**, *6*, 8758–8766.

(86) Schietinger, S.; Aichele, T.; Wang, H.-Q.; Nann, T.; Benson, O. Plasmon-Enhanced Upconversion in Single $NaYF_4$:Yb^{3+}/Er^{3+} Codoped Nanocrystals. *Nano Lett.* **2010**, *10*, 134–138.

(87) Feng, W.; Sun, L.-D.; Yan, C.-H. Ag Nanowires Enhanced Upconversion Emission of $NaYF_4$:Yb,Er Nanocrystals via a Direct Assembly Method. *Chem. Commun. (Camb).* **2009**, 4393–4395.

(88) Zhang, S.-Z.; Sun, L.-D.; Tian, H.; Liu, Y.; Wang, J.-F.; Yan, C.-H. Reversible Luminescence Switching of $NaYF_4$:Yb,Er Nanoparticles with Controlled Assembly of Gold Nanoparticles. *Chem. Commun. (Camb).* **2009**, 2547–2549.

(89) Xu, W.; Xu, S.; Zhu, Y.; Liu, T.; Bai, X.; Dong, B.; Xu, L.; Song, H. Ultra-Broad Plasma Resonance Enhanced Multicolor Emissions in an Assembled Ag/$NaYF_4$:Yb,Er Nano-Film. *Nanoscale* **2012**, *4*, 6971–6973.

(90) Wawrzynczyk, D.; Bednarkiewicz, A.; Nyk, M.; Gordel, M.; Strek, W.; Samoc, M. Modulation of Up-Conversion Luminescence of Lanthanide(III) Ion Co-Doped $NaYF_4$ Nanoparticles Using Gold Nanorods. *Opt. Mater. (Amst).* **2012**, *34*, 1708–1712.

(91) Saboktakin, M.; Ye, X.; Chettiar, U. K.; Engheta, N.; Murray, C. B.; Kagan, C. R. Plasmonic Enhancement of Nanophosphor Upconversion Luminescence in Au Nanohole Arrays. *ACS Nano* **2013**, *7*, 7186–7192.

(92) Zhang, W.; Ding, F.; Chou, S. Y. Large Enhancement of Upconversion Luminescence of $NaYF_4$:Yb^{3+}/Er^{3+} Nanocrystal by 3D Plasmonic Nano-Antennas. *Adv. Mater.* **2012**, *24*, OP236-41.

(93) Sun, Q.-C.; Mundoor, H.; Ribot, J. C.; Singh, V.; Smalyukh, I. I.; Nagpal, P. Plasmon-Enhanced Energy Transfer for Improved Upconversion of Infrared Radiation in Doped-Lanthanide Nanocrystals. *Nano Lett.* **2014**, *14*, 101–106.

(94) Paudel, H. P.; Zhong, L.; Bayat, K.; Baroughi, M. F.; Smith, S.; Lin, C.; Jiang, C.; Berry, M. T.; May, P. S. Enhancement of Near-Infrared-to-Visible Upconversion Luminescence Using Engineered Plasmonic Gold Surfaces. *J. Phys. Chem. C* **2011**, *115*, 19028–19036.

(95) Paudel, H. P.; Dachhepati, D.; Bayat, K.; Mottaghian, S. S.; May, P. S.; Lin, C.; Smith, S.; Baroughi, M. F. Design, Fabrication, and Characterization of a Plasmonic Upconversion Enhancer and Its Prospects for Photovoltaics. *J. Photonics Energy* **2013**, *3*, 35598.

(96) Zhang, H.; Xu, D.; Huang, Y.; Duan, X. Highly Spectral Dependent Enhancement of Upconversion Emission with Sputtered Gold Island Films. *Chem. Commun. (Camb).* **2011**, *47*, 979–981.

(97) Xu, W.; Zhu, Y.; Chen, X.; Wang, J.; Tao, L.; Xu, S.; Liu, T.; Song, H. A Novel Strategy for Improving Upconversion Luminescence of $NaYF_4$:Yb, Er Nanocrystals by Coupling with Hybrids of Silver Plasmon Nanostructures and Poly(methyl Methacrylate) Photonic Crystals. *Nano Res.* **2013**, *6*, 795–807.

(98) Zhang, C.; Lee, J. Y. Synthesis of Au Nanorod@Amine-Modified Silica@Rare-Earth Fluoride Nanodisk Core–Shell–Shell Heteronanostructures. *J. Phys. Chem. C* **2013**, *117*, 15253–15259.

(99) Ge, W.; Zhang, X. R.; Liu, M.; Lei, Z. W.; Knize, R. J.; Lu, Y. Distance Dependence of Gold-Enhanced Upconversion Luminescence in $Au/SiO_2/Y_2O_3$:Yb^{3+}, Er^{3+} Nanoparticles. *Theranostics* **2013**, *3*, 282–288.

(100) Zhang, H.; Li, Y.; Ivanov, I. A.; Qu, Y.; Huang, Y.; Duan, X. Plasmonic Modulation of the Upconversion Fluorescence in $NaYF_4$:Yb/Tm Hexaplate Nanocrystals Using Gold Nanoparticles or Nanoshells. *Angew. Chem. Int. Ed. Engl.* **2010**, *49*, 2865–2868.

(101) Sudheendra, L.; Ortalan, V.; Dey, S.; Browning, N. D.; Kennedy, I. M. Plasmonic Enhanced Emissions from Cubic NaYF4:Yb:Er/Tm Nanophosphors. *Chem. Mater.* **2011**, *23*, 2987–2993.

(102) Deng, W.; Sudheendra, L.; Zhao, J.; Fu, J.; Jin, D.; Kennedy, I. M.; Goldys, E. M. Upconversion in $NaYF_4$:Yb, Er Nanoparticles Amplified by Metal Nanostructures. *Nanotechnology* **2011**, *22*, 325604.

(103) Yuan, P.; Lee, Y. H.; Gnanasammandhan, M. K.; Guan, Z.; Zhang, Y.; Xu, Q.-H. Plasmon Enhanced Upconversion Luminescence of $NaYF_4$:Yb,Er@SiO_2@Ag Core-Shell Nanocomposites for Cell Imaging. *Nanoscale* **2012**, *4*, 5132–5137.

(104) Kannan, P.; Abdul Rahim, F.; Chen, R.; Teng, X.; Huang, L.; Sun, H.; Kim, D.-H. Au Nanorod Decoration on $NaYF_4$:Yb/Tm Nanoparticles for Enhanced Emission and Wavelength-Dependent Biomolecular Sensing. *ACS Appl. Mater. Interfaces* **2013**, *5*, 3508–3513.

(105) Kodama, T.; Fujii, M.; Nakano, T.; Imakita, K.; Hayashi, S. Enhancement of Upconversion Luminescence of Er and Yb Co-Doped Y_2O_3 Nanoparticle by Ag Half-Shell. *Opt. Mater. (Amst).* **2013**, *35*, 2394–2399.

(106) Schietinger, S.; Menezes, L. D. S.; Lauritzen, B.; Benson, O. Observation of Size Dependence in Multicolor Upconversion in Single Yb^{3+}, Er^{3+} Codoped $NaYF_4$ Nanocrystals. *Nano Lett.* **2009**, *9*, 2477–2481.

(107) Wu, S.; Han, G.; Milliron, D. J.; Aloni, S.; Altoe, V.; Talapin, D. V; Cohen, B. E.; Schuck, P. J. Non-Blinking and Photostable Upconverted Luminescence from Single Lanthanide-Doped Nanocrystals. *Proc. Natl. Acad. Sci. U. S. A.* **2009**, *106*, 10917–10921.

(108) Ostrowski, A. D.; Chan, E. M.; Gargas, D. J.; Katz, E. M.; Han, G.; Schuck, P. J.; Milliron, D. J.; Cohen, B. E. Controlled Synthesis and Single-Particle Imaging of Bright, Sub-10 Nm Lanthanide-Doped Upconverting Nanocrystals. *ACS Nano* **2012**, *6*, 2686–2692.

(109) Zhao, J.; Jin, D.; Schartner, E. P.; Lu, Y.; Liu, Y.; Zvyagin, A. V; Zhang, L.; Dawes, J. M.; Xi, P.; Piper, J. A.; *et al.* Single-Nanocrystal Sensitivity Achieved by Enhanced Upconversion Luminescence. *Nat Nano* **2013**, *8*, 729–734.

(110) Zhou, X.; Zhou, Y.; Ku, J. C.; Zhang, C.; Mirkin, C. A. Capillary Force-Driven, Large-Area Alignment of Multi-Segmented Nanowires. *ACS Nano* **2014**, *8*, 1511–1516.

(111) Yan, B.; Thubagere, A.; Premasiri, W. R.; Ziegler, L. D.; Dal Negro, L.; Reinhard, B. M. Engineered SERS Substrates with Multiscale Signal Enhancement: Nanoparticle Cluster Arrays. *ACS Nano* **2009**, *3*, 1190–1202.

(112) Holzner, F.; Kuemin, C.; Paul, P.; Hedrick, J. L.; Wolf, H.; Spencer, N. D.; Duerig, U.; Knoll, A. W. Directed Placement of Gold Nanorods Using a Removable Template for Guided Assembly. *Nano Lett.* **2011**, *11*, 3957–3962.

(113) Henzie, J.; Andrews, S. C.; Ling, X. Y.; Li, Z.; Yang, P. Oriented Assembly of

Polyhedral Plasmonic Nanoparticle Clusters. *Proc. Natl. Acad. Sci. U. S. A.* **2013**, *110*, 6640–6645.

(114) Hong, Y.; Qiu, Y.; Chen, T.; Reinhard, B. M. Rational Assembly of Optoplasmonic Hetero-Nanoparticle Arrays with Tunable Photonic-Plasmonic Resonances. *Adv. Funct. Mater.* **2014**, *24*, 739–746.

(115) Giannini, V.; Fernández-Domínguez, A. I.; Heck, S. C.; Maier, S. A. Plasmonic Nanoantennas: Fundamentals and Their Use in Controlling the Radiative Properties of Nanoemitters. *Chem. Rev.* **2011**, *111*, 3888–3912.

(116) Giannini, V.; Sánchez-Gil, J. A. Excitation and Emission Enhancement of Single Molecule Fluorescence through Multiple Surface-Plasmon Resonances on Metal Trimer Nanoantennas. *Opt. Lett.* **2008**, *33*, 899–901.

(117) Munechika, K.; Chen, Y.; Tillack, A. F.; Kulkarni, A. P.; Plante, I. J.-L.; Munro, A. M.; Ginger, D. S. Spectral Control of Plasmonic Emission Enhancement from Quantum Dots near Single Silver Nanoprisms. *Nano Lett.* **2010**, *10*, 2598–2603.

(118) Black, C. T.; Murray, C. B.; Sandstrom, R. L. Embedded Nanoparticle Films and Method for Their Formation in Selective Areas on a Surface. US 7,682,591 B2, 2010.

(119) Ming, T.; Zhao, L.; Yang, Z.; Chen, H.; Sun, L.; Wang, J.; Yan, C. Strong Polarization Dependence of Plasmon-Enhanced Fluorescence on Single Gold Nanorods. *Nano Lett.* **2009**, *9*, 3896–3903.

(120) Pollnau, M.; Gamelin, D.; Lüthi, S.; Güdel, H.; Hehlen, M. Power Dependence of Upconversion Luminescence in Lanthanide and Transition-Metal-Ion Systems. *Phys. Rev. B* **2000**, *61*, 3337–3346.

(121) Suyver, J.; Aebischer, A.; García-Revilla, S.; Gerner, P.; Güdel, H. Anomalous Power Dependence of Sensitized Upconversion Luminescence. *Phys. Rev. B* **2005**, *71*, 125123.

(122) Bryant, G. W.; García de Abajo, F. J.; Aizpurua, J. Mapping the Plasmon Resonances of Metallic Nanoantennas. *Nano Lett.* **2008**, *8*, 631–636.

(123) Ye, X.; Zheng, C.; Chen, J.; Gao, Y.; Murray, C. B. Using Binary Surfactant Mixtures To Simultaneously Improve the Dimensional Tunability and Monodispersity in the Seeded Growth of Gold Nanorods. *Nano Lett.* **2013**, *13*, 765–771.

(124) Palik, E. D. *Handbook of Optical Constants of Solids*; Academic Press: Boston,

1985.

(125) Banski, M.; Afzaal, M.; Podhorodecki, A.; Misiewicz, J.; Abdelhady, A. L.; O'Brien, P. Passivation of Lanthanide Surface Sites in Sub-10 Nm $NaYF_4:Eu^{3+}$ Nanocrystals. *J. Nanopart. Res.* **2012**, *14*, 1228.

(126) Müllen, K. Evolution of Graphene Molecules: Structural and Functional Complexity as Driving Forces behind Nanoscience. *ACS Nano* **2014**, *8*, 6531–6541.

(127) Watson, M. D.; Fechtenkötter, A.; Müllen, K. Big Is Beautiful - "Aromaticity" revisited from the Viewpoint of Macromolecular and Supramolecular Benzene Chemistry. *Chem. Rev.* **2001**, *101*, 1267–1300.

(128) Zdetsis, A. D.; Economou, E. N. A Pedestrian Approach to the Aromaticity of Graphene and Nanographene: Significance of Huckel's $(4n+2)\pi$ Electron Rule. *J. Phys. Chem. C* **2015**, 150713062235000.

(129) Popov, I. A.; Bozhenko, K. V.; Boldyrev, A. I. Is Graphene Aromatic? *Nano Res.* **2012**, *5*, 117–123.

(130) Guerrero-Martínez, A.; Grzelczak, M.; Liz-Marzán, L. M. Molecular Thinking for Nanoplasmonic Design. *ACS Nano* **2012**, *6*, 3655–3662.

(131) Klimov, V. V.; Guzatov, D. V. Plasmonic Atoms and Plasmonic Molecules. *Appl. Phys. A Mater. Sci. Process.* **2007**, *89*, 305–314.

(132) Remacle, F.; Levine, R. D. Quantum Dots as Chemical Building Blocks: Elementary Theoretical Considerations. *ChemPhysChem* **2001**, *2*, 20–36.

(133) Cherqui, C.; Bigelow, N. W.; Vaschillo, A.; Goldwyn, H.; Masiello, D. J. Combined Tight-Binding and Numerical Electrodynamics Understanding of the STEM/EELS Magneto-Optical Responses of Aromatic Plasmon-Supporting Metal Oligomers. *ACS Photonics* **2014**, *1*, 1013–1024.

(134) Alù, A.; Engheta, N. Achieving Transparency with Plasmonic and Metamaterial Coatings. *Phys. Rev. E* **2005**, *72*, 16623.

(135) Fang, N. Sub-Diffraction-Limited Optical Imaging with a Silver Superlens. *Science* **2005**, *308*, 534–537.

(136) Valentine, J.; Zhang, S.; Zentgraf, T.; Ulin-Avila, E.; Genov, D. A.; Bartal, G.; Zhang, X. Three-Dimensional Optical Metamaterial with a Negative Refractive Index. *Nature* **2008**, *455*, 376–379.

(137) Shalaev, V. M. Transforming Light. *Science* **2008**, *322*, 384–386.

(138) Mirin, N. A.; Bao, K.; Nordlander, P. Fano Resonances in Plasmonic Nanoparticle Aggregates. *J. Phys. Chem. A* **2009**, *113*, 4028–4034.

(139) Fan, J. A.; Wu, C.; Bao, K.; Bao, J.; Bardhan, R.; Halas, N. J.; Manoharan, V. N.; Nordlander, P.; Shvets, G.; Capasso, F. Self-Assembled Plasmonic Nanoparticle Clusters. *Science* **2010**, *328*, 1135–1138.

(140) Chuntonov, L.; Haran, G. Trimeric Plasmonic Molecules: The Role of Symmetry. *Nano Lett.* **2011**, *11*, 2440–2445.

(141) Sheikholeslami, S. N.; García-Etxarri, A.; Dionne, J. A. Controlling the Interplay of Electric and Magnetic Modes via Fano-like Plasmon Resonances. *Nano Lett.* **2011**, *11*, 3927–3934.

(142) Shafiei, F.; Monticone, F.; Le, K. Q.; Liu, X.-X.; Hartsfield, T.; Alù, A.; Li, X. A Subwavelength Plasmonic Metamolecule Exhibiting Magnetic-Based Optical Fano Resonance. *Nat. Nanotechnol.* **2013**, *8*, 95–99.

(143) Zhao, L.; Kelly, K. L.; Schatz, G. C. The Extinction Spectra of Silver Nanoparticle Arrays: Influence of Array Structure on Plasmon Resonance Wavelength and Width. *J. Phys. Chem. B* **2003**, *107*, 7343–7350.

(144) Chen, C.-F.; Tzeng, S.-D.; Chen, H.-Y.; Lin, K.-J.; Gwo, S. Tunable Plasmonic Response from Alkanethiolate-Stabilized Gold Nanoparticle Superlattices: Evidence of Near-Field Coupling. *J. Am. Chem. Soc.* **2008**, *130*, 824–826.

(145) Ben, X.; Park, H. S. Size Dependence of the Plasmon Ruler Equation for Two-Dimensional Metal Nanosphere Arrays. *J. Phys. Chem. C* **2011**, *115*, 15915–15926.

(146) Jain, P. K.; Huang, W.; El-Sayed, M. A. On the Universal Scaling Behavior of the Distance Decay of Plasmon Coupling in Metal Nanoparticle Pairs: A Plasmon Ruler Equation. *Nano Lett.* **2007**, *7*, 2080–2088.

(147) Russier, V.; Pileni, M. P. Optical Absorption Spectra of Arrays of Metal Particles from Cluster Calculations: Cluster Size and Shape Effects. *Surf. Sci.* **1999**, *425*, 313–325.

(148) Russier, V.; Pileni, M. P. Cluster Calculations of Optical Absorption Spectra of 2D Metal Particles Arrays: Cluster Size Effects. *Appl. Surf. Sci.* **2000**, *162–163*, 644–649.

(149) Toma, M.; Toma, K.; Michioka, K.; Ikezoe, Y.; Obara, D.; Okamoto, K.; Tamada, K. Collective Plasmon Modes Excited on a Silver Nanoparticle 2D Crystalline Sheet. *Phys. Chem. Chem. Phys.* **2011**, *13*, 7459–7466.

(150) Liu, N.; Mukherjee, S.; Bao, K.; Brown, L. V; Dorfmüller, J.; Nordlander, P.; Halas, N. J. Magnetic Plasmon Formation and Propagation in Artificial Aromatic Molecules. *Nano Lett.* **2012**, *12*, 364–369.

(151) Liu, N.; Mukherjee, S.; Bao, K.; Li, Y.; Brown, L. V.; Nordlander, P.; Halas, N. J. Manipulating Magnetic Plasmon Propagation in Metallic Nanocluster Networks. *ACS Nano* **2012**, *6*, 5482–5488.

(152) Hentschel, M.; Saliba, M.; Vogelgesang, R.; Giessen, H.; Alivisatos, A. P.; Liu, N. Transition from Isolated to Collective Modes in Plasmonic Oligomers. *Nano Lett.* **2010**, *10*, 2721–2726.

(153) Hentschel, M.; Dregely, D.; Vogelgesang, R.; Giessen, H.; Liu, N. Plasmonic Oligomers: The Role of Individual Particles in Collective Behavior. *ACS Nano* **2011**, *5*, 2042–2050.

(154) Dregely, D.; Hentschel, M.; Giessen, H. Excitation and Tuning of Higher-Order Fano Resonances in Plasmonic Oligomer Clusters. *ACS Nano* **2011**, *5*, 8202–8211.

(155) Chen, K.-P.; Drachev, V. P.; Borneman, J. D.; Kildishev, A. V.; Shalaev, V. M. Drude Relaxation Rate in Grained Gold Nanoantennas. *Nano Lett.* **2010**, *10*, 916–922.

(156) Huang, J.-S.; Callegari, V.; Geisler, P.; Brüning, C.; Kern, J.; Prangsma, J. C.; Wu, X.; Feichtner, T.; Ziegler, J.; Weinmann, P.; *et al.* Atomically Flat Single-Crystalline Gold Nanostructures for Plasmonic Nanocircuitry. *Nat. Commun.* **2010**, *1*, 150.

(157) Shi, J.; Monticone, F.; Elias, S.; Wu, Y.; Ratchford, D.; Li, X.; Alù, A. Modular Assembly of Optical Nanocircuits. *Nat. Commun.* **2014**, *5*, 3896.

(158) Sun, L.; Ma, T.; Yang, S.-C.; Kim, D.-K.; Lee, G.; Shi, J.; Martinez, I.; Yi, G.-R.; Shvets, G.; Li, X. Interplay Between Optical Bianisotropy and Magnetism in Plasmonic Metamolecules. *Nano Lett.* **2016**, *16*, 4322–4328.

(159) Tian, X.; Zhou, Y.; Thota, S.; Zou, S.; Zhao, J. Plasmonic Coupling in Single Silver Nanosphere Assemblies by Polarization-Dependent Dark-Field Scattering Spectroscopy. *J. Phys. Chem. C* **2014**, *118*, 13801–13808.

(160) Barrow, S. J.; Wei, X.; Baldauf, J. S.; Funston, A. M.; Mulvaney, P. The Surface

Plasmon Modes of Self-Assembled Gold Nanocrystals. *Nat. Commun.* **2012**, *3*, 1275.

(161) Roller, E.-M.; Khorashad, L. K.; Fedoruk, M.; Schreiber, R.; Govorov, A. O.; Liedl, T. DNA-Assembled Nanoparticle Rings Exhibit Electric and Magnetic Resonances at Visible Frequencies. *Nano Lett.* **2015**, *15*, 1368–1373.

(162) Barrow, S. J.; Funston, A. M.; Wei, X.; Mulvaney, P. DNA-Directed Self-Assembly and Optical Properties of Discrete 1D, 2D and 3D Plasmonic Structures. *Nano Today* **2013**, *8*, 138–167.

(163) Gordon, M. J.; Peyrade, D. Separation of Colloidal Nanoparticles Using Capillary Immersion Forces. *Appl. Phys. Lett.* **2006**, *89*.

(164) Ni, S.; Leemann, J.; Buttinoni, I.; Isa, L.; Wolf, H. Programmable Colloidal Molecules from Sequential Capillarity-Assisted Particle Assembly. *Sci. Adv.* **2016**, *2*, e1501779–e1501779.

(165) Slaughter, L. S.; Wang, L.-Y.; Willingham, B. A.; Olson, J. M.; Swanglap, P.; Dominguez-Medina, S.; Link, S. Plasmonic Polymers Unraveled through Single Particle Spectroscopy. *Nanoscale* **2014**, *6*, 11451–11461.

(166) Yan, B.; Boriskina, S. V.; Reinhard, B. M. Optimizing Gold Nanoparticle Cluster Configurations ($N \leq 7$) for Array Applications. *J. Phys. Chem. C* **2011**, *115*, 4578–4583.

(167) Graham, R. L.; Lubachevsky, B. D.; Nurmela, K. J.; Östergård, P. R. J. Dense Packings of Congruent Circles in a Circle. *Discrete Math.* **1998**, *181*, 139–154.

(168) Portalès, H.; Pinna, N.; Pileni, M.-P. Optical Response of Ultrafine Spherical Silver Nanoparticles Arranged in Hexagonal Planar Arrays Studied by the DDA Method. *J. Phys. Chem. A* **2009**, *113*, 4094–4099.

(169) Yang, P.; Portalès, H.; Pileni, M.-P. Ability to Discern the Splitting between Longitudinal and Transverse Plasmon Resonances in Au Compared to Ag Nanoparticles in Close-Packed Planar Arrays. *Phys. Rev. B* **2010**, *81*, 205405.

(170) Bao, K.; Mirin, N. A.; Nordlander, P. Fano Resonances in Planar Silver Nanosphere Clusters. *Appl. Phys. A* **2010**, *100*, 333–339.

(171) Harris, N.; Arnold, M. D.; Blaber, M. G.; Ford, M. J. Plasmonic Resonances of Closely Coupled Gold Nanosphere Chains. *J. Phys. Chem. C* **2009**, *113*, 2784–2791.

(172) Barrow, S. J.; Funston, A. M.; Gómez, D. E.; Davis, T. J.; Mulvaney, P. Surface Plasmon Resonances in Strongly Coupled Gold Nanosphere Chains from Monomer to Hexamer. *Nano Lett.* **2011**, *11*, 4180–4187.

(173) Maier, S. A.; Kik, P. G.; Atwater, H. A. Observation of Coupled Plasmon-Polariton Modes in Au Nanoparticle Chain Waveguides of Different Lengths: Estimation of Waveguide Loss. *Appl. Phys. Lett.* **2002**, *81*, 1714–1716.

(174) Barrow, S. J.; Rossouw, D.; Funston, A. M.; Botton, G. A.; Mulvaney, P. Mapping Bright and Dark Modes in Gold Nanoparticle Chains Using Electron Energy Loss Spectroscopy. *Nano Lett.* **2014**, *14*, 3799–3808.

(175) Willingham, B.; Link, S. Energy Transport in Metal Nanoparticle Chains *via* Sub-Radiant Plasmon Modes. *Opt. Express* **2011**, *19*, 6450–6461.

(176) Slaughter, L. S.; Willingham, B. A.; Chang, W. S.; Chester, M. H.; Ogden, N.; Link, S. Toward Plasmonic Polymers. *Nano Lett.* **2012**, *12*, 3967–3972.

(177) Si, K. J.; Sikdar, D.; Chen, Y.; Eftekhari, F.; Xu, Z.; Tang, Y.; Xiong, W.; Guo, P.; Zhang, S.; Lu, Y.; *et al*. Giant Plasmene Nanosheets, Nanoribbons, and Origami. *ACS Nano* **2014**, *8*, 11086–11093.

(178) Hanske, C.; Tebbe, M.; Kuttner, C.; Bieber, V.; Tsukruk, V. V; Chanana, M.; König, T. A. F.; Fery, A. Strongly Coupled Plasmonic Modes on Macroscopic Areas *via* Template-Assisted Colloidal Self-Assembly. *Nano Lett.* **2014**, *14*, 6863–6871.

(179) Scheeler, S. P.; Mühlig, S.; Rockstuhl, C.; Hasan, S. Bin; Ullrich, S.; Neubrech, F.; Kudera, S.; Pacholski, C. Plasmon Coupling in Self-Assembled Gold Nanoparticle-Based Honeycomb Islands. *J. Phys. Chem. C* **2013**, *117*, 18634–18641.

(180) Lin, M. H.; Chen, H. Y.; Gwo, S. Layer-by-Layer Assembly of Three-Dimensional Colloidal Supercrystals with Tunable Plasmonic Properties. *J. Am. Chem. Soc.* **2010**, *132*, 11259–11263.

(181) Ung, T.; Liz-Marzán, L. M.; Mulvaney, P. Optical Properties of Thin Films of Au@SiO2 Particles. *J. Phys. Chem. B* **2001**, *105*, 3441–3452.

(182) Olson, J.; Dominguez-Medina, S.; Hoggard, A.; Wang, L.-Y.; Chang, W.-S.; Link, S. Optical Characterization of Single Plasmonic Nanoparticles. *Chem. Soc. Rev.* **2015**, *44*, 40–57.

(183) Steiner, E.; Fowler, P. W.; Jenneskens, L. W. Counter-Rotating Ring Currents in

Coronene and Corannulene. *Angew. Chemie - Int. Ed.* **2001**, *40*, 362–366.

(184) Rodríguez-Fernández, J.; Pérez-Juste, J.; García de Abajo, F. J.; Liz-Marzán, L. M. Seeded Growth of Submicron Au Colloids with Quadrupole Plasmon Resonance Modes. *Langmuir* **2006**, *22*, 7007–7010.

(185) Casas, J.; Venkataramasubramani, M.; Wang, Y.; Tang, L. Replacement of Cetyltrimethylammoniumbromide Bilayer on Gold Nanorod by Alkanethiol Crosslinker for Enhanced Plasmon Resonance Sensitivity. *Biosens. Bioelectron.* **2013**, *49*, 525–530.

(186) Vernon, K. C.; Funston, A. M.; Novo, C.; Gómez, D. E.; Mulvaney, P.; Davis, T. J. Influence of Particle-Substrate Interaction on Localized Plasmon Resonances. *Nano Lett.* **2010**, *10*, 2080–2086.

(187) Johnson, P. B.; Christy, R. W. Optical Constants of the Noble Metals. *Phys. Rev. B* **1972**, *6*, 4370–4379.

(188) Wang, H.; Brandl, D. W.; Nordlander, P.; Halas, N. J. Plasmonic Nanostructures: Artificial Molecules. *Acc. Chem. Res.* **2007**, *40*, 53–62.

(189) Meinzer, N.; Barnes, W. L.; Hooper, I. R. Plasmonic Meta-Atoms and Metasurfaces. *Nat. Photonics* **2014**, *8*, 889–898.

(190) Barrow, S. J.; Collins, S. M.; Rossouw, D.; Funston, A. M.; Botton, G. A.; Midgley, P. A.; Mulvaney, P. An Electron Energy Loss Spectroscopy Investigation Into Symmetry in Gold Trimer and Tetramer Plasmonic Nanoparticle Structures. *ACS Nano* **2016**, acsnano.6b03796.

(191) Cherqui, C.; Wu, Y.; Li, G.; Quillin, S. C.; Busche, J. A.; Thakkar, N.; West, C. A.; Montoni, N. P.; Rack, P. D.; Camden, J. P.; *et al.* STEM/EELS Imaging of Magnetic Hybridization in Symmetric and Symmetry-Broken Plasmon Oligomer Dimers and All-Magnetic Fano Interference. *Nano Lett.* **2016**, *16*, 6668–6676.

(192) Karaveli, S.; Zia, R. Strong Enhancement of Magnetic Dipole Emission in a Multilevel Electronic System. *Opt. Lett.* **2010**, *35*, 3318–3320.

(193) Noginova, N.; Zhu, G.; Mavy, M.; Noginov, M. A. Magnetic Dipole Based Systems for Probing Optical Magnetism. *J. Appl. Phys.* **2008**, *103*, 7–10.

(194) Karaveli, S.; Zia, R. Spectral Tuning by Selective Enhancement of Electric and Magnetic Dipole Emission. *Phys. Rev. Lett.* **2011**, *106*, 1–4.

(195) Sawai, K.; Tatumi, R.; Nakahodo, T.; Fujihara, H. Asymmetric Suzuki-Miyaura

Coupling Reactions Catalyzed by Chiral Palladium Nanoparticles at Room Temperature. *Angew. Chemie - Int. Ed.* **2008**, *47*, 6917–6919.

(196) Ma, W.; Kuang, H.; Xu, L.; Ding, L.; Xu, C.; Wang, L.; Kotov, N. A. Attomolar DNA Detection with Chiral Nanorod Assemblies. *Nat. Commun.* **2013**, *4*, 2689; 1-8.

(197) Wu, X.; Xu, L.; Ma, W.; Liu, L.; Kuang, H.; Kotov, N. A.; Xu, C. Propeller-Like Nanorod-Upconversion Nanoparticle Assemblies with Intense Chiroptical Activity and Luminescence Enhancement in Aqueous Phase. *Adv. Mater.* **2016**, 5907–5915.

(198) Zhao, Y.; Askarpour, A. N.; Sun, L.; Shi, J.; Li, X.; Alù, A. Chirality Detection of Enantiomers Using Twisted Optical Metamaterials. *Nat. Commun.* **2017**, *8*, 14180.

(199) Slaughter, L. S.; Wu, Y.; Willingham, B. a.; Nordlander, P.; Link, S. Effects of Symmetry Breaking and Conductive Contact on the Plasmon Coupling in Gold Nanorod Dimers. *ACS Nano* **2010**, *4*, 4657–4666.

(200) Tan, S. F.; Anand, U.; Mirsaidov, U. Interactions and Attachment Pathways between Functionalized Gold Nanorods. *ACS Nano* **2017**, acsnano.6b07398.

(201) Shao, L.; Woo, K. C.; Chen, H.; Jin, Z.; Wang, J.; Lin, H.-Q. Angle- and Energy-Resolved Plasmon Couplings in Gold Nanorod Dimers. *ACS Nano* **2010**, *3053*, 3062.

(202) Fontana, J.; Charipar, N.; Flom, S. R.; Naciri, J.; Piqué, A.; Ratna, B. R. Rise of the Charge Transfer Plasmon: Programmable Concatenation of Conductively Linked Gold Nanorod Dimers. *ACS Photonics* **2016**, *3*, 904–911.

(203) Funston, A. M.; Novo, C.; Davis, T. J.; Mulvaney, P. Plasmon Coupling of Gold Nanorods at Short Distances and in Different Geometries. *Nano Lett.* **2009**, *9*, 1651–1658.

(204) Kumar, J.; Wei, X.; Barrow, S.; Funston, A. M.; Thomas, K. G.; Mulvaney, P. Surface Plasmon Coupling in End-to-End Linked Gold Nanorod Dimers and Trimers. *Phys. Chem. Chem. Phys.* **2013**, *15*, 4258–4264.

(205) Lu, X.; Wu, J.; Zhu, Q.; Zhao, J.; Wang, Q.; Zhan, L.; Ni, W. Circular Dichroism from Single Plasmonic Nanostructures with Extrinsic Chirality. *Nanoscale* **2014**, *6*, 14244–14253.

(206) Ross, M. B.; Mirkin, C. A.; Schatz, G. C. Optical Properties of One-, Two-, and Three-Dimensional Arrays of Plasmonic Nanostructures. *J. Phys. Chem. C* **2016**, acs.jpcc.5b10800.

(207) Gómez-Graña, S.; Hubert, F.; Testard, F.; Guerrero-Martínez, A.; Grillo, I.; Liz-Marzán, L. M.; Spalla, O. Surfactant (Bi)Layers on Gold Nanorods. *Langmuir* **2012**, *28*, 1453–1459.

(208) Jishkariani, D.; Diroll, B. T.; Cargnello, M.; Klein, D. R.; Hough, L. A.; Murray, C. B.; Donnio, B. Dendron-Mediated Engineering of Interparticle Separation and Self-Assembly in Dendronized Gold Nanoparticles Superlattices. *J. Am. Chem. Soc.* **2015**, *137*, 10728–10734.

(209) Andres, R. P.; Bielefeld, J. D.; Henderson, J. I.; Janes, D. B.; Kolagunta, V. R.; Kubiak, C. P.; Mahoney, W. J.; Osifchin, R. G. Self-Assembly of a Two-Dimensional Superlattice of Molecularly Linked Metal Clusters. *Science (80-.).* **1996**, *273*, 1690–1693.

(210) Fafarman, A. T.; Hong, S.-H.; Caglayan, H.; Ye, X.; Diroll, B. T.; Paik, T.; Engheta, N.; Murray, C. B.; Kagan, C. R. Chemically Tailored Dielectric-to-Metal Transition for the Design of Metamaterials from Nanoimprinted Colloidal Nanocrystals. *Nano Lett.* **2013**, *13*, 350–357.

(211) Jung, H.; Cha, H.; Lee, D.; Yoon, S. Bridging the Nanogap with Light: Continuous Tuning of Plasmon Coupling between Gold Nanoparticles. *ACS Nano* **2015**, 151014231344007.

(212) Rupich, S. M.; Castro, F. C.; Irvine, W. T. M.; Talapin, D. V. Soft Epitaxy of Nanocrystal Superlattices. *Nat. Commun.* **2014**, *5*, 5045.

(213) Alù, A.; Engheta, N. Dynamical Theory of Artificial Optical Magnetism Produced by Rings of Plasmonic Nanoparticles. *Phys. Rev. B* **2008**, *78*, 85112.

(214) Stenger, N.; Rehspringer, J.-L.; Hirlimann, C. Template-Directed Self-Organized Silica Beads on Square and Penrose-like Patterns. *J. Lumin.* **2006**, *121*, 278–281.

(215) Namin, F. A.; Yuwen, Y. A.; Liu, L.; Panaretos, A. H.; Werner, D. H.; Mayer, T. S. Efficient Design, Accurate Fabrication and Effective Characterization of Plasmonic Quasicrystalline Arrays of Nano-Spherical Particles. *Sci. Rep.* **2016**, *6*, 22009.

(216) Talapin, D. V; Shevchenko, E. V; Bodnarchuk, M. I.; Ye, X.; Chen, J.; Murray, C. B. Quasicrystalline Order in Self-Assembled Binary Nanoparticle Superlattices. *Nature* **2009**, *461*, 964–967.

(217) Dai, Q.; Chen, Y.; Liu, C. C.; Rettner, C. T.; Holmdahl, B.; Gleixner, S.; Chung, R.; Pitera, J. W.; Cheng, J.; Nelson, A. Programmable Nanoparticle Ensembles via High-Throughput Directed Self-Assembly. *Langmuir* **2013**, *29*, 3567–3574.

(218) Shelby, R. A. Experimental Verification of a Negative Index of Refraction. *Science (80-.).* **2001**, *292*, 77–79.

(219) Liu, N.; Liu, H.; Zhu, S.; Giessen, H. Stereometamaterials. *Nat. Photonics* **2009**, *3*, 157–162.

(220) Cargnello, M.; Johnston-Peck, A. C.; Diroll, B. T.; Wong, E.; Datta, B.; Damodhar, D.; Doan-Nguyen, V. V. T.; Herzing, A. A.; Kagan, C. R.; Murray, C. B. Substitutional Doping in Nanocrystal Superlattices. *Nature* **2015**, *524*, 450–453.

(221) Zheludev, N. I.; Kivshar, Y. S. From Metamaterials to Metadevices. *Nat. Mater.* **2012**, *11*, 917–924.

(222) Appavoo, K.; Haglund, R. F. Detecting Nanoscale Size Dependence in VO2 Phase Transition Using a Split-Ring Resonator Metamaterial. *Nano Lett.* **2011**, *11*, 1025–1031.

(223) Paik, T.; Hong, S.-H.; Gaulding, E. A.; Caglayan, H.; Gordon, T. R.; Engheta, N.; Kagan, C. R.; Murray, C. B. Solution-Processed Phase-Change VO2 Metamaterials from Colloidal Vanadium Oxide (VOx) Nanocrystals. *ACS Nano* **2014**, *8*, 797–806.

(224) Lopez, R.; Feldman, L.; Haglund, R. Size-Dependent Optical Properties of VO2 Nanoparticle Arrays. *Phys. Rev. Lett.* **2004**, *93*, 177403.

(225) Ye, J.; Van Dorpe, P. Plasmonic Behaviors of Gold Dimers Perturbed by a Single Nanoparticle in the Gap. *Nanoscale* **2012**, *4*, 7205–7211.

(226) Gordon, T. R.; Paik, T.; Klein, D. R.; Naik, G. V; Caglayan, H.; Boltasseva, A.; Murray, C. B. Shape-Dependent Plasmonic Response and Directed Self-Assembly in a New Semiconductor Building Block, Indium-Doped Cadmium Oxide (ICO). *Nano Lett.* **2013**, *13*, 2857–2863.

(227) Brown, L. V.; Sobhani, H.; Lassiter, J. B.; Nordlander, P.; Halas, N. J. Heterodimers: Plasmonic Properties of Mismatched Nanoparticle Pairs. *ACS Nano* **2010**, *4*, 819–832.

(228) Bigelow, N. W.; Vaschillo, A.; Camden, J. P.; Masiello, D. J. Signatures of Fano Interferences in the Electron Energy Loss Spectroscopy and Cathodoluminescence of Symmetry-Broken Nanorod Dimers. *ACS Nano* **2013**, *7*, 4511–4519.

(229) Lombardi, A.; Grzelczak, M. P.; Pertreux, E.; Crut, A.; Maioli, P.; Pastoriza-Santos, I.; Liz-Marzán, L. M.; Vallée, F.; Del Fatti, N. Fano Interference in the Optical Absorption of an Individual Gold–Silver Nanodimer. *Nano Lett.* **2016**, *16*,

6311–6316.

(230) Sheikholeslami, S.; Jun, Y. W.; Jain, P. K.; Alivisatos, a. P. Coupling of Optical Resonances in a Compositionally Asymmetric Plasmonic Nanoparticle Dimer. *Nano Lett.* **2010**, *10*, 2655–2660.

(231) Liu, X.; Biswas, S.; Jarrett, J. W.; Poutrina, E.; Urbas, A.; Knappenberger, K. L.; Vaia, R. A.; Nealey, P. F. Deterministic Construction of Plasmonic Heterostructures in Well-Organized Arrays for Nanophotonic Materials. *Adv. Mater.* **2015**, *27*, 7314–7319.

(232) Virganavičius, D.; Juodėnas, M.; Tamulevičius, T.; Schift, H.; Tamulevičius, S. Investigation of Transient Dynamics of Capillary Assisted Particle Assembly Yield. *Appl. Surf. Sci.* **2017**.

(233) Tinguely, J.-C.; Charron, G.; Lau-Truong, S.; Hohenau, A.; Grand, J.; Félidj, N.; Aubard, J.; Krenn, J. R. Template-Assisted Deposition of CTAB-Functionalized Gold Nanoparticles with Nanoscale Resolution. *J. Colloid Interface Sci.* **2013**, *394*, 237–242.